

https://dspace.org/

# Toward the development of an economically viable digital x-ray imaging device

**Mlambo, Musikavanhu Roy**

**2010-08-03**
http://hdl.handle.net/10539/8350

Downloaded from a DSpace repository. https://dspace.org/

# TOWARD THE DEVELOPMENT OF AN ECONOMICALLY VIABLE DIGITAL X-RAY IMAGING DEVICE

Musikavanhu Roy Mlambo

A research report submitted to the Faculty of Science, University of the Witwatersrand, Johannesburg, in partial fulfilment of the requirements for the degree of Master of Sciences.

October 2009

**DECLARATION**

I, the undersigned, hereby declare that the work contained in this research report is my own original work. It is being submitted for the Degree of Masters of Science in the University of the Witwatersrand. I have not previously in its entirety or in part submitted it at any other university for a degree or examination.

Signature: ……

Date: ……

# ABSTRACT

A project aimed at the development of a robot-based patient positioning system for high-precision proton radiotherapy is underway at iThemba LABS. Part of the project included the development of a portal digital x-ray imaging device that would be used to verify the patient treatment set-up. The imaging device consisted of a scintillation screen, front surface mirror and a high-resolution charged-couple device (CCD) camera. The total costs for the device were about 7 times less expensive than a commercial amorphous silicon flat panel detector. To improve the efficiency of the system, the CCD chip and scintillation screen were chosen so that the wavelength of the light from the screen closely matched the wavelength at which the CCD sensor has the maximum quantum efficiency. The digital images compared favourably with those of x-ray film. Although the digital images were of lower resolution due to the finite resolution of the CCD chip, they were considered satisfactory. The use of pixel binning allowed for the use of lower exposure settings when compared to exposure settings for un-binned images. This resulted in a reduction of patient dose without significantly compromising image quality. The device would not be used for diagnostic purposes, but only to verify patient position at treatment setup. As such, the digital images would be compared against digitally reconstructed radiographs (DRRs) of the fields and/or the treatment position, which are created from the treatment planning Computed Tomography (CT) images. In general, the spatial resolution of the DRRs is also comparably lower than digital x-ray images, as the resolution of the DRRs is limited to the voxel size of the CT images.

In Memory of my Mother

Esnarth Mlambo

(1945 – 2002)

# ACKNOWLEDGEMENTS

I would like to thank my Maker and God for the countless opportunities He has given me, including the opportunity to do my Masters.

Thanks goes to my supervisor Mr. Evan de Kock, without whom the writing of this manuscript would have not been possible; I also want to thank him for allowing me to do the project with him at the iThemba LABS institute in Cape Town. I would also like to thank my co-supervisor Prof Debbie Van der Merwe, for the invaluable assistance she has given me on numerous occasions.

I am grateful to my family, in particular to my brother Dr. Kupukile Mlambo, for the belief in me; they stood by me and gave me the support that I needed. I would like to thank my wife Motlatso Mlambo who encouraged me to finish this report in spite of the challenges I was facing. My appreciation goes to Dr. Andrew Forbes of the CSIR for allowing me to use the Laser Technology facilities at the CSIR and Ms. Tshepiso Baisitse as well as Dr. Malik Maaza for assisting me with measurements and analysis of the data. I would like to thank Mr. Steven Maage and Dr. Mark Swanepoel for their invaluable assistance with the Monte Carlo simulations. I would also like to thank the staff at the iThemba LABS library, especially Ms. Audrey Sauls for providing me with the publications and material I requested. Thanks goes to Mr. Jan Van der Merwe for his assistance with the synchronization card, which made doing the experiments much easier. I would also like to thank Mr. Jamie Nieto-Camero for the useful discussions we had. Finally I would like to thank all the staff from the Medical Radiation Group at iThemba LABS who contributed and assisted in one way or the other.

# TABLE OF CONTENTS

ABSTRACT i
ACKNOWLEDGEMENTS iii
TABLE OF CONTENTS iv
LIST OF FIGURES vi
LIST OF TABLES viii
ABBREVIATIONS ix
CHAPTER 1 Introduction 1
1.1 Motivation for the Project 6
CHAPTER 2 Literature review 8
2.1 Lens Coupled Systems 8
2.2 Lens Distortions 10
2.3 Radiographic Imaging Systems 12
2.4 Veiling Glare 13
2.5 Patient Exposure and Dosimetry in Radiology 14
CHAPTER 3 Methodology 18
3.1 Calibration Frames (Dark, Flat and Bias Frame) 20
3.2 Working Distance and the Depth of Field 22
3.3 Characterisation of Apogee AP47p Camera 26
3.3.1 Exposure Variation 26
3.3.2 Linearity 28
3.3.3 Signal Variance, Gain 28
3.3.4 System Noise 29
3.4 Lens Coupling Efficiency 29
3.5 Resolution 30
3.6 Exposure Synchronisation Card 33
3.7 Correction for Lens Distortion 33
3.8 Optical Scatter 37
3.8.1 Zygo Experiment 38
3.8.2 Optical Scatter Experiments 39
3.9 X-ray Imaging and Pixel Binning 41
3.10 Shielding (MCNPX) 42
CHAPTER 4 Results and discussion 45
4.1 Calibration Frames (Dark, Flat and Bias Frame) 45
4.2 Working Distance and the Depth of Field (DOF) 49
4.3 Characterisation of Apogee AP47p Camera 53
4.3.1 Exposure Variation 53

4.3.2 Linearity 55
4.3.3 Signal Variance, Gain 55
4.3.4 System Noise 56
4.4 Lens Coupling Efficiency 57
4.5 Resolution 58
4.6 Correction for Lens Distortion 60
4.7 Zygo Experiment 64
4.8 Optical Scatter Experiments 66
4.8.1 Anti-Scatter Grid 71
4.9 X-ray Imaging and Pixel Binning 73
4.9.1 Pixel Binning 74
4.10 Shielding (MCNPX ) 77
CHAPTER 5 Conclusion 79
References 81
APPENDIX A. - 1 -
TEST DATA SHEET - 1 -
APPENDIX B. - 2 -
CAMERA TEST METHODS - 2 -
APPENDIX C. - 8 -
C.1 Quantum Efficiency - 8 -
C.2 Depth of Field - 11 -
C.3 Field of View - 14 -
C.4 Lens Coupling Efficiency - 14 -
C.5 Lens Distortion - 20 -
C.6 Projective Camera Model - 25 -
C.7 Distortion Model - 28 -

# LIST OF FIGURES

Figure 1.1-1 An illustration of how CT data is aquired and used to calculate the digitally reconstructed radiograph (DDR) ..... 4
Figure 2.5-1 The effect of vaious dosimetric quantities in the dose-to-information conversion factor, $SNR^2$/dose.. ..... 17
Figure 3.1-1 The spectral response of the CCD47-10 High Performance AIMO Back thinned CCD Sensor. ..... 18
Figure 3.2-1 A test rig for doing the optical test for the CCD Camera..... 24
Figure 3.2-2 Diagram showing the Bar chart test pattern ..... 25
Figure 3.3-1 A diagram showing the set-up of the light source and the camera. ..... 27
Figure 3.5-1 The digital x-ray imaging device with a phantom in place ..... 31
Figure 3.6-1 A block diagram for micro controller card ..... 33
Figure 3.7-1 A diagram illustrating bilinear interpolation..... 36
Figure 3.8-1 An illustration of the components of a light reflection model ..... 38
Figure 3.8-2 An illustration of the Maximum peak-to valley height..... 39
Figure 3.8-3 An illustration of the arithematic mean deviation..... 39
Figure 3.9-1 An illustration showing pixel binning..... 41
Figure 3.10-1 Illustration showing the relative positions of the various beam elements that were included in the Monte Carlo simulations ..... 44
Figure 3.10-2 An illustration of the geometry of the x-ray imaging device. ..... 44
Figure 4.1-1 The variation of bias current with temperature ..... 45
Figure 4.1-2 (a) A typical flat frame. (Temperature is at $-20^oC$) (b) An illustration of a line profile of flat frame ..... 46
Figure 4.1-3 A typical bias frame. (Temperature is at $-20^oC$)..... 46
Figure 4.1-4 A typical dark frame. (Temperature is at $-20^oC$)..... 47
Figure 4.1-5 The variation of dark current with temperature. ..... 48
Figure 4.1-6 The variation of dark current with temperature. ..... 48
Figure 4.1-7 The variation of dark current with temperature. ..... 49
Figure 4.2-1 The variation of FWHM with distance using a 2 cm white disc..... 50
Figure 4.2-2 The variation of maximum pixel value with distance. ..... 51
Figure 4.2-3 Illustartion of DOF for the various f-stops..... 52
Figure 4.3-1 An illustration of the flat frame, Flat1, with photons per ADU setting of 10..... 53
Figure 4.3-2 An illustration of the Flat frame, Flat3, with photons per ADU setting of 10..... 54
Figure 4.3-3 A plot of flat frame histograms ..... 54
Figure 4.3-4 A plot of the system linearity. ..... 55
Figure 4.3-5 A plot of the signal variance ..... 56
Figure 4.5-1 A plot of the measured edge spread function for the digital x-ray image. ..... 58
Figure 4.5-2 A plot of the line spread function obtained from the ESF for the digital x-ray image. ..... 59
Figure 4.5-3 The modulation transfer function of the digital imaging system. ..... 59
Figure 4.6-1 A graphical representation of the distortion model incorporating the tangential and radial distortion..... 61
Figure 4.6-2 An illustration showing the correction for lens distortion. ..... 62
Figure 4.6-3 An illustration showing the correction for lens distortion, for a skull x-ray image. ..... 63

Figure 4.6-4 The histogram for the subtraction of the distorted and un-distorted images shown in Figure 4.6-3. ..... 64
Figure 4.7-1 The surface analysis using the MetroPro Zygo interferometer.. ..... 65
Figure 4.8-1 The effect of paper strip width on measured optical scatter. The profiles were taken in the AB direction. ..... 67
Figure 4.8-2 The effect of paper strip width on measured optical scatter. The profiles were taken in the GT direction. ..... 67
Figure 4.8-3 The effect of plastic strip width on measured optical scatter. The profiles were taken in the GT direction. ..... 68
Figure 4.8-4 The effect of plastic strip width on measured optical scatter. The profiles were taken in the AB direction. ..... 68
Figure 4.8-5 The effect of measurement strip width on measured optical scatter. The measurements were taken with a 600 mm × 450 mm 6 MV beam using the high-speed imager. ..... 69
Figure 4.8-6 The maximum scatter as a function of mask area. ..... 70
Figure 4.8-7 The measured optical scatter on the central axis in the GT direction of imager for a range of mask sizes. ..... 70
Figure 4.8-8 The effect of adding an anti-scatter grid. ..... 71
Figure 4.8-9 (a) An image of skull with the 'privacy filter' (b) An image of skull without the 'privacy filter' (c) Difference image ..... 72
Figure 4.8-10 A histogram of the subtraction image of the skull (taken with the use of the 'privacy filter' from image of skull without the 'privacy filter' ..... 72
Figure 4.9-1 An illustration of digital x-ray images compared to a film x-ray image. 73
Figure 4.9-2 An illustration of the digitally reconstructed radiograph of the skull from 5 mm slice thickness. ..... 74
Figure 4.9-3 An illustration showing the effects of pixel binning. ..... 75
Figure 4.9-4 An illustration showing the effect of Perspex slab in front skull; ..... 77

# LIST OF TABLES

Table 1.1-1 Rarex G-130 scintillation screen properties [From Lätti, 2000] ..... 5
Table 3.10-1 Properties of materials used for the beam components. ..... 43
Table 4.2-1 Calculated values for hypofocal distance, near focus and far focus at different apertures. ..... 52
Table 4.3-1 Comparison of results from Camera Test Data Sheet with those from measurements. ..... 57
Table 4.7-1 Values of PV( $\overline{\sigma_{PV}}$ ), RMS( $\overline{\sigma_{rms}}$ ) and $R_a$ ( $\overline{\sigma_{Ra}}$ )for the samples in μm. ..... 66
Table 4.9-1 Exposure settings for different binning schemes and film. ..... 76

# ABBREVIATIONS

| | |
|---|---|
| ADU | - Analog To Digital Unit |
| BMP | - Bitmap |
| CCD | - Charged-Couple Device |
| CT | - Computed Tomography |
| DRR | - Digitally Reconstructed Radiograph |
| ESF | - Edge Spread Function |
| FITS | - Flexible Image Transport System |
| FSHS | - Full-Scale Histogram Stretch |
| FWHM | - Full-Width at Half Maximum |
| ICRP | - International Commission on Radiological Protection |
| IAEA | - International Atomic Energy Agency |
| JPEG | - Joint Photographic Experts Group |
| LABS | - Laboratory for Accelerator Based Sciences |
| LED | - Light Emitting Diodes |
| MCNPX | - Monte Carlo N-Particle eXtended code |
| MOS | - Metal Oxide Semiconductor |
| MTF | -Modulation Transfer Function |
| PSF | - Point Spread Function |
| QA | - Quality Assurance |
| ROI | - Region Of Interest |
| SPG | - Stereophotogrammetry |
| SNR | - Signal-To-Noise Ratio |

# CHAPTER 1 INTRODUCTION

A project that was initially funded by a Technical Co-operation Programme of the International Atomic Energy Agency (IAEA), is underway at iThemba LABS (Laboratory for Accelerator Based Sciences). iThemba LABS is the only facility in the world that offers both proton and neutron therapy, and is the only particle therapy facility in Africa. This project was aimed at the development of a patient positioning system for high-precision proton radiotherapy. The project included the development of a portal radiographic system to verify the patient position in a setup for proton therapy. This report describes the work done in developing the device to allow the acquisition of digital x-ray images of the patient.

Proton therapy is considered a very effective treatment modality in the treatment of cancer lesions close to critical anatomical structures. Its success is due to the characteristic Bragg peak in the depth-dose curve of the proton beam. The Bragg peak is followed by a steep dose fall off to zero dose and as a result, the tumors can be accurately treated whilst completely sparing normal tissue behind the distal edge of the beam. It is essential that the patient be correctly and precisely positioned with respect to the proton beam, to ensure the accurate delivery of the dose to the treatment volume. Any misalignment of the beam and the volume being treated might be detrimental to the patients. Missing the treatment target volume, even partially, reduces the tumor control probability and increases the normal tissue complication probability (Herman *et al.*, 2000). Several studies have been conducted to validate and determine the importance of eliminating treatment set-up errors (Goitein, 1985; Lomax *et al.*, 2001).

Currently at iThemba LABS, a stereophotogrammetry (SPG) system is used to assist in positioning the patient undergoing proton therapy. Stereophotogrammetry techniques have their origins in procedures for land surveying to compute a three-dimensional view (a 3-D model) of the objects of interest, based on a pair of stereo images. Stereo images are two graphical representations of the same area taken from different view angles; however, the views must be at some relatively large angle to each other. The clinical SPG system cross-references reflective makers on the patient mask and compares the current position of the markers with the position of the markers from the treatment plan as computed by the treatment planning system. The position of the patient is then adjusted accordingly using a computer that controls the motorized treatment chair in which the patient sits. The position of the patient relative to the beam line also has to be checked before treatment can commence. To verify that the patient is positioned correctly, portal x-ray films are taken, which are then compared to a reference image. The reference image can be a simulation film or digitally reconstructed radiograph (DRR); the latter is constructed from a series of Computed Tomography (CT) images of the patient (Herman *et al.*, 2001; Boyer *et al.*, 1992). A simulation film is a radiographic film taken of the patient during the simulation of the treatment. A digitally reconstructed radiograph, DRR, is a two-dimensional x-ray image of detected primary photon intensity, which can be formed from the 3D volumetric CT data by ray-tracing from the source to an (imaginary) detector plane. Resolution is limited by the finite slice width of the CT scans, which is generally much larger than the in-slice spatial resolution.

Figure 1.1-1 shows how the DRR is calculated from the transit dose. Transit dose is a measure of the primary radiation transmitted through the patient and measured at a

point on the central ray at some point beyond the patient.The point $x_d$, $y_d$ is a general point in the DRR at which the detected signal is D($x_d$, $y_d$, $A$), within a field size of $A$. The transit dose is computed at a general point $r$, in the irradiated part of the patient. $R(r, x_d, y_d)$ is the radiological thickness from $r$ to $(x_d, y_d)$, which is equivalent to the distance travelled by the x-ray beam from entry to exit of the patient. The point $e$ is where the beam from the source $S$ exits the patient . A truly 3D treatment planning system can generate a digital radiograph (also known as the portal image) by ray tracing from the x-ray source S through the CT data. This ray tracing takes account of the ray divergence and differential photon attenuation. The DRR is given by

$$DRR(x_d, y_d) = In(I_0 / I_{x_d, y_d}) = \mu_w R \ , \qquad 1.1$$

where $I_0$ is the photon intensity from the source, and $\mu_w$ is the linear attenuation coefficient of water (computed for the effective diagnostic energy of the CT scanner, between 50 keV and 120 keV), and $I_{x_d, y_d}$ is the detected primary-photon intensity given by

$$I_{x_d, y_d} = I_0 \exp\left( -\sum_i \rho_{el,i} \sigma \Delta \right) . \qquad 1.2$$

$\sigma$ is the photon attenuation cross section, $\Delta$ is the CT voxel size $\rho_{el,i}$ is the electron density in the $i$th voxel and the sum is over all the voxels which lie on the ray from the source to the element $x_d$, $y_d$ of the detector. By definition the radiological thickness $R$ is

$$R = \sum \rho_{el,i}^{rel} \Delta \ , \qquad 1.3$$

Where $\rho_{el,i}^{rel}$ is the electron density of the $i$th voxel relative to that of water.

The computation of a DRR (Webb, 1993 and Webb, 1997) from a series of CT slices in the chest region of the patient is shown in Figure 1.1-1.

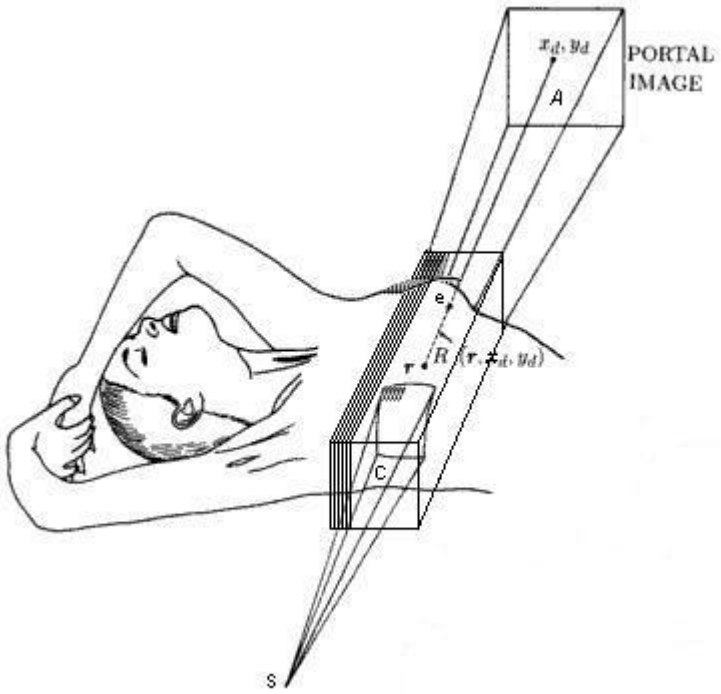



**Figure 1.1-1 An illustration of how CT data is aquired and used to calculate the digitally reconstructed radiograph (DDR)** *[Modified image from Webb, 1997]*

At iThemba LABS the verification x-ray images are currently obtained from a diagnostic x-ray tube, which when it is being used, is aligned with the proton beam axis. The patient is positioned between the x-ray tube and the x-ray film, which is also in the beam path, with the x-ray tube upstream with respect to the patient. However in the long run, portal x-ray films are expensive, and their processing and interpretation is labour intensive and time consuming. In addition, x-ray films are manually compared against DRRs and simulation films, a process that can be highly subjective, unreliable and inefficient. Potentially a more efficient and cost effective x-ray

imaging system can be implemented if a digital device for acquiring the x-ray images replaces the x-ray films.

The imaging device that has been developed consists of a scintillation screen, front surface mirror and a high-resolution charged-couple device (CCD) camera, which captures the radiographic images formed on the scintillation screen. Previous work was done on the selection of the scintillation screen and camera to be used in the construction of the imaging device (Renema, 1999; Ryneveld, 1995). The Rarex G-130 ($Gd_2O_2S$:Tb) scintillation screen together with the Apogee AP47p camera was chosen. The scintillation screen gave a relatively high light output compared to other screens that were tested previously, and the wavelength of the emitted light closely matched the wavelength for which the CCD of the Apogee AP47p camera has the maximum quantum efficiency. Some of the properties of the Rarex G-130 are shown in Table 1.1-1 below.

**Table 1.1-1 Rarex G-130 scintillation screen properties** *[From Lätti, 2000]*

| **Composition** | **Emission efficiency** | **Deposition density ($mg/cm^2$)** | **Phosphor thickness (mm)** | **Visual screen resolution (lp/mm)** | **Wavelength peak (nm)** |
|---|---|---|---|---|---|
| $Gd_2O_2S$:Tb | 16 % | 129.2 | 0.53 | 5.0 | 545 |

The images were then viewed on the display of the computer to which the CCD camera was connected. Essentially, there were two main aspects to the development of the imaging device. The first was to carry out a series of tests to characterize the

optical part of the imaging system. These optical tests were carried out to establish appropriate design parameters, which would give a suitable compromise between the compactness and the best optical characteristics of the x-ray imaging device. The second aspect in the development of the device was to determine the performance of the device. Investigations were also done to see how to improve the imaging device. These included the use of an anti-scatter grid and corrections for distortion caused by the optical system.

## *1.1 Motivation for the Project*

One of the main reasons for not purchasing a commercially available amorphous silicon flat panel detector for the patient position verification system was financial constraints. Large amorphous silicon detectors were significantly more expensive than the proposed camera-based system. A rough estimate showed that for the proposed camera system, the cost for the camera with lens, front surface mirror, scintillation screen and other fabrication costs, would be about R70 000. An amorphous silicon flat panel detector meeting the proposed system requirements would be in the region of about R500 000, which was almost 7 times more expensive than the digital camera system.

Another disadvantage with the use of amorphous silicon detectors was that, there was little data available to show how susceptible these detectors were to radiation damage when used in a proton therapy environment. In the event of the CCD camera being damaged by exposure to radiation, it would be considerably cheaper to replace the CCD sensor, compared to replacing the entire amorphous silicon detector.

The use of a digital imaging system allows x-ray images to be obtained in a very short time, unlike x-ray film, which requires a substantial amount of time to develop, store and maintain. With the camera system, the images were obtained in digital form, thus enabling computerized comparisons with DRRs. Digital radiography in general has the potential of improving image quality, reducing patient dose, improving data storage and retrieval, and reducing cost by eliminating the use of film (Giger and Doi, 1984). Unlike film, digital images allow for the implementation and application of image processing tools, such as contrast enhancement and image fusion. Film has the disadvantage that it has a fixed slope of the "characteristic curve", which limits contrast optimisation (Althof *et al.*, 1996).

There are however two drawbacks for a digital system. The digital images from camera-based imaging systems are generally of lower resolution and are subject to distortions due to the optical lens system. In the development of this imaging device the resolution was quantified, and corrections were made for the distortions.

The main work in the development of the imaging device involved:

(i) Optimising the design that gave the best compromise between the optical characteristics and the compactness of the device.

(ii) Developing software and techniques to correct for or minimize the effects of lens distortion, as well as the biasing, dark current and sensitivity variations in the CCD.

(iii) Determining the x-ray imaging characteristics of the device and the lowest exposure to the patient whilst maintaining adequate image quality.

(iv) Determining the shielding requirements for the camera.

(v) Studying the effects of veiling glare.

# CHAPTER 2 LITERATURE REVIEW

## *2.1 Lens Coupled Systems*

The imaging device developed was a lens-coupled system, which used a CCD chip as the detector. The device also utilised a scintillation screen, which provided the light image that was focused by the lens onto the CCD. Karellas *et al.* (1992) investigated the physical characteristics of a CCD image detector and its use in digital imaging. They suggested the use of a faster lens, or fibre optic coupling, as a means of improving the lens coupling efficiency. The speed of a lens refers to the maximum aperture diameter, or minimum f-number of a photographic lens, where the f-number is inversely proportional to the diameter of the lens. A lens with a larger maximum aperture diameter is a fast lens because it allows more light to the focal plane, allowing a faster shutter speed. A lens may be referred to as "fast" or "slow" depending on its maximum aperture compared to other lenses of similar focal length designed for a similar film format. Yu and Boone (1997) provided a derivation for the calculation of lens coupling efficiency. The optical coupling efficiency of the lens can be defined as the ratio of the optical energy incident upon the detector to the optical energy from the scintillator. Historically, calculations of lens coupling efficiency made assumptions as to whether the emission properties of the scintillator were Lambertian (i.e. light is equally emitted over all angles) or point radiators. Lambertian emitters obey Lambert's cosine law, which states that the radiant intensity emitted in any direction from a unit radiating surface falls off as the cosine of the angle between the normal to the surface and the direction of the radiation. The radiant intensity of such a surface is maximum normal to the surface and decreases in proportion to the cosine of the angle from the normal. This is described by

$$N = N_o \cos\theta \,, \qquad 2.1$$

where N is the radiant intensity, $N_o$ is the radiance normal to an emitting surface and $\theta$ is the angle between the viewing direction and the normal to the surface. It is generally accepted that every point on the surface of a scintillating screen emits light as if it were a uniform point source. Such a surface is regarded as an extended diffusing surface, which obeys Lambert's law (Liu *et al.,* 1994).

However, there are different classes of scintillators that are available. Yu and Boone (1997) suggested a more broadly applicable equation, which is useful for computing lens-coupling efficiency under more general conditions, without making assumptions about the emission characteristics of the scintillator. Liu *et al.* (1994) examined common lens coupling efficiency equations, and emphasised their proper use and associated parameters in the estimation of the signal-to-noise ratio (SNR). SNR in general is a measure of signal strength (which has the desired information) relative to background noise (Harwood, 2007). In image processing, the SNR of an image is usually defined as the ratio of the mean pixel value to the standard deviation of the pixel values (Rangayyan, 2005).

Giakoumakis and Miliotis (1985) investigated the angular distribution of the light emission from scintillation screens, and how this affected the calculation of the modulation transfer function (MTF) of a system using such a screen. In general the MTF is a two-dimensional function expressed in terms of either a two-dimensional frequency vector $k$ as MTF($k$), or orthogonal frequencies $u$ and $v$ as MTF($u$,$v$) (Beutel et al., 2000). The modulation transfer function can be defined as the ratio of the spatial frequencies of the image over the spatial frequencies of the input object being

imaged. The MTF describes the ability of the system to record the spatial frequencies (Oakley, 2003). Giakoumakis and Miliotis' observations showed that the light emitted by phosphor screens deviated considerably from the Lambertian distribution. Errors arising from ignoring the real angular distribution could introduce uncertainties of ±5 % to ±25 % in calculations of the light flux emitted and the absolute efficiency. They provided an equation, which was fitted to experimental data that gave a better estimate of the angular distribution of the light emitted from the scintillating screen.

Partridge *et al*. (1999) have investigated the optical scattering within camera-based electronic portal imaging devices. Their results suggested that the main source of optical scattering is multiple reflections between the scintillation screen and the 45° mirror. They found that for large radiation fields the scatter could be 20 % of the primary scintillator light intensity. To remove the optical scattering they proposed using a louvre grid (privacy screen) placed on the surface of the scintillation screen. This method has an advantage over deconvolution methods in that no calculations are required and all the scattering reduction is achieved optically. The use of the antiscatter grid was shown to effectively remove the optical scattering but introduced a uniform attenuation of about 25 %. The inclusion of the grid did not contribute to structured noise, and seemed to have very little effect on spatial resolution.

## *2.2 Lens Distortions*

It is well known that the use of a lens introduces some distortion in imaging. Liu *et al.* (2000) highlighted the significance of the presence of geometrical distortions in position-dependent procedures, where errors introduced by both radial and tangential

distortion, reduced the spatial accuracy of lens-coupled CCD systems. They suggested a method to correct for radial distortion, which used a polynomial transformation technique. The radial position of each pixel and the tangential offset component were corrected by applying two sets of N-order polynomials:

$$\theta' = a_1\theta + a_2\theta^2 + a_3\theta^3 + a_4\theta^4 + \cdots, \qquad 2.2$$

$$\rho' = b_1\rho + b_2\rho^2 + b_3\rho^3 + b_4\rho^4 + \cdots, \qquad 2.3$$

where, $a_i$ and $b_i$ are the distortion coefficients, and a feature point on the distorted image was specified by the polar coordinate $(\rho,\theta)$ and the point on the distortion-free image was denoted as $(\rho',\theta')$.

X-ray images of a grid wire placed in front of the scintillation screen were taken, and using digital image processing techniques, the image was then corrected for distortion. They found that a fourth order polynomial gave better results, although in theory a higher order polynomial gives less residual error. However, such higher order polynomials can cause unstable solutions. This approach could be adopted as part of the quality assurance of the imaging device. The method for correcting for lens distortion, which was used in this work, required the camera to be removed from the rest of the imaging device. This method was initially used before the construction of the box housing the camera, and no subsequent camera calibration were done; it was noted that a less cumbersome method could have been used. With the use of a calibration wire grid, as used by Liu *et al.* (2000), there would be no need for the camera to be removed from the rest of the device to obtain the lens distortion coefficients.

## 2.3 Radiographic Imaging Systems

Fujita *et al.* (1989) presented techniques to evaluate a commercial radiographic imaging system. They investigated the system response determined by the characteristic curves, the spatial resolution given by the modulation transfer function (MTF) and the noise analysis from the Wiener spectra. The Wiener spectrum represents the level of noise as a function of the spatial frequency and is similar to the MTF. Just as the ability of an imaging system to record an image contrast decreases as the object's spatial dimension becomes smaller and smaller, the ability of the system to record noise fluctuations decreases as the fluctuations become smaller and smaller in their spatial extent. The Wiener spectrum describes the noise amplitude as a function of spatial frequency and equals the Fourier Transform (FT) of the autocorrelation function in a uniformly exposed radiographic image. The autocorrelation function provides a measure of the correlation between noise fluctuations that occur at two different points in an image. In general, it is a function of the spatial distance between the points A$x$ and A$y$, (both in $x$ direction and $y$ direction) and is thus two-dimensional in nature. The autocorrelation for a separation A$x$ in the $x$ direction is calculated by multiplying the reconstructed value at a point $x,y$, r($x,y$), by the value r($x$ + A$x$,$y$) at $x$ + A$x$,$y$, to form the product r($x$,$y$) × r($x$ + A$x$,$y$). The autocorrelation function is then determined by averaging the product over all values of $x$ and $y$ throughout the image. The autocorrelation function of the noise is related to the Wiener spectrum also known as the noise power spectrum (Hanson, 1998 and Oakley, 2003). One way of estimating the autocorrelation for a given noise image is to first estimate the noise power spectrum and then calculate its inverse FT. Since the autocorrelation function may be calculated from the noise power spectrum, and vice versa, both of these methods provide equivalent and complete descriptions of

the correlations present in the noise (Hanson, 1981 and Wagner, 1976). Fujita *et al.* (1989) found that for exposures less than about $2.58 \times 10^{-8}$ C/kg, quantum mottle was dominant. Quantum mottle is mottle that is caused by the statistical fluctuation of the number of photons absorbed by the scintillating screens to form the light image. At high exposures, system intrinsic noise such as structure mottle of the imaging plate and electronic noise was dominant. Giger and Doi (1984) investigated the effect of various digital parameters on the MTF of a digital imaging radiographic system.

## *2.4 Veiling Glare*

Seibert *et al.* (1984) investigated the theoretical derivation of a point spread function that describes the veiling glare in x-ray image intensifiers, i.e. the scatter of electrons and light photons within an x-ray image intensifier. The scatter resulted in a degradation of the low-frequency response of the acquired image. Electrons and light produced from brighter areas, corresponding to regions of high transmission of the detected x-ray projection, migrated to the adjacent darker regions of low transmission. The theoretical methods for deriving the analytic point spread function (PSF) were confirmed with experiments. The experimental measurements were performed using various sized lead disks centrally located on the image receptor, giving a calculated contrast ratio as a function of disk radius. A simplification of the analytical form of the PSF gave an easy method relating contrast ratios to the parameterisation of the proposed PSF for an image intensifier. Seibert *et al*. (1985) also investigated the removal of the effects of veiling glare from images using mathematical deconvolution techniques. Fujita *et al.* (1985) noted that they had to collimate the x-ray beam to a small area to avoid the contribution of veil glare for their measurements using slits.

## 2.5 Patient Exposure and Dosimetry in Radiology

Motz and Danos (1978) examined the quantitative relationship between the image information content and the patient exposure. The information content was expressed in terms of spatial resolution and the number of greyscale levels required for detection of the structure of interest to the radiologist. They suggested that with the use of image processing and contrast enhancement tools, it should be possible to determine the patient exposure from the image information content desired by the radiologist, rather than the imaging requirements as in the case of film. X-ray film contains a considerable amount of image information, which cannot be detected by the human eye because of variations in film density that are below the visibility threshold. With image processing tools, it is possible to retrieve all this information even in low contrast images, which would normally be below the visibility threshold. Motz and Danos' (1978) results showed that for all subject thicknesses greater than 5 cm, a single exposure kilovoltage (between 40 kV and 70 kV) with adequate filtration, together with image enhancement and anti-scatter techniques could be used. They also recommended the use of antiscatter techniques in radiographic procedures to increase the image information content without necessarily increasing exposure.

Tapiovaara *et al.* (1999) investigated the effects of x-ray tube potential, beam filtration and antiscatter grids on patient dose and image quality in paediatric fluoroscopy. They highlighted the importance of optimizing the imaging techniques for digital radiographic systems so that their advantage over conventional systems could be fully utilized, a view that was also supported by Carlsson and Chan (1999). Tapiovaara *et al.* suggested an optimal technique that minimizes the absorbed dose in the patient with a constraint on constant image quality, where image quality was

expressed in terms of the signal to noise ratio, and not equal to input phosphor brightness. Contrary to the use of the automatic brightness control system of conventional x-ray machines, which are designed to increase the tube potential with patient thickness, their results suggest the most dose efficient tube voltage is almost independent of patient thickness, with an x-ray tube potential of 50 kV and 0.25 mm copper added filter resulting in dose savings of about 50 %. Their technique makes use of heavy filtration, thus requiring high tube loading, with tube loading increasing by a factor as much as 7 times compared to reference conditions of 70 kV and the basic 2.7 mm aluminium added filtration. They also showed that the interpretation of dose efficiency was dependent on the dosimetric quantity that was used, namely effective dose, mean phantom dose and air kerma. Dose efficiency can be taken to refer to the overall efficiency and is a product of geometric efficiency, quantum (also called capture efficiency) and charge conversion efficiency (Bronzino, 2000). The overall efficiency of the system should be high to minimize the patient radiation dose.

Geometric efficiency refers to the area of the detector sensitive to radiation as a fraction of the total exposed area. Quantum efficiency refers to the fraction of incident x-rays on the detector that are absorbed and contribute to the measured signal. Quantum efficiency is discussed in Appendix C. Conversion efficiency refers to the ability to accurately convert the absorbed x-ray signal into an electrical signal. To convert the photo-generated charges that are collected in the CCD pixels into a measurable quantity (e.g. a voltage signal), the CCD sensors employ an output node and a read-out circuitry to perform this function. The charges that are generated from incident photons are collected in the pixels and transferred across the CCD register before they can be converted into a voltage, which can be amplified before

transmission. The performance of this conversion stage is evaluated in terms of the charge conversion efficiency, which is expressed as the voltage per unit charge (Li and Nathan, 2005).

The effective dose is the sum of the weighted equivalent doses for all irradiated tissues or organs. Its is given by the expression

$$E = \sum_{\mathrm{T}} w_T \cdot H_T \,, \tag{2.4}$$

where $H_T$ is the equivalent dose in tissue or organ, T, and $w_T$ is the tissue weighting factor representing the proportionate detriment (stochastic) of tissue, T, when the body is irradiated uniformly. The tissue weighting factor takes into account the relative detriment of each organ and tissue including the different mortality and morbidity risks from cancer, the risk of severe hereditary effects for all generations, and the length of life lost due to these effects (NCRP, 1993 and ICRP, 1996).

The mean phantom dose, is the mean absorbed dose in the phantom and is given by

$$\begin{aligned} D_T &= 1 \Big/ m_T \int_{m_T} D \, dm \\ &= 1 \Big/ m_T \int_{m_T} \frac{d\bar{\varepsilon}}{dm} dm \end{aligned} \,, \tag{2.5}$$

where $m_T$ is the mass of the phantom and $D = \dfrac{d\bar{\varepsilon}}{dm}$ is the absorbed dose in the mass element, $dm$ (ICRP 1996).

Air kerma is kerma in a given mass of air. It is the kinetic energy released per unit mass of a volume of air when it is irradiated by an x-ray beam. It is a measure of the amount of radiation energy actually deposited in or absorbed in a unit mass of air.

Kerma, K, is defined as the quotient of d$E_{tr}$ by d$m$, where d$E_{tr}$ is the sum of the initial kinetic energies of all the charged ionizing particles liberated by uncharged ionizing particles in a volume element of mass d$m$, thus:

$$K = \frac{dE_{tr}}{dm}. \qquad 2.6$$

The unit of kerma is joule per kilogram (J/kg) which is also the gray (Gy).

In determining the most dose efficient imaging technique, Tapiovaara *et al.* (1999) showed how the dose-to-information conversion factor ($SNR^2$ /dose) versus tube potential curves varied when the dosimetric quantity was changed, as indicated in Figure 2.5-1.

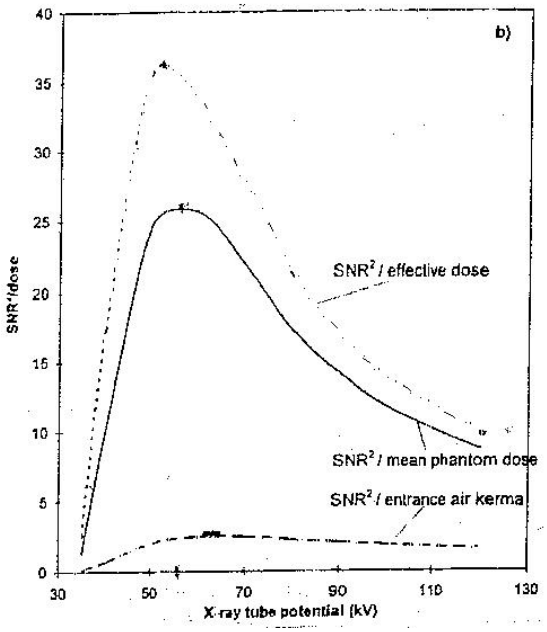



**Figure 2.5-1 The effect of various dosimetric quantities in the dose-to-information conversion factor, $SNR^2$/dose.** *$SNR^2$/mean dose in the phantom [$\mu Gy^{-1}$]; $SNR^2$/effective dose ($\mu Sv^{-1}$]; $SNR^2$/entrance air kerma (without backscatter) [$\mu Gy^{-1}$]. [Image from Tapiovaara, 1999].*

The imaging performance was evaluated in terms of $SNR^2$/dose, where the maximum in a given imaging task identifies the most dose-efficient imaging technique for that task.

# CHAPTER 3 METHODOLOGY

All measurements were done using the Apogee Camera, model AP47P, camera serial number A2804 and CCD serial number 01063-09-19. The CCD chip on the Apogee AP47p camera is a midband CCD from E2V Technologies. The CCD chip has an array size of 1024 × 1024 pixels and has a quantum efficiency of almost 92 % at the peak emission wavelength of the Rarex G-130 scintillation screen (about 545 nm) as shown in Figure 3.1-1.

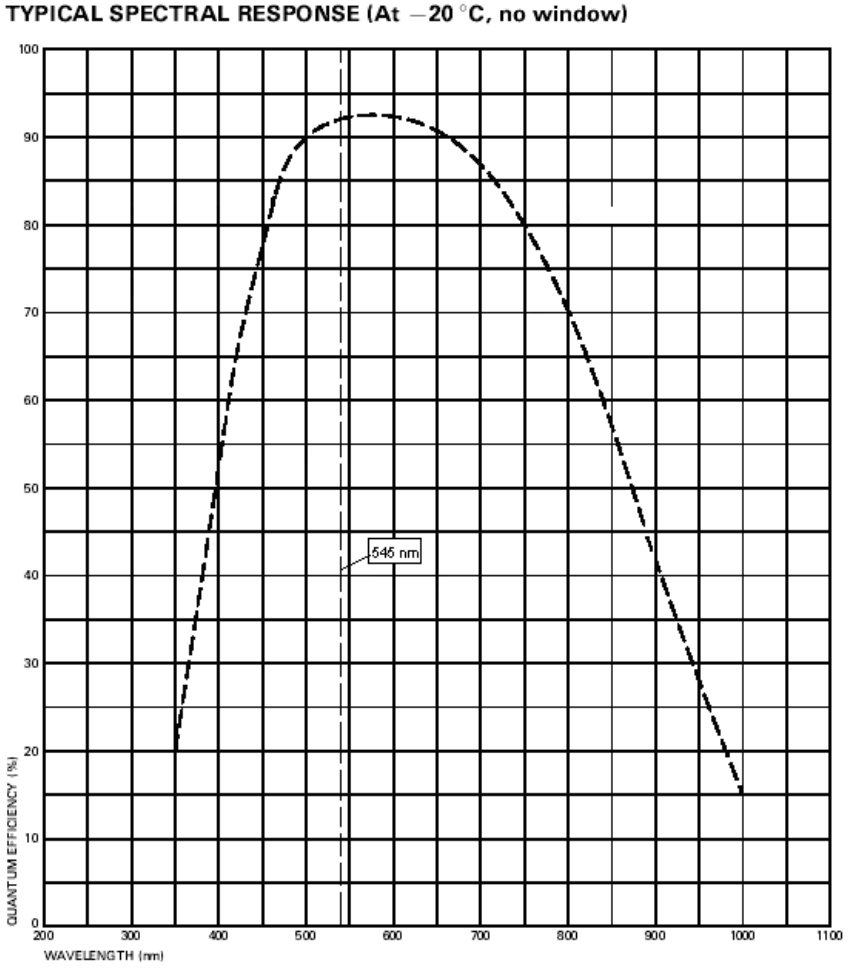



**Figure 3.1-1 The spectral response of the CCD47-10 High Performance AIMO Back thinned CCD Sensor**. *[Image from E2V Technologies, 2002]*

A Nikon Nikkor, 35 mm, f/14, lightweight, ultra-high speed, wide-angle lens was used. The lens had 9 elements in 7 groups, and had an actual focal length of 36 mm. Spherical, astigmatism and coma aberrations are well corrected for in this lens, by the manufacturer, to ensure uniformly sharp images of high contrast over the entire image plane even at full aperture. It has a minimum focus distance of 0.3 m, a nine-blade diaphragm with a minimum f-stop of 16 and a picture angle of 62°. The application of multilayer antireflective coating on the air-to-glass lens surface minimizes flare and ghost, suggesting improved contrast and natural colour rendition (Nikon Corporation). Lens flare and ghost are image artefacts which, when taking images near a strong light source might not necessarily be in the image. Flare is non-image-forming light in a camera due to the reflection of light from any surface such as that of the lens, lens mount or the interior of a camera. Flare is not an aberration, and manifests in a number of ways including coloured patches, ghost images, haloes, or a haze over the entire image. Flare can be caused by reflections at air/glass interfaces, at the lens barrel, at the diaphragm blades, at the film, or scattering at impurities within the glass, or even camera light leakage. Multi-coatings of the lens greatly reduced the magnitude of reflections at the air/glass interfaces of lens elements, but the performance of a coating is not constant over the spectrum and depends on the angle of incidence. When the outline shape of localized flare resembles the shape of the limiting aperture, it is identified as a ghost image. A ghost image is an undesirable image typically of the camera diaphragm opening. It is a form of flare spot and may be removed or reduced by use of an efficient lens hood (Stroebel and Zakia (1993)).

Measurements were done to characterize the optical system. The shortest possible exposures were 0.02 s, due to limitations of the electromechanical shutter (Apogee

Instruments Inc). As a result, an exposure time of 0.025 s was chosen to allow for the use of more f-stops without saturating the pixels when using room lighting. The software used to capture the images was MaxIm DL/CCD, which ran on a Windows platform. The images were saved using the commonly used formats such as JPEG and BMP, but the default format was the FITS (Flexible Image Transport System). The FITS format has extensive support for header information to describe the image and the equipment used. More importantly, it saves the image information in raw format that does not involve loss of information due to compression of data.

## *3.1 Calibration Frames (Dark, Flat and Bias Frame)*

Calibration frames (bias frame, dark frame and flat frame) were taken to correct for different CCD effects. Each pixel had a different bias level when it was read from the CCD. A bias frame is a zero-length exposure with the shutter closed that is subtracted from each image to account for the electronic offset. Dark current produced by thermal effects accumulates at different rates in every pixel, and can lead to large amounts of noise in the image if not compensated for. Dark current can be eliminated or minimised by operating the CCD chip at temperatures below ambient temperature. Cooling can either be done by using a liquid nitrogen dewar or by Peltier cooling. The type of cooling depends on the integration time and minimum acceptable signal-to-noise ratio; the CCD chip in this work was cooled by Peltier cooling. To prevent thermal shock, the temperature of the CCD must be ramped up or down very slowly, allowing about 15 minutes for the required temperature to be reached. The effect of dark current can be reduced by subtracting a dark frame from the image. A dark frame is an equal exposure of the same exposure time as the image to be taken, with the shutter closed, at the same thermoelectric cooler temperature as the light field. It

shows the thermal signal contribution to each image from the CCD itself. Dark frames were taken by covering the camera and lens with a thick black cloth, which was folded to reduce the light reaching the camera. It was then determined how the dark current varied with temperature.

A flat frame is an image of an exposure from a uniform source of light. The flat-field frame accounts for the artefacts in the optical path such as vignetting and dust particles on the lens, as well as differences in light sensitivity of each pixel. Vignetting is the blockage of light rays by a surface other than the aperture and occurs towards the corners of the image. It results from a mismatch between the optical pupil and the field of view of the lens, which may cause the corners of the image field to be darker than the rest of the image. The field of view is the viewable area of the object that fills the camera's sensor, which for this work is the CCD chip. The size of the sensor's active area, together with the working distance between the scintillation screen and the camera's lens, and the optical properties of the lens (in particular the focal length), are important factors in determining the field of view. Generally, under similar conditions, larger sensors give larger field of views. On the other hand, if the lens is not able to support a large CCD chip size a "tunnel effect" results, caused by vignetting with the edges of the field being darker.

The flat frame does not need to be the same exposure length as the normal image, but its pixel values should be about a third of the saturation value in order to have a good signal-to-noise ratio (Diffraction Limited, 2000). If the pixel values are too high or too low this might not improve the quality of the image, or worse, it might even degrade the image quality. A white paper with dimensions greater than $30 \times 30$ cm$^2$

on a black board was used, with the camera at the working distance. Flat images taken using ambient room lighting did not result in a uniform image. A diode ring with green high intensity light emitting diodes (LEDs) was then used. These LEDs where chosen because the CCD was more sensitive to green light. The diode ring was placed around the camera lens. The resultant light falling on the white paper was not uniform as each diode formed a distinctive circular light field of its own. Two 150W halogen filament lamps on either side of camera were then used to uniformly illuminate the white paper, to give a slightly more uniform image. Instead of calibrating the entire optical system it was then decided to calibrate "just the camera", using a method suggested in the MaxIm DL user manual. This was done by making use of a 17.5 cm long black opaque tube of diameter 7.5 cm. One end of the tube was covered with white photocopy paper. The lens was removed from the camera and a tube was then placed in front of the camera, where the lens would have been. Exposures were taken which produced a brightness level of about 30 % of the saturation value. The flat frame was dark-subtracted, normalized and then divided into each image.

## *3.2 Working Distance and the Depth of Field*

The working distance that would allow the image to be covered as much as possible by the object, was then determined. The working distance is the distance from the front of the lens to the object under inspection, and in our application the object is the scintillation screen. For a given lens, the working distance must be chosen so that the image of the object maximally covers the CCD array. The scintillation screen was $30 \times 30$ cm$^2$, and this was accepted as the dimensions of a typical object. Images were taken with the camera at different distances from the object until a distance was

reached that had the object covering almost the whole image. This distance was taken to be the working distance. The working distance was used as a guide for the overall dimensions of the “test rig”. The “test rig” was designed in the form of an “L” shape, and the camera was mounted on it. It consisted of a movable flat metal panel, whose plane was at a 45° angle to the mirror, with the camera mounted on rails as shown in Figure 3.2-1. Alongside the rails was a fixed graduated linear scale to indicate the distance moved by the camera. A white paper with a $30 \times 30$ cm$^2$ square drawn on it was placed on the flat panel. The panel was positioned such that the $30 \times 30$ cm$^2$ square drawing would cover the image. The appropriate position of the camera was noted and this was taken as the zero position. At this position the distance of the camera to the mirror plus the distance of the panel to the mirror corresponded to the working distance. For information on the depth of field refer to section C.2 of Appendix C.

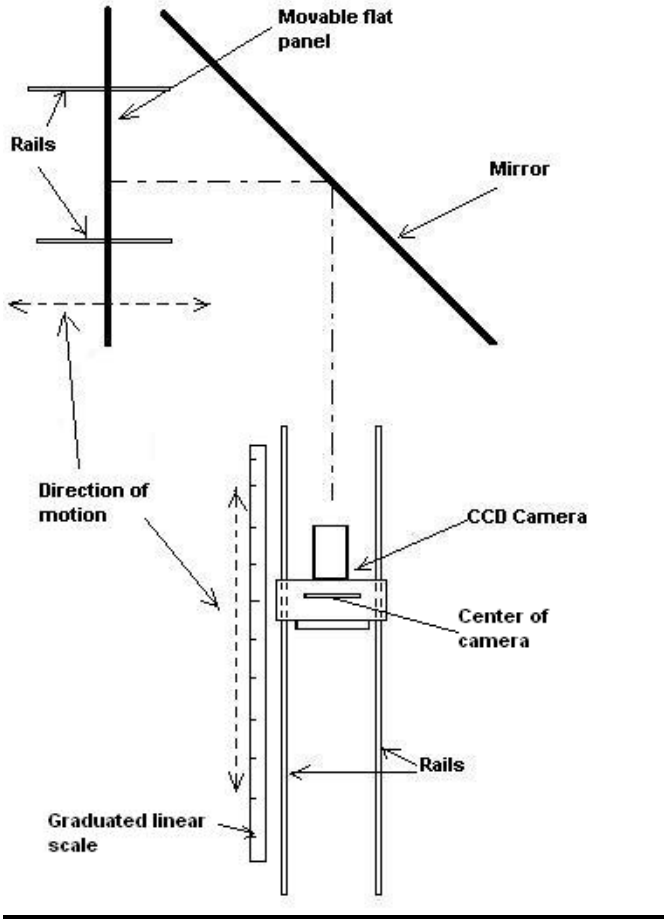



**Figure 3.2-1 A test rig for doing the optical test for the CCD Camera**

The position of the panel and the camera was adjusted, with images taken at different panel and camera positions. For fixed panel and mirror positions, the camera positions were then adjusted until a position was reached that had the object ($30 \times 30$ cm$^2$ square) covering almost the whole image. The distance from panel to mirror was determined to be 375 mm, and the distance from mirror to the center of camera was taken to be 549 mm, giving a working distance of 924 mm. The required minimum mirror size was 220 mm × 220 mm.

To focus the camera a white disc (2 cm in diameter) on a black background was placed in the centre of the flat panel. The full-width at half maximum (FWHM) of the

disc was measured (using the MaxIm DL/CCD software) from images taken of the white disc. The FWHM was used as an indication of how sharply focused the image was. FWHM is a simple measure of the width of a distribution, and was obtained using a built-in tool in MaxIm DL/CCD software. When the camera is focused the white disc would appear bright (indicated by large maximum pixel value) whereas an image of the white disc when the lens is completely out of focus, will be blurred. The lens focus was adjusted by trial and error until a minimum value of FWHM was reached with the largest maximum pixel value. At this minimum value of the FWHM the camera was said to be focused. After the camera was focused, the resolution was then quantified using bar charts, similar to the one shown in Figure 3.2-2.

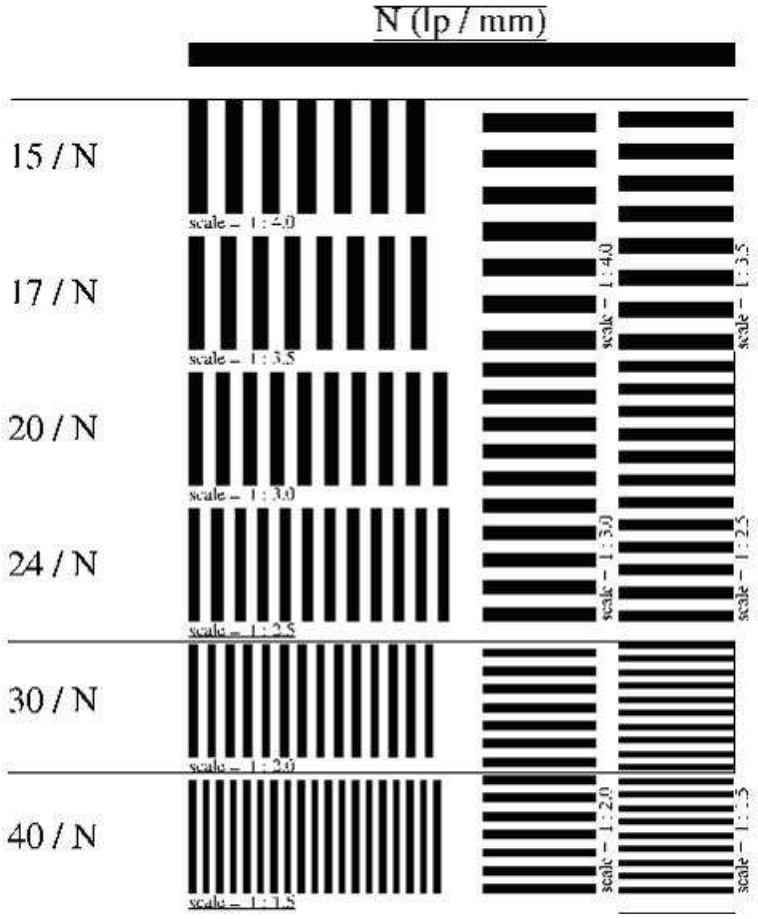



**Figure 3.2-2 Diagram showing the Bar chart test pattern**

Images of different bar charts were taken. The images were taken at a fixed camera position. On reaching the bar chart with the smallest line pairs that could be resolved, the camera was then moved to establish the depth of field. The depth of field is the amount of object movement (in and out of focus), which is allowable to maintain acceptable image focus. It gives an indication of how sensitive the system is to defocusing. The camera was moved as close as possible to the mirror in small increments. At each incremental displacement, images of the line pairs was obtained. The camera was moved up to a point where the line pairs could not be resolved.

## *3.3 Characterisation of Apogee AP47p Camera*

Initial exposures indicated that there were variations in exposures captured under the same conditions. Tests were done to confirm the performance specifications of the AP47p camera as per the data sheet given in Appendix A. The tests used were those in Appendix B as given by Apogee Instruments Inc. (Apogee Instruments, Inc.). Measurements were done with the CCD temperature set to –20 °C, except for the dark count which was done at –27 °C, which was the temperature indicated on the data sheet.

### 3.3.1 Exposure Variation

Three methods were used to acquire flat field images to determine if there was any variation in the flat field images. The camera was set to focus at an object at infinity. A series of at least 5 flat field measurements were taken with different illuminations.

To vary the illumination reaching the camera lens, a different number of sheets of paper were placed on top of the lens hood of the camera. Exposures of 0.1 seconds were made.

The second method involved the camera facing a white background. A light source, whose intensity could be varied using a potentiometer dial, was used to illuminate the room. Nine equally spaced dial positions were marked, ranging from position 0 (brightest dial setting) to position 8 (dimmest dial setting). For the flat field, the dial position 5 was used. The third method entailed taking a sequence of flat frames with the set-up as shown in Figure 3.3-1. A light source was made to shine on the white ceiling to obtain a uniform light field, and the camera was placed upright facing the ceiling. A paper covering was then placed in front of the camera lens. The third method was the method of choice.

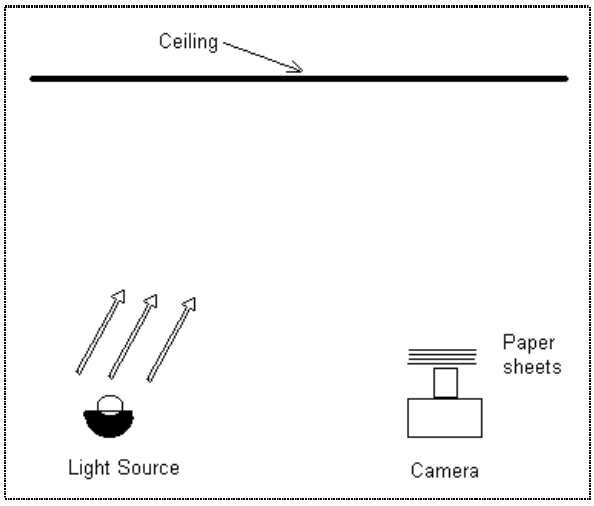



**Figure 3.3-1 A diagram showing the set-up of the light source and the camera.**

The camera was then focused manually. A "bar chart" test pattern (similar to the one shown in Figure 3.2-2) was used as the object to be imaged; it was placed at a

distance of about 86 cm from the camera. Images for varying room illumination were then taken.

### 3.3.2 Linearity

The camera linearity was also verified, where linearity was defined as how consistently the CCD responded to light over its well depth. The well depth is the number of electrons that can be accumulated in each pixel, a typical value being 100 000 with a minimum of 60 000, measured at 253 K and 20 kHz CCD readout speed. The camera was set up as before with only one sheet of paper placed over the camera opening, to produce a uniform light. Exposures were taken for times of 0.0 s to 1.0 s in increments of 0.1 sec, 1.0 s to 2.0 s in increments of 0.2 s and 2.0 s to 5.0 s in increments of 0.5 sec.

### 3.3.3 Signal Variance, Gain

The signal variance was then measured. The method for determining the system's gain in electrons per ADU was used with the camera set-up shown in Figure 3.3-6. The number of photons per ADU indicates how many photoelectrons are required to increase the pixel value by one count. A photoelectron is produced whenever a photon is detected by the pixel. The method involved taking multiple exposures with increasing light, with an exposure time of 0.1 sec. A bias frame was also taken. Standard deviation and mean count data were collected for each image. The variances were then plotted against the net mean signal values. The net mean signal value from the multiple exposures for a particular light intensity was the mean value minus the mean bias value. The slope of the line represented the gain of the system. The mean and standard deviation values were obtained with the cursor positioned at the center

of the image for a region of interest (ROI) of radius 20 pixels (this is the maximum radius that the software allowed), as suggested in the method from Apogee (see Appendix B). The bias level was determined by the mean value of the cursor positioned in the center of the bias frame.

### 3.3.4 System Noise

To determine the system noise, two bias frames were obtained with the CCD temperature set at –20 °C. The standard deviation was obtained from the difference of the two bias frames, which was calculated from the region of interest at the center of the frames. The product of the gain and the standard deviation was taken as the noise in units of electrons.

## *3.4 Lens Coupling Efficiency*

The imaging device uses a lens, which couples the scintillating screen and the CCD chip. The lens coupling efficiency $g_2$ was calculated from equation 3.1

$$g_2 = \frac{Tm^2}{4(F_{\#})^2(1+m)^2 + m^2} \qquad 3.1$$

$T$ is the bulk transmittance of the lens, which is the ratio of the photon energy passing into the image domain to the photon energy falling into the lens aperture at the object domain, $m$ is the system geometrical magnification factor, and $F_{\#}$ is the f-number of the lens. For a more detailed explanation on lens coupling, refer to section C.4 of Appendix C.

## 3.5 Resolution

The spatial resolution of an imaging system is the ability of the system to distinguish between two points as separate and distinct, as they become smaller and closer together. The closer they are, with the image still showing them as separate objects the better the spatial resolution. Spatial resolution is sometimes referred to simply as the resolution. The spatial resolution, expressed in line pairs per millimeter, can be measured with a test object or by the modulation transfer function (MTF). The modulation transfer function indicates the contrast transfer of an image through the system at different frequencies. A test object consisting of a series of regularly spaced bars and spaces will give an indication of the resolution that can be resolved with the system.

In general, the spatial resolution of the digital image is limited by the pixel size of the CCD chip. For a given detector technology the spatial resolution is inversely proportional to the pixel size and is defined as the Nyquist limit which states that the maximum resolution is equal to the inverse of twice the pixel size in millimeters. The system resolution is given by:

$$System\ resolution = \frac{1}{2 \times Effective\ pixel\ size} \quad . \qquad 3.2$$

The units for system resolution are line pairs per millimeter (lp/mm). The effective pixel size is determined by the field of view (FOV), divided by the number of pixels on the CCD chip

$$Effective\ pixel\ size = \frac{Field\ of\ view}{Number\ of\ pixels}\ , \qquad 3.3$$

and the system resolution therefore becomes

$$System\ resolution = \frac{Number\ of\ pixels}{2 \times Field\ of\ view}\ . \qquad 3.4$$

The system resolution is directly proportional to the number of pixels on the CCD chip and inversely proportional to the field of view. More information on the field of view is given in section C.3 of Appendix C.

The prototype of the imaging device is shown in Figure 3.5-1

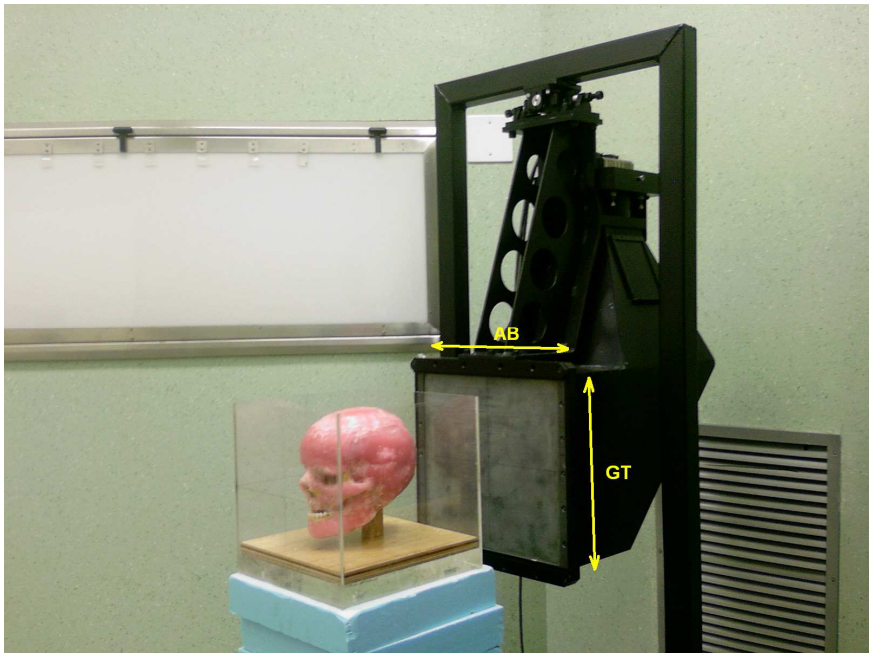



**Figure 3.5-1 The digital x-ray imaging device with a phantom in place**

The theoretical system resolution was determined from the number of pixels and the field of view. The modulation transfer function for the digital camera system was determined by implementing the edge exposure technique. Exposures of a 3 mm thick lead disc were taken. Using the "line profile" tool for MaxIm DL, the pixel values were obtained by tracing the digital image across the disc edge. This was done to obtain the edge spread function (ESF). The ESF was then smoothed and the central difference method was used to obtain the LSF. Taking the modulus of the Fourier Transform gives the MTF of the system. The MTF is obtained from the LSF by using a Fourier Transform function (FFT) and is given by:

$$\mathrm{MTF}(\omega) = \mathrm{FFT}\{\mathrm{LSF}(x)\} \qquad 3.5$$

The Modulation Transfer function MTF(ω), is the line spread function represented in the frequency domain ω where x is the measured distance along the 'line profile'. The Matlab program was used to calculate the MTF.

To determine the resolution of diagnostic film in comparison, exposures of a 3 mm thick lead disc placed in front of the film cassette holder were taken. The processed film was then scanned using a high-resolution flat bed scanner. A "line profile" was obtained by making a trace on the digital image across the disc edge. This was done to obtain the edge spread function (ESF), from which the MTF was calculated giving the resolution at 2 % modulation transfer.

## 3.6 Exposure Synchronisation Card

An electronic card was designed at iThemba LABS to synchronize the mouse click event for the camera to capture an image, and for the x-ray tube to expose. The block diagram for the card is shown in Figure 3.6-1

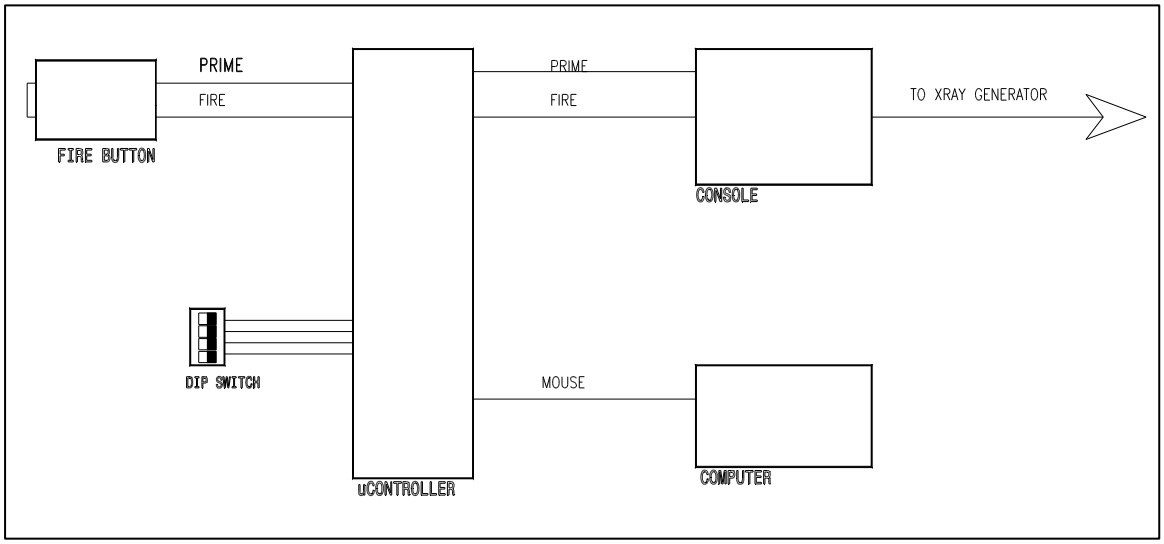



**Figure 3.6-1 A block diagram for micro controller card**

When the "fire button" was pressed for the x-ray tube to expose, the card allowed a mouse-click signal to be sent to the computer controlling the camera, so that the x-ray image was captured at the same time the exposure occurred.

## 3.7 Correction for Lens Distortion

A method was determined to correct for lens distortion. The method used a set of images of a "checker grid" comprising of alternating black and whites squares much like a chessboard, for different camera orientations, i.e. at different angles to the

"checker grid". These images were used to determine the internal and external camera parameters, which were then used to undistort the images. A Matlab toolbox by Bouguet (2004) was used to determine the camera parameters, which are the focal plane, coordinates of principle point, coordinates of the camera center in the world coordinate frame and the orientation of the camera coordinate frame. The toolbox allowed images of a checkerboard to be captured with the camera at different orientations. A corner extraction engine was able to detect the checker square and showed the predicted grid in the absence of distortion. Should the predicted corners not be close to the real image corners, the user was able to manually input a guess for the first order lens distortion coefficient ($k_c$). In practice this value is between –1 and 1. The values used here for the distortion coefficient were only used to help with the corner extraction and did not affect the main calibration step, as they are neither used as the final distortion coefficients nor were they used as the initial guess of the true distortion coefficients. For severely distorted images, manual corner extraction was possible. The calibration was done in two steps. The first step comprised initialisation, which was then followed by non-linear optimisation. Bouguet (2004) states that the initialization step computes a closed-form solution for the calibration parameters. The non-linear optimisation step minimized the total reprojection error (in the least squares sense) over all the calibration parameters. The reprojection error is an error corresponding to the image distance between a projected point and a measured one. It is used to quantify how closely an estimate of a 3D point recreates the point's true projection. Bouguet (2004) states that the optimisation was done by iterative gradient descent with explicit (closed-form) computation of the Jacobian Matrix of the inverse transform of the pixel coordinates. Once the calibration had been done it was possible to analyse the reprojection error and see which points had the corresponding large

reprojection error in pixels (where the pixel error was the standard deviation of the reprojection error in pixels in both the x and y directions respectively). In cases where the corners had been badly extracted the user was able to recompute the corners of the specific images using different window sizes.

A Matlab routine was initially written to correct the images for distortion. The distortion correction for this routine was based on an approach using control points obtained from a reference image. The reference image was an image of a checker board of known spacing between the white and black squares. The "ideal" coordinate position of the control points (x, y) are obtained by considering the corners of the squares in the center of the image, as these were assumed to be undistorted. The pixel coordinates (x,y) undergo geometric distortion to produce an image with coordinates ($u$, $v$). The distortion was then modeled using the following bilinear equations:

$$u = c_1 x + c_2 y + c_3 xy + c_4 \tag{3.6}$$

$$v = c_5 x + c_6 y + c_7 xy + c_8 \tag{3.7}$$

Taking 4 pairs of control point coordinates we get:

$$\begin{bmatrix} u_1 \\ v_1 \\ u_2 \\ v_2 \\ u_3 \\ v_3 \\ u_4 \\ v_4 \end{bmatrix} = \begin{bmatrix} x_1 & y_1 & x_1y_1 & 1 & 0 & 0 & 0 & 0 \\ 0 & 0 & 0 & 0 & x_1 & y_1 & x_1y_1 & 1 \\ x_2 & y_2 & x_2y_2 & 1 & 0 & 0 & 0 & 0 \\ 0 & 0 & 0 & 0 & x_2 & y_2 & x_2y_2 & 1 \\ x_3 & y_3 & x_3y_3 & 1 & 0 & 0 & 0 & 0 \\ 0 & 0 & 0 & 0 & x_3 & y_3 & x_3y_3 & 1 \\ x_4 & y_4 & x_4y_4 & 1 & 0 & 0 & 0 & 0 \\ 0 & 0 & 0 & 0 & x_4 & y_4 & x_4y_4 & 1 \end{bmatrix} \begin{bmatrix} c_1 \\ c_2 \\ c_3 \\ c_4 \\ c_5 \\ c_6 \\ c_7 \\ c_8 \end{bmatrix} \tag{3.8}$$

Which can be written as

$$[X'Y'] = [M][C] \tag{3.9}$$

To solve for the bilinear coefficients $c_1$, ……, $c_8$, equation 3.9 becomes

$$[C] = [M]^{-1}[X'Y'] \tag{3.10}$$

To assign the grey level value to the pixel(x, y) in the corrected image bilinear interpolation was used. The interpolation was done between the four pixels nearest to $(\tilde{u}, \tilde{v})$ in the distorted image as shown in Figure 3.7-1.

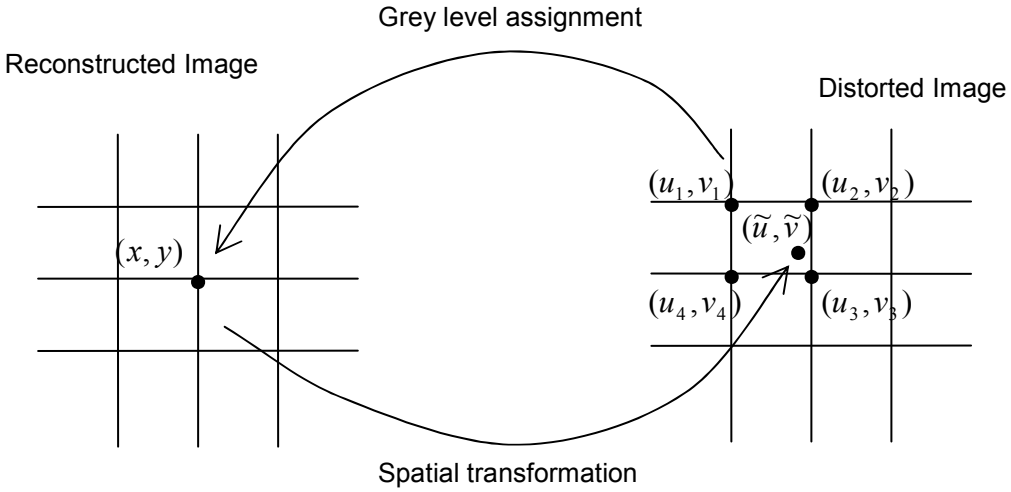



**Figure 3.7-1 A diagram illustrating bilinear interpolation**

The gray-level was given by equation

$$f(u_i, v_i) = au_i + bv_i + cu_i v_i + d\,, \tag{3.11}$$

where $f(u_i, v_i)$ is the grey value at position $(u_i, v_i)$. The interpolation coefficients (*a*, *b*, *c*, *d*) are found by solving equation 3.12

$$\begin{bmatrix} f(u_1, v_1) \\ f(u_2, v_2) \\ f(u_3, v_3) \\ f(u_4, v_4) \end{bmatrix} = \begin{bmatrix} u_1 & v_1 & u_1 v_1 & 1 \\ u_2 & v_2 & u_2 v_2 & 1 \\ u_3 & v_3 & u_3 v_3 & 1 \\ u_4 & v_4 & u_4 v_4 & 1 \end{bmatrix} \begin{bmatrix} a \\ b \\ c \\ d \end{bmatrix} \tag{3.12}$$

The grey level to assign pixel $(x, y)$ in the reconstructed image is then calculated using equation 3.13

$$f(x, y) = a\tilde{u} + b\tilde{v} + c\tilde{u}\tilde{v} + d \tag{3.13}$$

## 3.8 Optical Scatter

Experiments similar to those discussed by Partridge *et al.* (1999) were done to determine the effects of optical scattering. The experiments required the use of material with a surface finish, which had a reflectance similar to that of the scintillation screen. A number of sheeting materials made from either plastic or paper, which were assumed to have a similar reflectance as the scintillation screen, were collected. The plastic and paper samples were white in colour all having a smooth finish that was similar to that of the scintillation screen. Non-destructive Zygo interferometery tests (an alternative to using an integrating sphere) were conducted on the scintillation screen and samples of the different sheeting materials to determine their reflecting properties.

The specular reflectance as indicated in Figure 3.8-1, is a surface property of the material, namely the refractive index and the surface roughness (Bhushan, 1999). Surface roughness scatters the reflected light, thus affecting reflectance. The correlation between specular reflectance, $R$, and the surface roughness, $\sigma$, is described by (Beckmann and Spizzichino, 1963)

$$\frac{R}{R_0} = \exp\left[-\left(\frac{4\pi\sigma\cos\theta_i}{\lambda}\right)^2\right] \approx 1-\left(\frac{4\pi\sigma\cos\theta_i}{\lambda}\right)^2 \quad , \qquad 3.14$$

where $\theta_I$ is the angle of incidence measured with respect to the sample normal and $R$ is the specular reflectance. The total reflectance $R_0$ is given by

$$R_0 = \frac{P_S}{P_0} \quad , \qquad 3.15$$

where $P_S$ is the total backscattered light power, and $P_0$ is the incident light power (Hummel *et al.,* 1995)

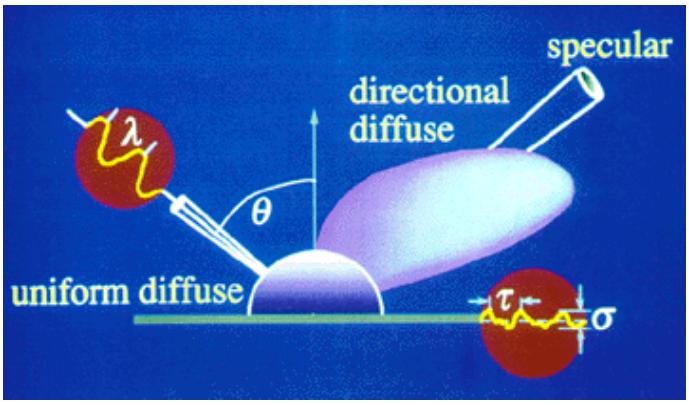



**Figure 3.8-1 An illustration of the components of a light reflection model, showing incoming light and outgoing diffuse, directional diffuse, and specular reflections**

### 3.8.1 Zygo Experiment

A MetroPro Zygo interferometer was used to determine the reflectance of the various white paper and plastic samples. The interferometry used a helium light source with a wavelength of about 632 nm, which was the same order as the light emitted by the scintillation screen.

To determine the surface properties of the samples, the following parameters were used: the maximum peak-to-valley height (*PV*), the root-mean-square (*RMS*) roughness, the arithmetical mean deviation (*Ra*). The maximum peak-to-valley height (*PV*) was taken as the absolute value between the highest and lowest peaks and is given by the expression $PV = R_P + R_V$, where $R_P$ is the maximum distance between the highest point and the mean, and $R_V$ is the minimum distance between the lowest point and the mean, as indicated in Figure 3.8-2

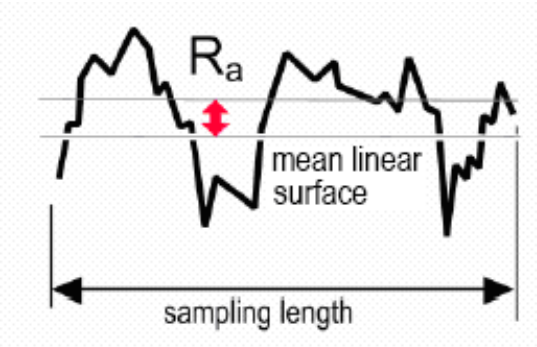



**Figure 3.8-2 An illustration of the Maximum peak-to valley height**

The root-mean-square (*RMS*) roughness was the measured height deviations taken within the evaluation length or area and measured from the mean linear surface. The mean linear surface is defined such that equal "areas" of the surface lie above and below it. The arithmetic mean deviation ($R_a$) was the average roughness or deviation of all points from a plane fitted to the test part of the surface, as shown in Figure 3.8-3.

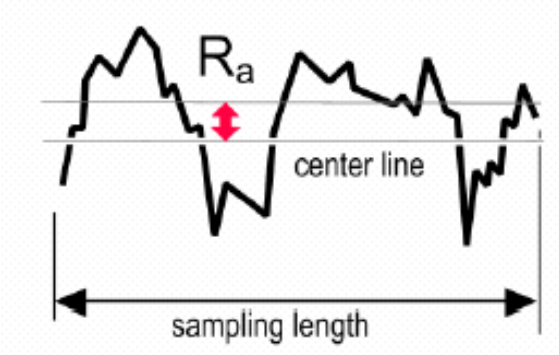



**Figure 3.8-3 An illustration of the arithmetic mean deviation**

### 3.8.2 Optical Scatter Experiments

Experiments to determine the optical scattering, similar to those discussed by Partridge *et al.*(1999) were conducted. Strips of width 1.5 cm, 3 cm, 6 cm, 10 cm and 20 cm were used. The strips were placed in contact with the screen along the central

axes in both the GT (in-plane) direction and the AB (cross-plane) direction (as indicated previously in Figure 3.5-1). Two sets of strips were used, one being made of paper from which sample 6 was cut from and the other of plastic from which sample 7 was cut from. Measurements of the scattered light were made by taking a line profile along the center of the strip, on the x-ray images taken with the different strips in place.

To determine optical scatter for different field sizes of 10 cm × 10 cm, 15 cm × 15 cm, 20 cm × 20 cm and 25 cm × 25 cm, masks were placed in front of the scintillation screen instead of varying the radiation field output. An exposure setting of 77 kV, 250 mA and 50 ms was used for an exposure of 0.2 seconds, for a field size of 35 cm × 35 cm, which was chosen to cover the front of the imaging device.

#### 3.8.2.1 Anti-Scatter Grid

To prevent scattered light emitted by the scintillation screen from reflecting back onto the screen, Partridge *et al.* (1999) suggested the use of a louvre computer "privacy filters" from 3M Corporation, which are normally used on computer screens. The film is composed of thin opaque strips with a pitch of about 0.1 mm, embedded in a polycarbonate matrix. The film has a transmission of 75 % normal to sheet, which reduces to 35 % at an angle of 15° and cut off completely at 30°. The 3M louvre film was placed in direct contact with the scintillation screen and a 1.5 mm strip was placed between the scintillation screen and the film. To determine the glare, line profiles were extracted from the central axis. Filtered images of the skull phantom were also obtained and these were compared to the images without the filter.

## 3.9 X-ray Imaging and Pixel Binning

The use of pixel binning can be employed to reduce the dose to the patient. Pixel binning is a technique that increases the sensitivity of the CCD. The technique allows for adjacent pixels to be summed together into a "super pixel" (as illustrated in Figure 3.9-1), which has better signal to noise ratio.

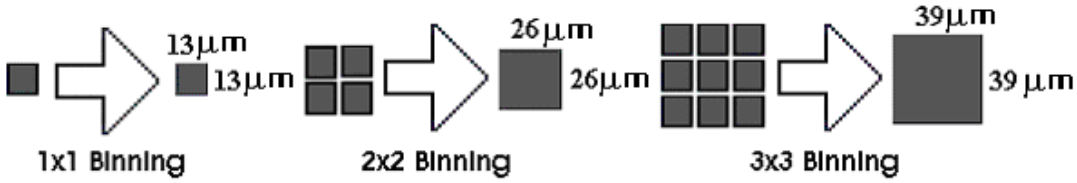



**Figure 3.9-1 An illustration showing pixel binning.** *This effectively increases the pixel size while also increasing the sensitivity.*

For the 13 mm × 13 mm CCD having 13 × 13 $\mu m^2$ square pixels a binning of 2 × 2 would give a "super pixel" of 26 × 26 $\mu m^2$; a binning of 3 × 3 would give a "super square pixel" of 39 × 39 $\mu m^2$ and so on.

X-ray images of a human skull filled and covered with wax were obtained using the imaging device. A series of exposures were taken for different binning settings. Exposures for binning settings of 1 × 1, 2 × 2, 3 × 3 up to 6 × 6 were made to determine the effect of pixel binning. To give an indication of the effect of body tissue on the image quality, a series of exposures were done for varying thicknesses of perspex slabs mimicking body tissue, with a maximum thickness of 6 cm placed in front of the skull phantom.

## *3.10 Shielding (MCNPX)*

The CCD camera would be used in a radiation environment. As a result, the housing for the camera should shield the camera against scattered x-rays, neutrons and proton irradiation and against secondary gamma-ray exposure. The appropriate shielding for the camera was verified by carrying out Monte Carlo simulations. In general, Monte Carlo codes are software algorithms used for solving various kinds of computational problems by using random number generators. The MCNPX (Monte Carlo N-Particle eXtended) software, from Los Alamos National Laboratory was used for the shielding simulations. MCNPX is a general-purpose Monte Carlo radiation transport computer code that can be used to transport nearly all sub–atomic particle types, to nearly all energies, and to nearly all applications (Hendricks *et al.*, 2005). It uses the latest nuclear cross section libraries and uses physics models for particle types and energies where tabular data are not available.

The geometry for the MCNPX simulation consisted of the horizontal proton beam line with its beam elements such as the energy degrader, range modulator, multi-wire ionization chamber, ionization chamber, dose monitor chambers, and collimator, as shown in Figure 3.10-1 below. The beam components indicated in Figure 3.10-1 were made of the materials in Table 3.10-1.

**Table 3.10-1 Properties of materials used for the beam components.**

| Material | Density | Atomic fraction | Weight fraction |
|---|---|---|---|
| Lead | 11.3 | | |
| Phelonic resin | 1.07 | 7 (carbon)<br>6 (Hydrogen)<br>2 (Oxygen) | |
| Graphite | 1.86 | | |
| Brass | 8.90 | | |
| Standard concrete | 2.45 | | 0.529 (oxygen)<br>0.001 (carbon)<br>0.016 (sodium)<br>0.034 (aluminium)<br>0.337 (silicon)<br>0.002 (magnesium)<br>0.073 (potassium)<br>0.0044 (calcium)<br>0.014 (iron) |
| Steel | 7.80 | | 0.005 ( carbon)<br>0.995 (Iron) |
| Water | 1.00 | 2 (hydrogen)<br>1 (oxygen) | |
| Perspex | 1.18 | 5 (carbon)<br>8 (hydrogen<br>2 oxygen | |
| Air | 0.001225 | | |

The proton beam had a Gaussian energy distribution with a mean energy of 200 MeV and the FWHM of 1.2MeV, a 10 cm × 10 cm fixed brass collimator and a patient collimator with a diameter of 5 cm were used, these being the last two collimators in the beam set-up.

To simulate the patient the geometry also included a $30 \times 30 \times 30$ $cm^3$ water phantom, whose center was positioned at the isocenter. The geometry also included the x-ray imaging device, which was positioned 2 m from the isocenter in the beam

direction, with the center of the CDD sensor 2 m above the axis of the beam line, simulating the position the device could be in when the beam is in the treatment vault.

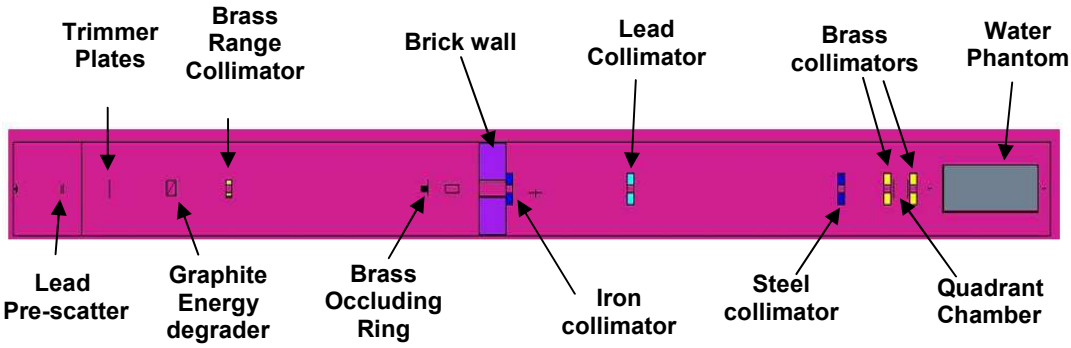



**Figure 3.10-1 Illustration showing the relative positions of the various beam elements that were included in the Monte Carlo simulations**

The geometry for the imaging device is shown in Figure 3.10-2. The device was constructed from 3.5 mm thick aluminium. It also included a 10 mm thick steel casing that was attached to the box in which the camera was housed. The simulations were conducted to determine whether additional shielding was required for the protection of the CCD chip. The simulations were done on a Microsoft Windows computer with a 1.86 GHz Intel processor.

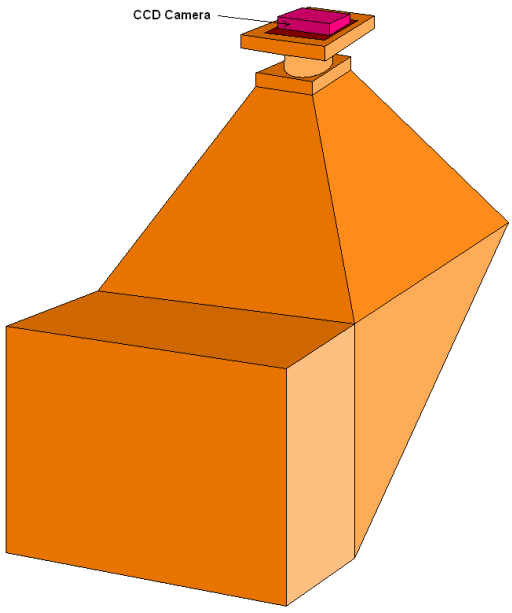



**Figure 3.10-2 An illustration of the geometry of the x-ray imaging device.**

# CHAPTER 4 RESULTS AND DISCUSSION

## *4.1 Calibration Frames (Dark, Flat and Bias Frame)*

The variation in the dark current with temperature was determined. This was done by plotting the average pixel values against temperature, without considering the bias offset. A plot was also done with the bias offset for a range of temperatures as shown in Figure 4.1-1. Bias current variation with temperature was also determined.

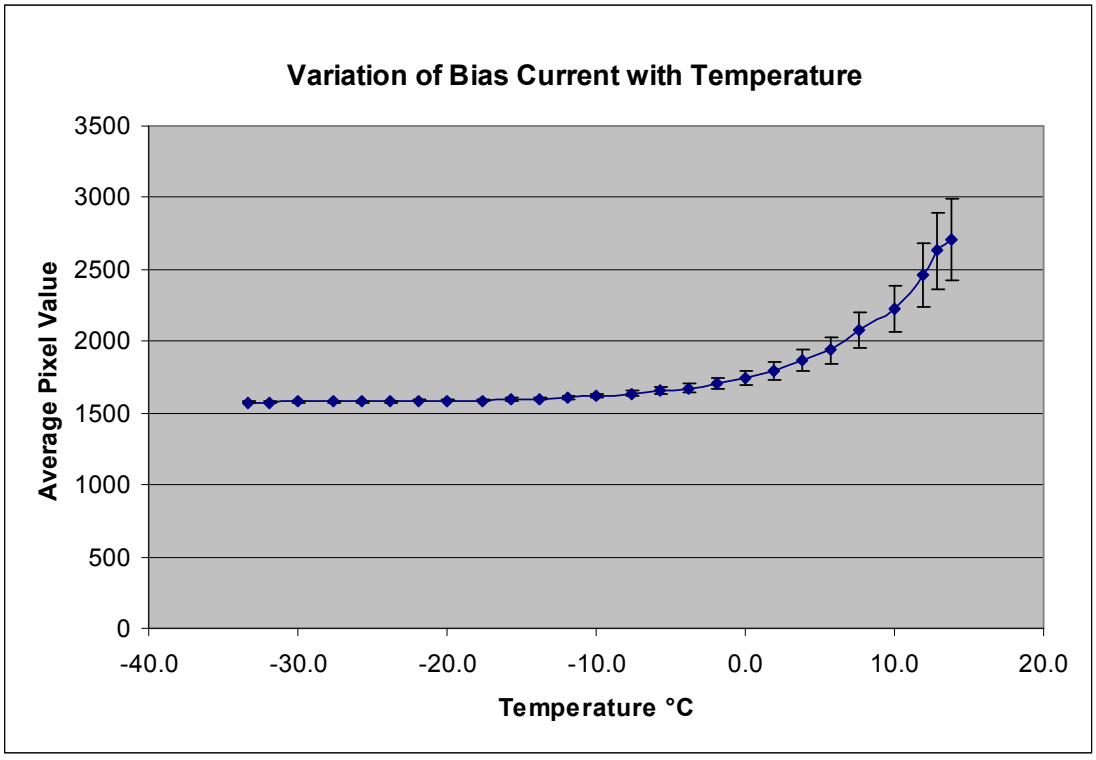
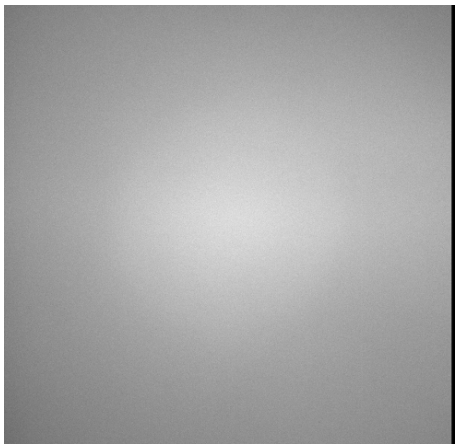


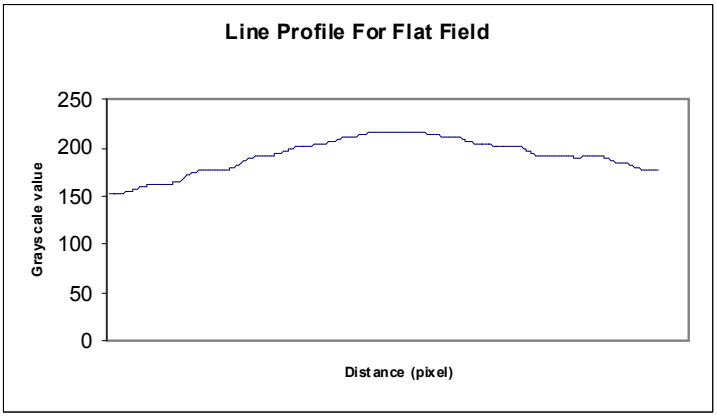

**Figure 4.1-1 The variation of bias current with temperature** *(Values used are for corrected images.)*

It was noticed that for the dark and bias frames the images had a "shading/gradient effect" getting lighter from top to bottom; the cause of which could not be determined The brightness gradients could be due to a slight build-up of thermal charge in the vertical registers during image download from the CCD. The biasing was changed but

this did not affect the observed "gradient effect". Typical images from some of these frames are shown in Figure 4.1-2 to Figure 4.1-4.



**(a)**




**(b)**

**Figure 4.1-2 (a) A typical flat frame. (Temperature is at –20$^{o}$C) (b) An illustration of a line profile of flat frame**

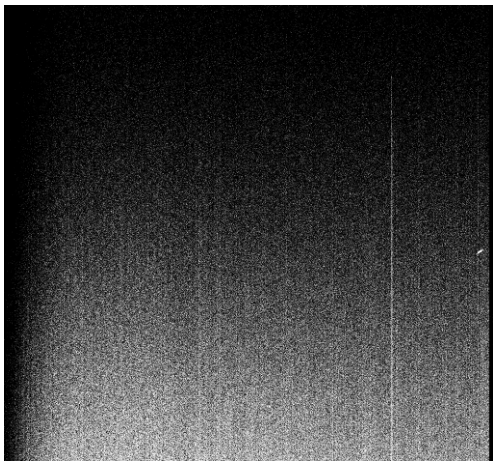


**Figure 4.1-3 A typical bias frame. (Temperature is at –20$^{o}$C)**

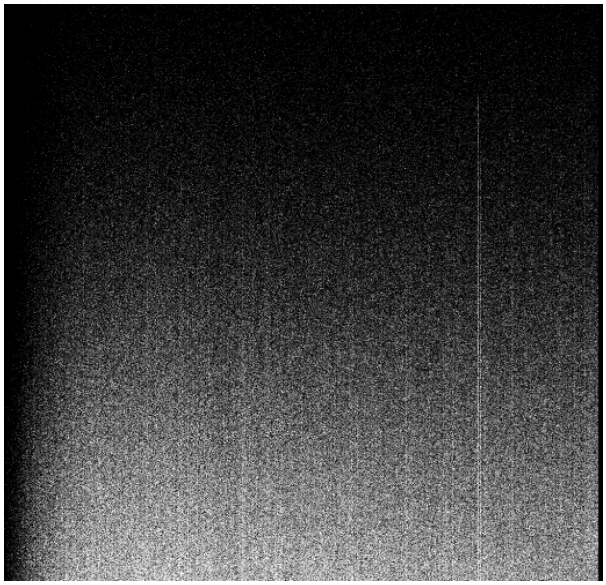


**Figure 4.1-4 A typical dark frame. (Temperature is at –20$^{o}$C)**

It can be seen that for the flat frames there is an increase in brightness (an increase of about 43%) in the centre of the image. This effect could be due to vignetting.

When taking measurements for establishing the variation of dark current with temperature, both corrected and un-corrected images were used. The un-corrected images were the raw images for which bias, flat and dark frames were not applied. The calibration frames were applied on the corrected images. The plots for the two sets of images are shown in Figure 4.1-5 to Figure 4.1-7. The pixel value is the read out from the CCD as a voltage of the order of microvolts per electron. The voltage is proportional to the charge produced by thermal processes occurring in the chip collected. The thermally produced charge gives rise to dark current.

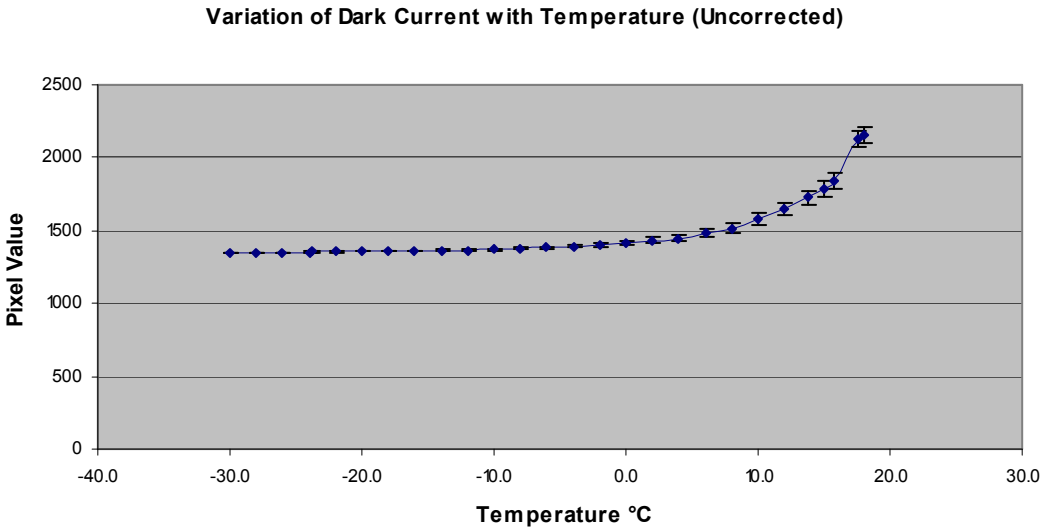



**Figure 4.1-5 The variation of dark current with temperature.** *(The values used are for uncorrected images.)*

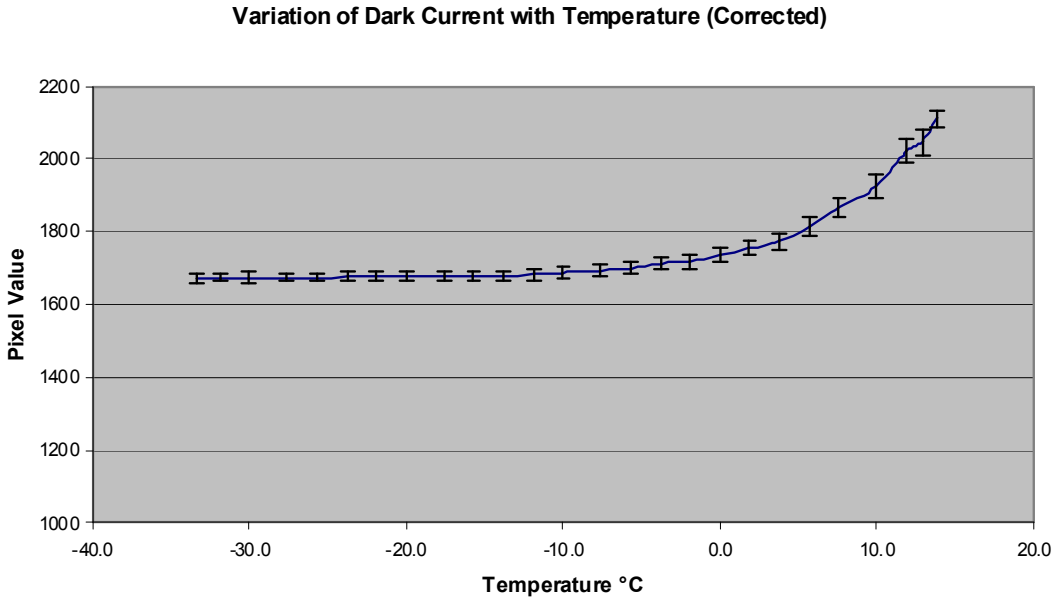



**Figure 4.1-6 The variation of dark current with temperature.** *(The values used are for corrected images.)*

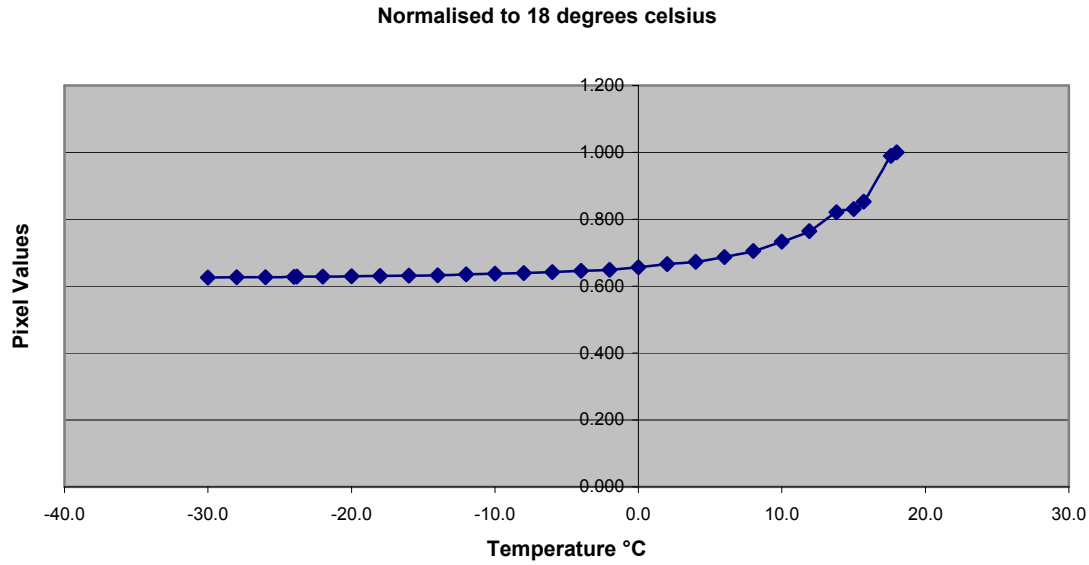



**Figure 4.1-7 The variation of dark current with temperature.** *(The values used are for un- corrected images normalized to 18 $^{o}$C, which was taken to be the ambient temperature.)*

It can be seen that below –5 $^{o}$C, any further decrease in temperature does not result in a significant decrease in pixel value. The temperature of, –20 $^{o}$C was taken to be the operational temperature for all subsequent images.

## *4.2 Working Distance and the Depth of Field (DOF)*

When the camera is focused the image of a 2 cm diameter white disc on a black background would appear bright (indicated by large maximum pixel value) whereas the image when the lens is completely out of focus, will be blurred. The lens focus was adjusted by trial and error until a minimum value of FWHM was reached with the largest maximum pixel value. At this minimum value of the FWHM, the camera was said to be focused. Figure 4.2-1 shows how the FWHM varied as the camera was moved once it was focused. This was expected as it correlates with the DOF

measurements which allow for the camera to remain focused for slight movements towards and away from the object in focus.

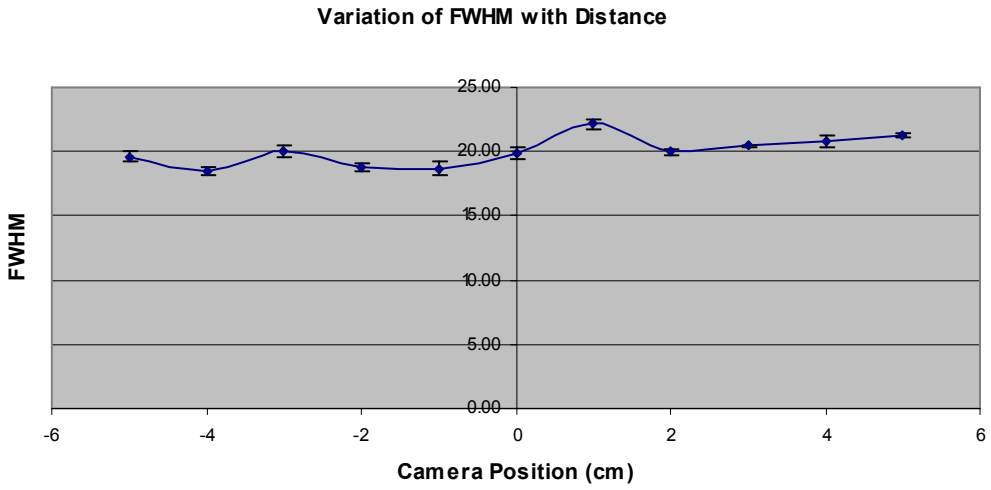



**Figure 4.2-1 The variation of FWHM with distance using a 2 cm white disc.**

After the camera was focused, the resolution was then quantified using bar charts. The distance at which all the line pairs could be resolved was measured to be 0.86 m.

Initially a white disc on a black background was used to determine DOF. However, this method was abandoned, as the results were not conclusive as shown by the variation in the maximum pixel values in Figure 4.2-2. The variation was random, and was therefore abandoned as a measure to determine whether the camera was focused.

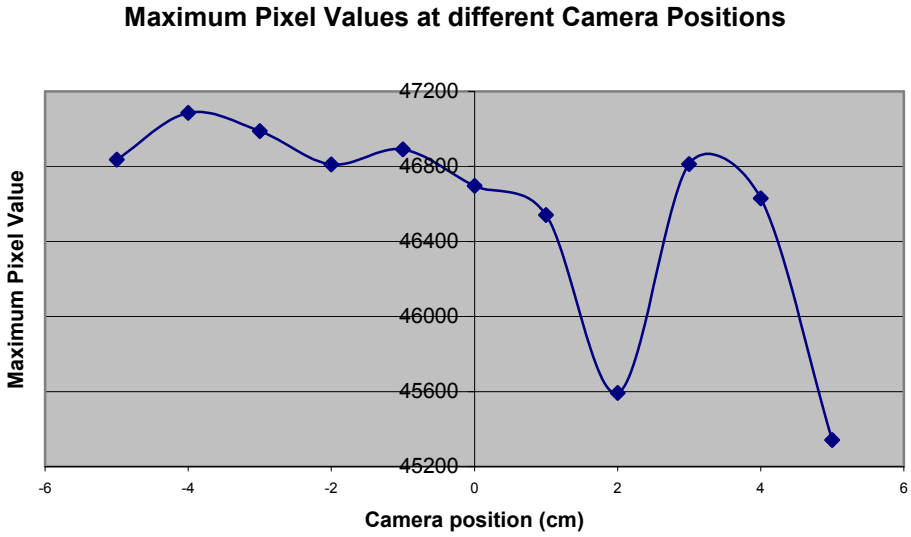



**Figure 4.2-2 The variation of maximum pixel value with distance.**

The calculated DOF for the various aperture f-stops with the lens focused at a distance of 0.86 m (which is different from the working distance of 0.924 m), is shown in Figure 4.2-3. The values for the near focus and far focus shown in Figure 4.2-3 and Table 4.2-1 were calculated for the lens focal length of 36 mm, and the calculated circle of confussion of $1.0627 \times 10^{-5}$ (in 35 mm terms) (see Appendix C). The range for the near focus is indicated by the orange region, with the yellow region indicating the range for the far focus. The depth of field was the sum of the orange and yellow region. It can be seen that at bigger f-numbers the camera is easier to focus, as the range at which it remains in focus is longer.

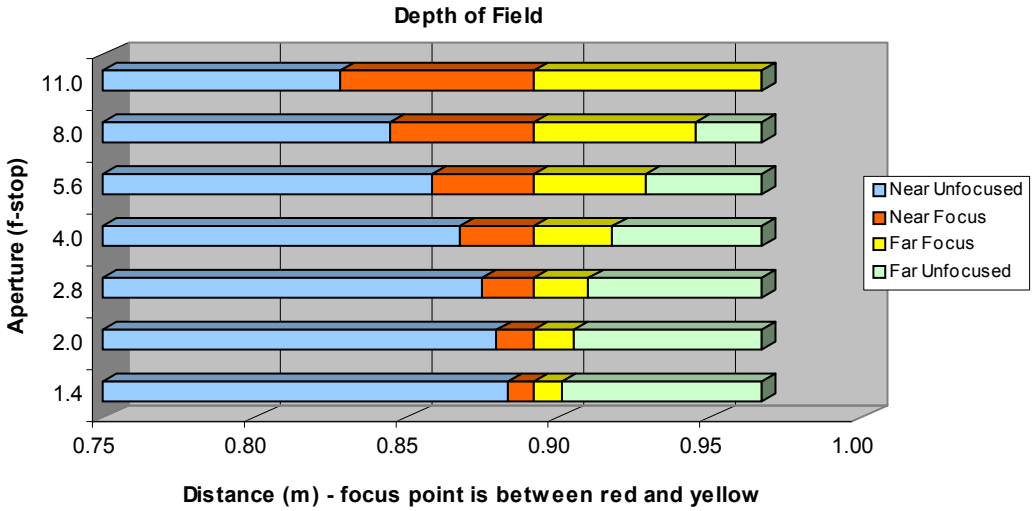



**Figure 4.2-3 An illustration of DOF for the various f-stops**

Table 4.2-1 shows the calculated values for the hypofocal distance, near focus and far focus at different apertures, which gives an indication of the DOF. Table 4.2-1 is a tabulated form of Figure 4.2-5.

**Table 4.2-1 Calculated values for hypofocal distance, near focus and far focus at different apertures.**

| Aperture | Hyperfocal Distance (m) | Near Focus(m) | Far Focus (m) |
|---|---|---|---|
| 1.4 | 87.11 | 0.88 | 0.90 |
| 2.0 | 60.98 | 0.88 | 0.90 |
| 2.8 | 43.56 | 0.87 | 0.91 |
| 4.0 | 30.49 | 0.87 | 0.92 |
| 5.6 | 21.78 | 0.86 | 0.93 |
| 8.0 | 15.24 | 0.84 | 0.95 |
| 11.0 | 11.09 | 0.83 | 0.97 |

## 4.3 Characterisation of Apogee AP47p Camera

### 4.3.1 Exposure Variation

A series of flat frames were taken. On visually inspecting the histograms for the flat frames, there generally appeared to be no significant shift in the position of the histogram profile or a change in the shape when comparing flat frames of similar exposure settings and illuminations. However there were instances (5 cases out of the 200 exposures taken, which are referred to as Flat1, Flat2 etc), where there appeared to be a notable variation of the histogram profile, with the most noticeable variation being that shown in Figure 4.3-1 and Figure 4.3-2. Figure 4.3-1 is typical of the other 195 exposures that were taken. The mean pixel value differs by 0.22 % and the standard deviation differs by 0.05 %, with the only notable difference being in the maximum pixel value with that for Flat3, which was about 58 % higher. It could not be determined why there was a shift in the histogram for Flat3, or any of the other histograms in the 5 incidences, furthermore the manufacturer does not give a specification for this failure rate.

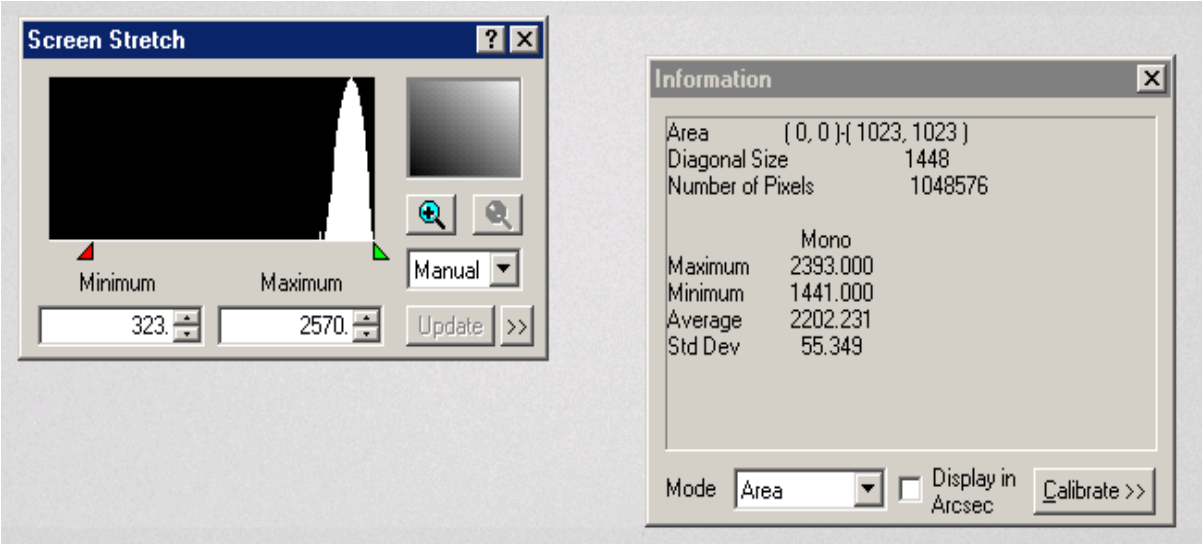



**Figure 4.3-1 An illustration of the flat frame, Flat1, with photons per ADU setting of 10.**

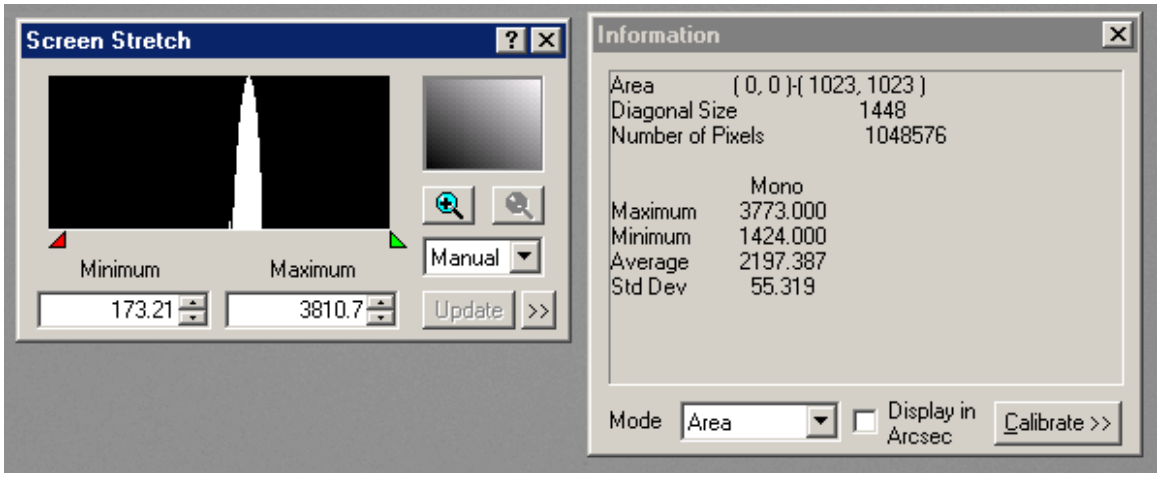



**Figure 4.3-2 An illustration of the Flat frame, Flat3, with photons per ADU setting of 10.**

A plot of the histograms is shown in Figure 4.3-3. The plot of Flat2 and Flat3 is typical of the other 195 flat frames that were taken. The full width at half maximum of Flat1 is about 33 % bigger than that of Flat3. From the plots in Figure 4.3-3, it seemed as if the exposure time was more than double that of Flat2 and Flat3. This could have been due to the electro-mechanical shutter not responding fast enough to give the required exposure time of 0.1 seconds.

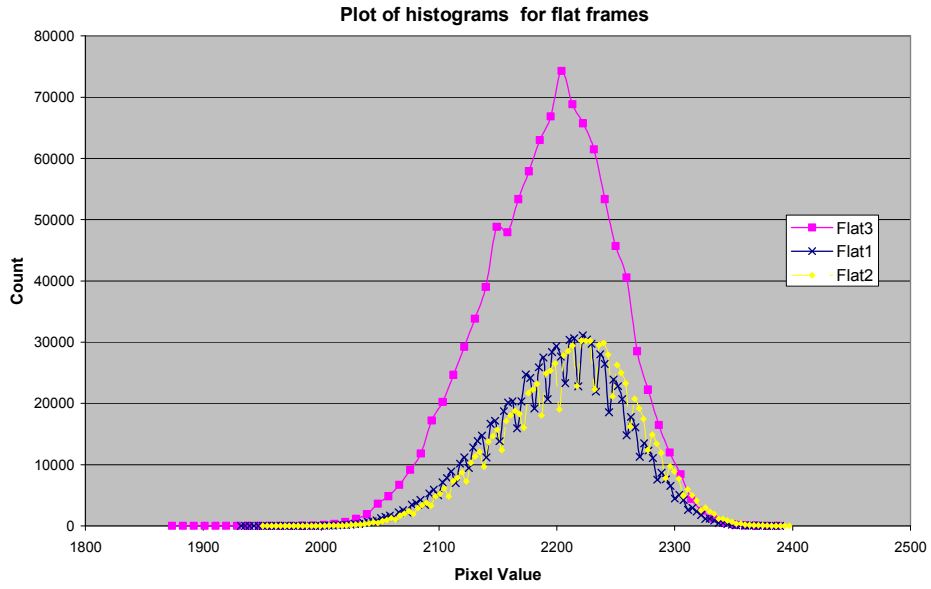



**Figure 4.3-3 A plot of flat frame histograms**

### 4.3.2 Linearity

The linearity of the camera is shown in Figure 4.3-4. A plot of the pixel value in electrons against exposure time in seconds was linear and regression resulted in a coefficient of determination of 0.9995. The error in the data was of the order of 1.4 %.

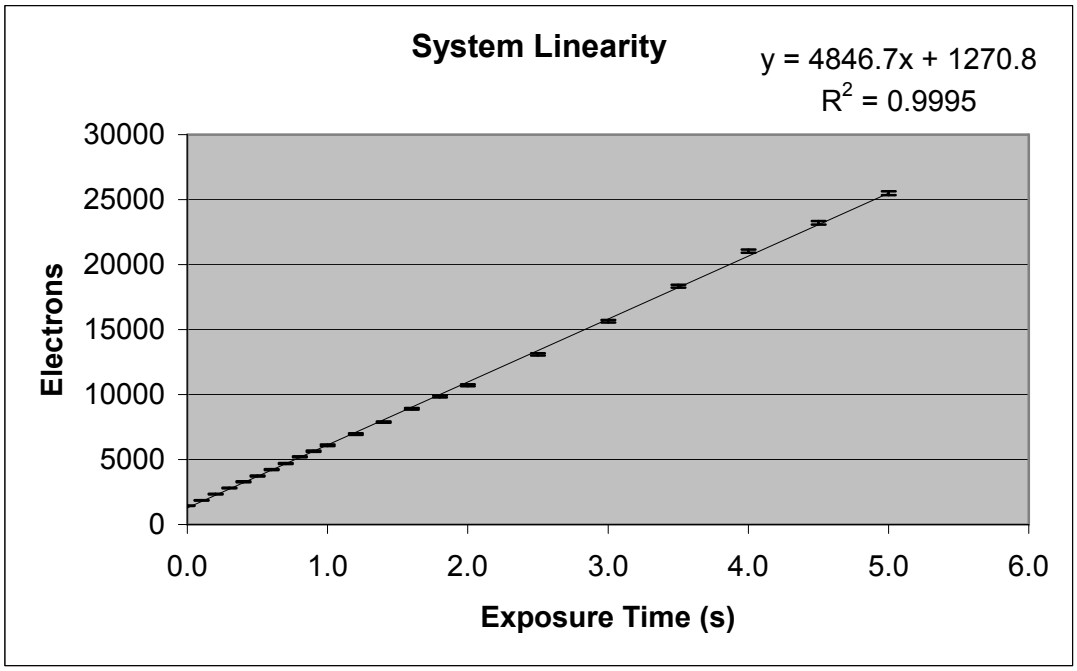



**Figure 4.3-4 A plot of the system linearity.**

### 4.3.3 Signal Variance, Gain

As seen in Figure 4.3-5, the measured gain was 0.7 compared to that reported on the data sheet of 1.3. The bias level was for information only and was determined by the mean value of the cursor positioned in the center of the bias frame. The mean value obtained was 1372 ±5 compared to 2310 on the Test Data Sheet.

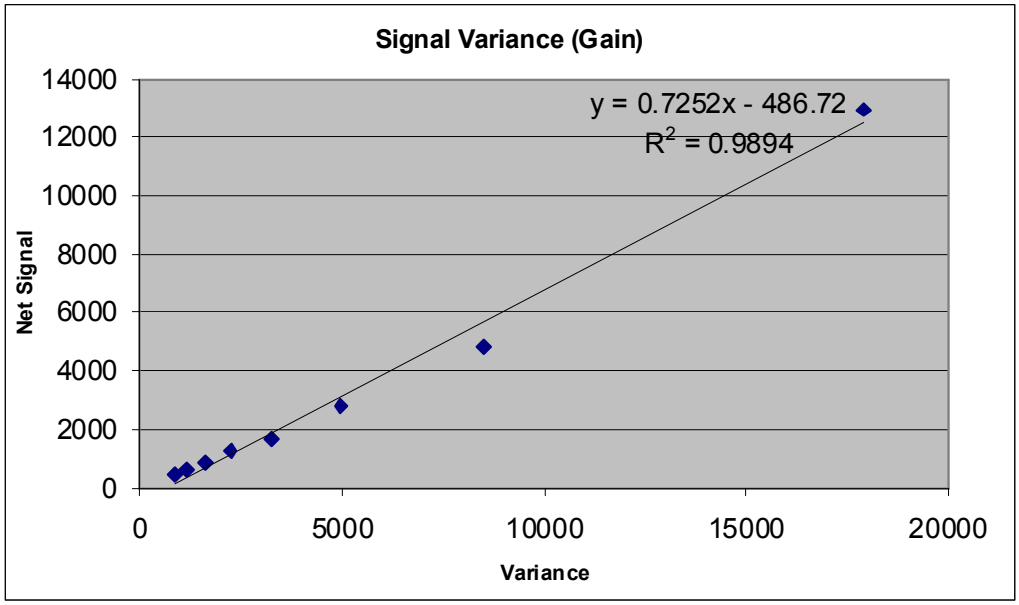



**Figure 4.3-5 A plot of the signal variance**

This difference was probably due to the simplified method of measurement.

### 4.3.4 System Noise

The product of the gain and the standard deviation was taken as the noise, in units of electrons. The standard deviation of the difference of the two bias frames was calculated to be 1.5, giving a noise level of 1.1 ±0.1 electrons. The standard deviation on the data sheet was given as 5.1, with a noise level of 6.4, differing by a factor of almost 6.

There was no agreement between the results from the measurements with those reported on the "Test Data Sheet" as shown in Table 4.3-1. The measured parameters were generally much lower than those stated in the data sheet. The discrepancy might arise from the different test conditions in which the measurements were conducted. This could not be confirmed by Apogee.

**Table 4.3-1 Comparison of results from Camera Test Data Sheet with those from measurements.**

| System Noise | Data Sheet | Measurement |
|---|---|---|
| GAIN | 1.3 | 0.7 |
| SDEV | 5.1 | 1.5 |
| n(e-) | 6.4 | 1.1 |
| | | |
| **Bias Level Setting** | 2310 | 1372 |
| | | |
| **Dark count** | | |
| Net Count (e/s) | 0.56 | 0.24 |

## *4.4 Lens Coupling Efficiency*

The lens coupling efficiency was calculated using the maximum aperture of f/1.4, a CCD imaging area of 13.3 mm × 13.3 mm, scintillating area projected onto CCD i.e. the field of view as 300 mm × 300 mm, the demagnification m = 13.3/300 = 0.044 and taking T = 0.8. The lens coupling efficiency was calculated to be 8.4 %. Assuming T = 1, which is the maximum attainable bulk transmission, the efficiency is given as $g_2 = 10.5$ %.

It has been suggested that the light capture efficiency of the system can be greatly improved by using other optical coupling devices such as fibre optic reducers. An option for fibre-optic coupling is available for the CCD chip that was used.

## 4.5 Resolution

The theoretical system resolution was determined from the number of pixels and the field of view. The CCD consisted of an array of 1024 by 1024 pixels. For a field of view of 300 × 300 $mm^2$ the system resolution was 1.7 lp/mm. The system resolution could be increased by reducing the field of view, and this can be achieved by shortening the distance between the scintillating screen and the camera.

Using the "line profile" tool for MaxIm DL, the edge spread function (ESF) was obtained. The ESF is shown in Figure 4.5-1.

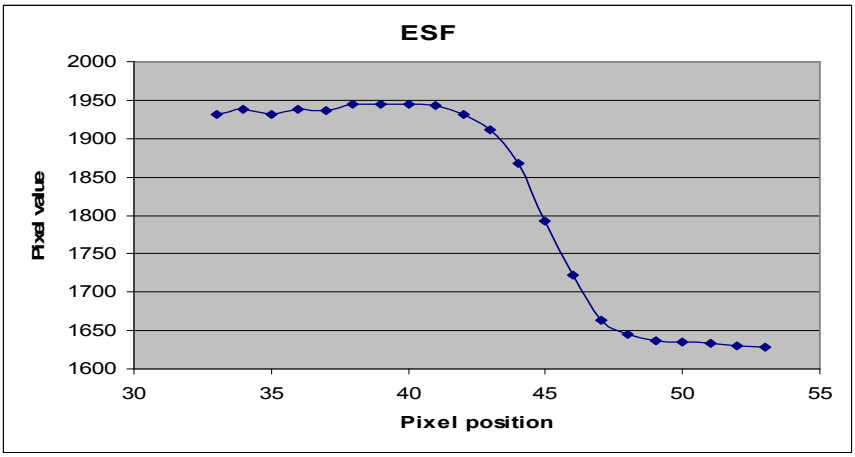



**Figure 4.5-1 A plot of the measured edge spread function for the digital x-ray image.**

The line-spread function (LSF) obtained from the ESF is shown in Figure 4.5-2.

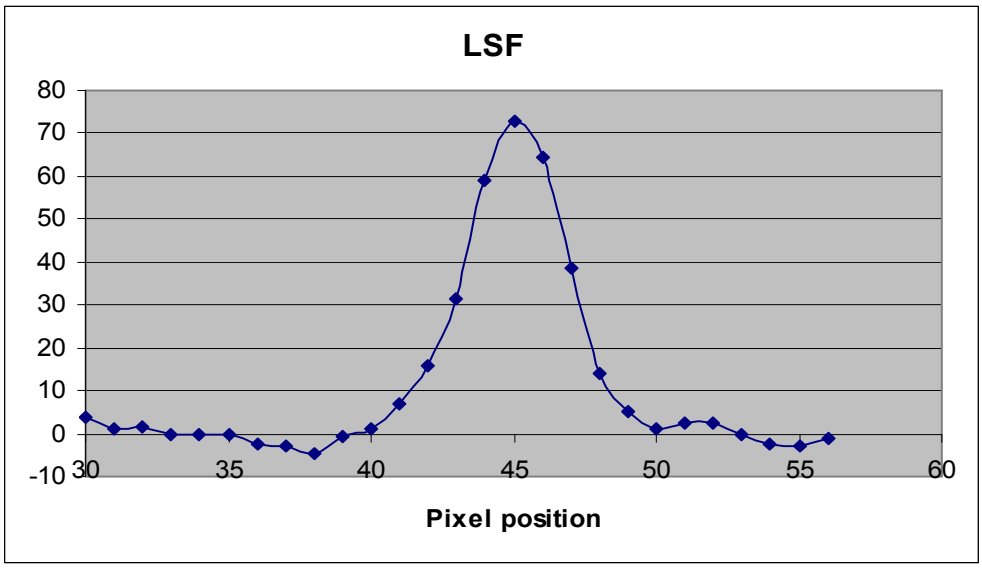



**Figure 4.5-2 A plot of the line spread function obtained from the ESF for the digital x-ray image.**

The MTF of the system is shown in Figure 3.5-3. The frequency scale on the *x*-axis is determined by the theoretical maximum resolution with increments according to the number of points used for obtaining the Fourier transform (Lätti, 2000). The theoretical maximum resolution was calculated to be 1.7 lp/mm.

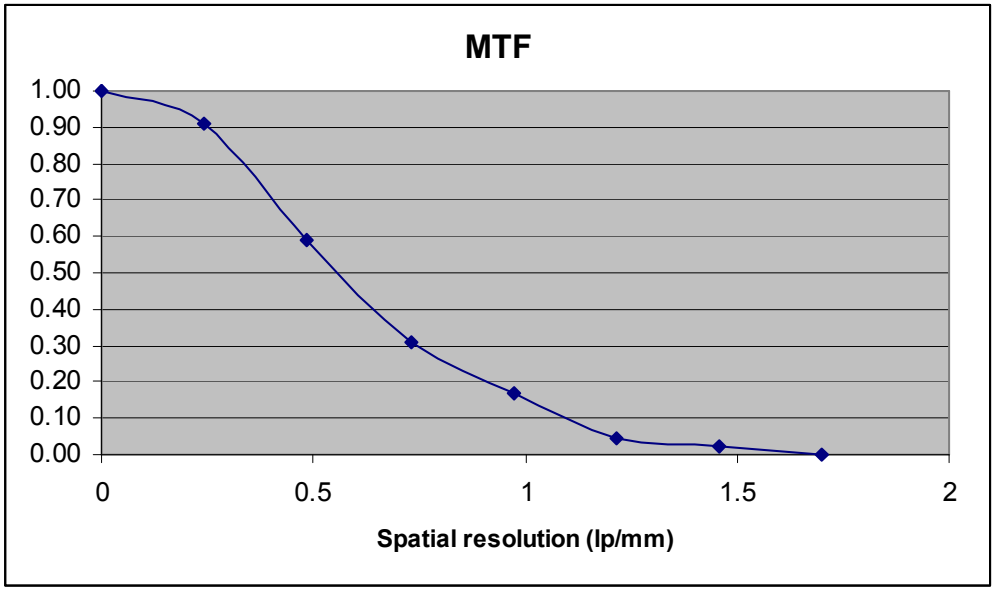



**Figure 4.5-3 The modulation transfer function of the digital imaging system.**

The maximum resolution was read off from the graph in Figure 4.5-3 at 2 % modulation transfer, which gave a value of about 1.51 lp/mm, this was comparable to the theoretical value. The MTF at 2 % approximates the limiting visual resolution, which is related to the eye's ability to distinguish the low contrast difference between the peaks and valleys in the presence of image noise.

The resolution of diagnostic film in comparison, was determined by the MTF which was calculated from the ESF. The maximum resolution for the diagnostic film was determined to be 10.0 lp/mm. Compared to film the digital system is of a lower resolution.

## *4.6 Correction for Lens Distortion*

The Matlab routine to correct the images for distortion that was written, gave unsatisfactory results as it increased the distortion further. The routine provided by Bouguet was therefore used to undistort the images. It can be seen from Figure 4.6-1 that the radial distortion was more dominant, with the tangential component being very small and thus it did not contribute significantly to the complete distortion model. The points at the corners of the image are displaced by as much as 5 pixels, which was the maximum displacement. For an image area of 30 cm × 30 cm, this corresponds to a displacement of 1.46 mm.

A visual representation of the effect of the distortion on the pixel image is also shown in Figure 4.6-1. The figure shows a complete distortion model incorporating both the tangential and radial components to fourth order. The arrows represent the effective

displacement of a pixel induced by the lens distortion with the number indicating the displacement in pixel units.

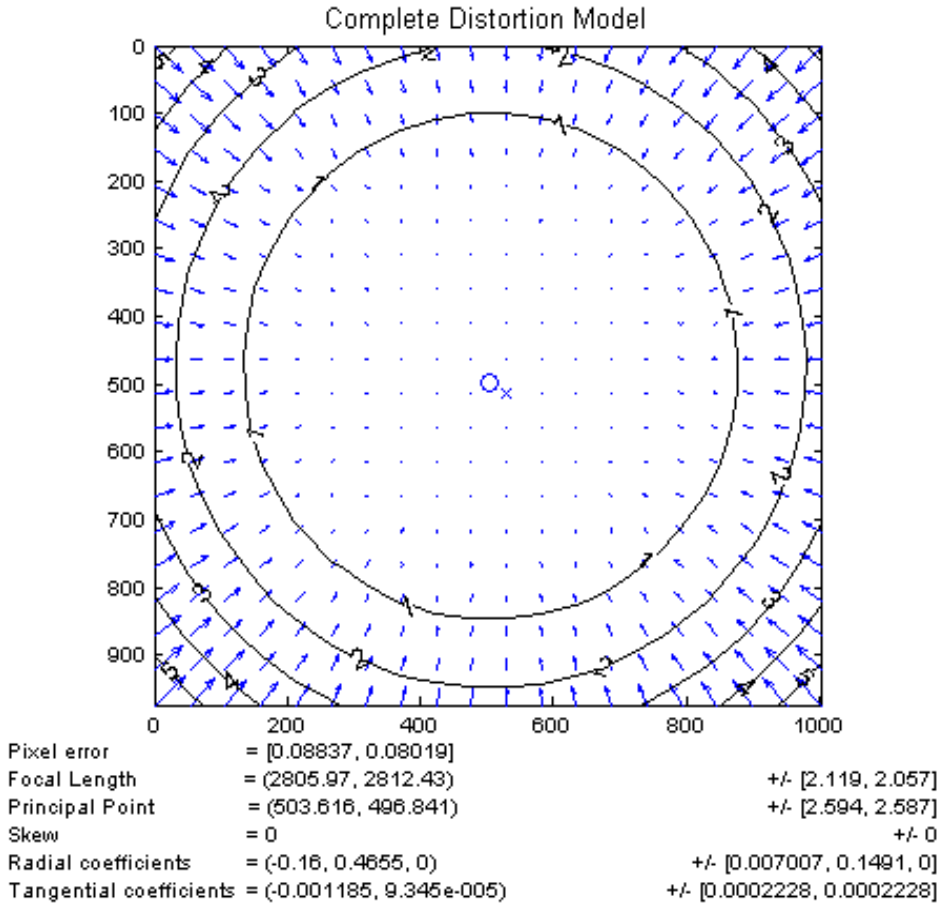
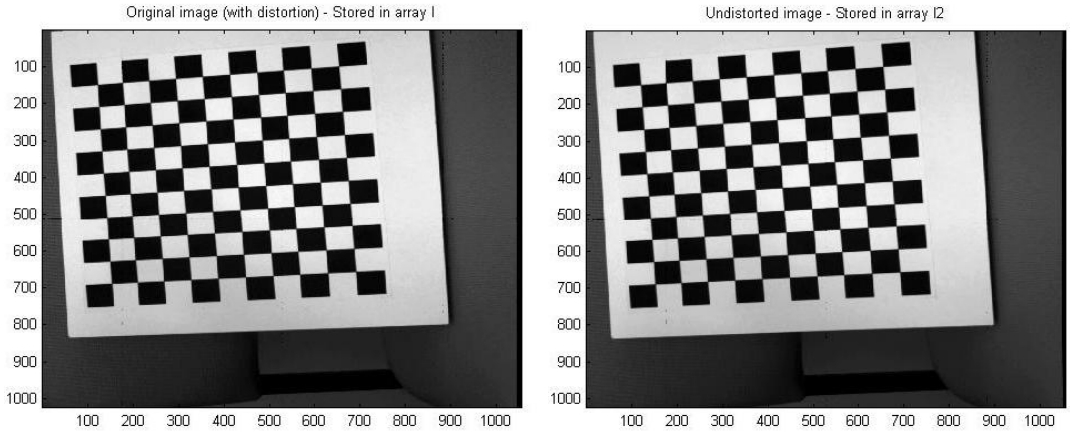
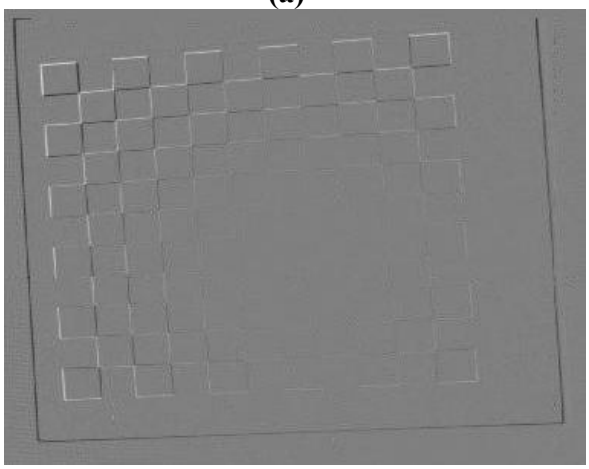



**Figure 4.6-1 A graphical representation of the distortion model incorporating the tangential and radial distortion.**

An image that was corrected using the distortion model is shown in Figure 4.6-2 together with the original image and the subtraction image.




**(a)** **(b)**



**(c)**

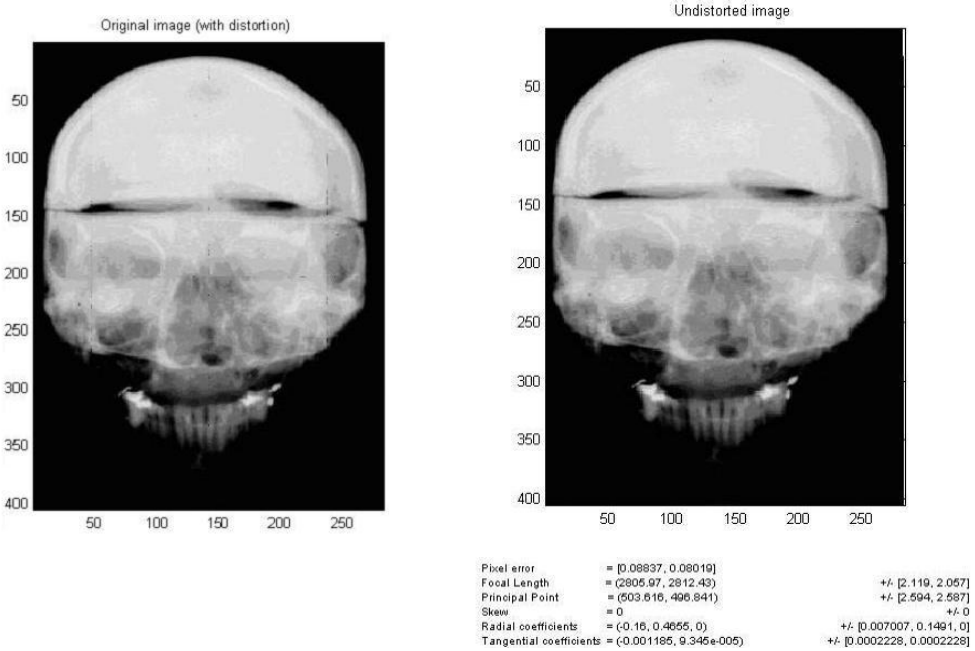
**Figure 4.6-2 An illustration showing the correction for lens distortion.**

*(a) Original checker board with lens distortion*

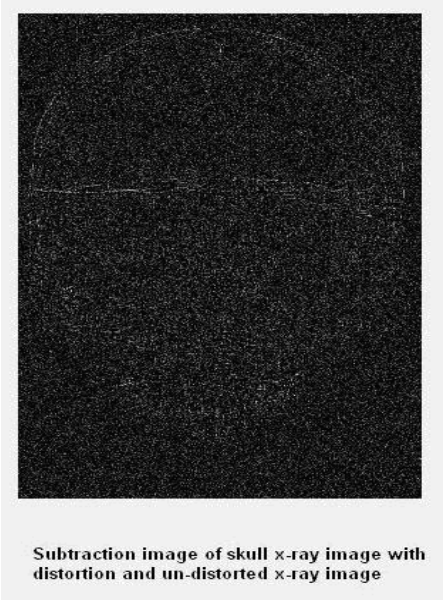
*(b) Checker board image that has been corrected for lens distortion,*

*(c)The subtraction image*

A skull image that was corrected using the distortion model is shown in Figure 4.6-3 together with the original image and the subtraction image.




**(a)** **(b)**




**(c)**

**Figure 4.6-3 An illustration showing the correction for lens distortion, for a skull x-ray image.**

*(a) The original x-ray image with the lens distortion*

*(b) X-ray image that has been corrected for lens distortion,*

*(c) The resultant subtraction image of image with distortion and one that has been corrected for lens distortion*

From the subtraction image it can be seen that there is little difference between the distorted image and the one that has been corrected for lens distortion. The histogram of the subtraction image is shown in Figure 4.6-4, where the minimum pixel value is shown to be zero and the maximum is 94.

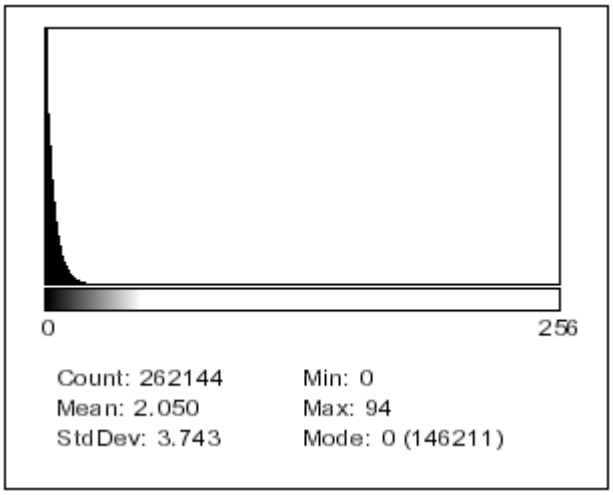



**Figure 4.6-4 The histogram for the subtraction of the distorted and un-distorted images shown in Figure 4.6-3.**

## *4.7 Zygo Experiment*

The tests from the MetroPro Zygo interferometer provided a surface profile of the samples as shown in Figure 4.7-1.

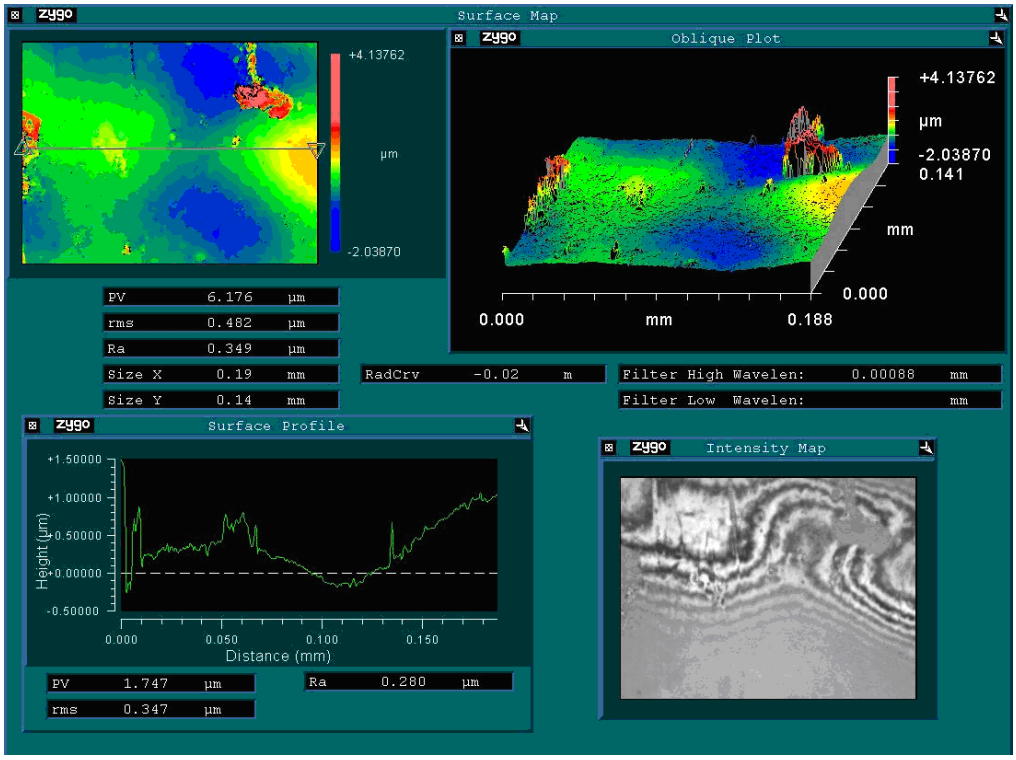



**Figure 4.7-1 The surface analysis using the MetroPro Zygo interferometer.** *Top left window shows a 2D map of the 3D topography of the surface as shown in the window on the right. The bottom left window shows the surface profile for a line across the surface, and the bottom right window shows the map of the diffraction patterns.*

The samples of the white paper and plastic used for the tests were about 1 cm × 2 cm. The *PV* gave an indication of the texture of the sample, whilst the *RMS* roughness and $R_a$ gave an indication of the optical properties of the sample, such as how the surface scatters light. *PV*, *RMS* and $R_a$ values give an indication of how the various surfaces reflect light. Surfaces that had similar reflectance would have similar *PV*, *RMS* and $R_a$ values. Gloss or specular reflectance (sometimes referred to as sheen or luster) are surface properties of a material, which are the refractive index and surface roughness (Bhushan, 1999). Zygo interferometry provides a method to quantify surfaces spatially.

**Table 4.7-1 Values of *PV*($\overline{\sigma_{PV}}$), *RMS*($\overline{\sigma_{rms}}$) and $R_a$ ($\overline{\sigma_{Ra}}$)for the samples in μm.**

| | $\overline{\sigma_{PV}}$ | $\overline{\sigma_{rms}}$ | $\overline{\sigma_{Ra}}$ |
|---|---|---|---|
| Sample 1 (Paper) | 19.54 | 2.19 | 1.72 |
| Sample 2 (Paper) | 5.87 | 0.37 | 0.27 |
| Sample 3 (Plastic) | 19.50 | 3.62 | 3.00 |
| Sample 4 (Plastic) | 16.54 | 2.41 | 1.97 |
| Sample 5 (Plastic) | 2.865 | 0.27 | 0.208 |
| Sample 6 (Paper) | 31.859 | 4.94 | 4.000 |
| Sample 7 (Plastic) | 11.232 | 1.50 | 1.208 |
| Scintillation Screen | 11.417 | 1.68 | 1.328 |

It can be seen from Table 4.7-1 that sample 7 had similar characteristics to the scintillation screen. The plastic sheeting from which sample 7 was taken, was used for the optical scattering experiments.

## *4.8 Optical Scatter Experiments*

It was assumed that because primary light from the scintillator was blocked completely, any measurable light from the strip would be due to reflected scattered light only. As the size of the strips decreased the measured scatter was expected to converge to a value, being the scattered light signal expected along the central axis if no strip was present. This value could however not be determined from the results that were obtained in (Figures 4.8-1 to 4.8-4) by taking a line profile along the center of the strip on the images.

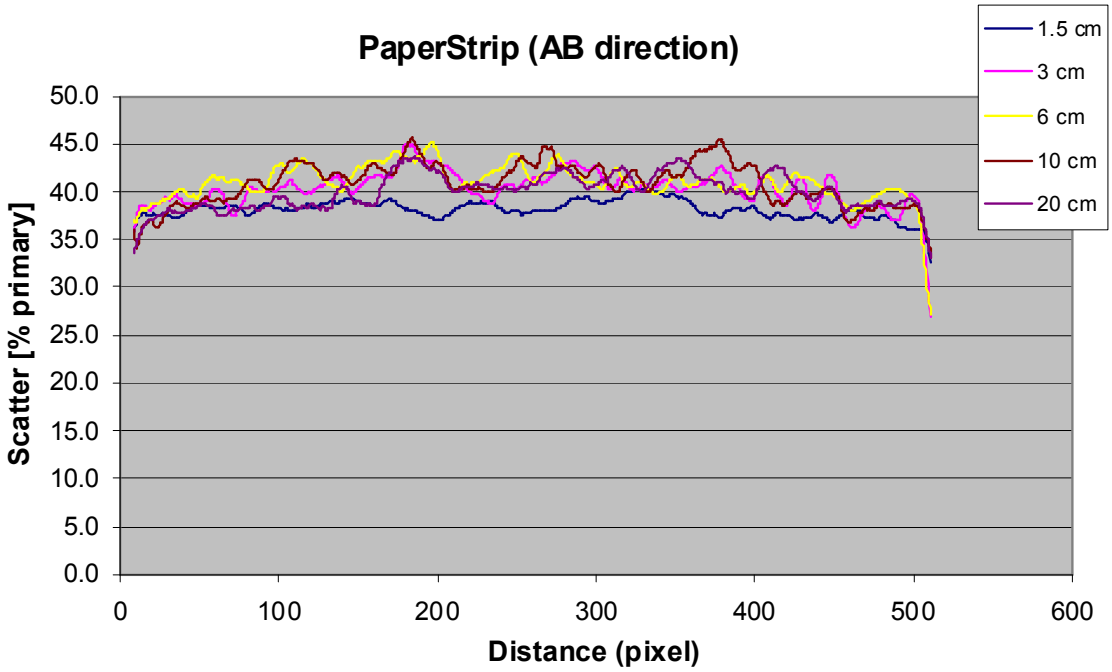



**Figure 4.8-1 The effect of paper strip width on measured optical scatter.** *The profiles were taken in the AB direction.*

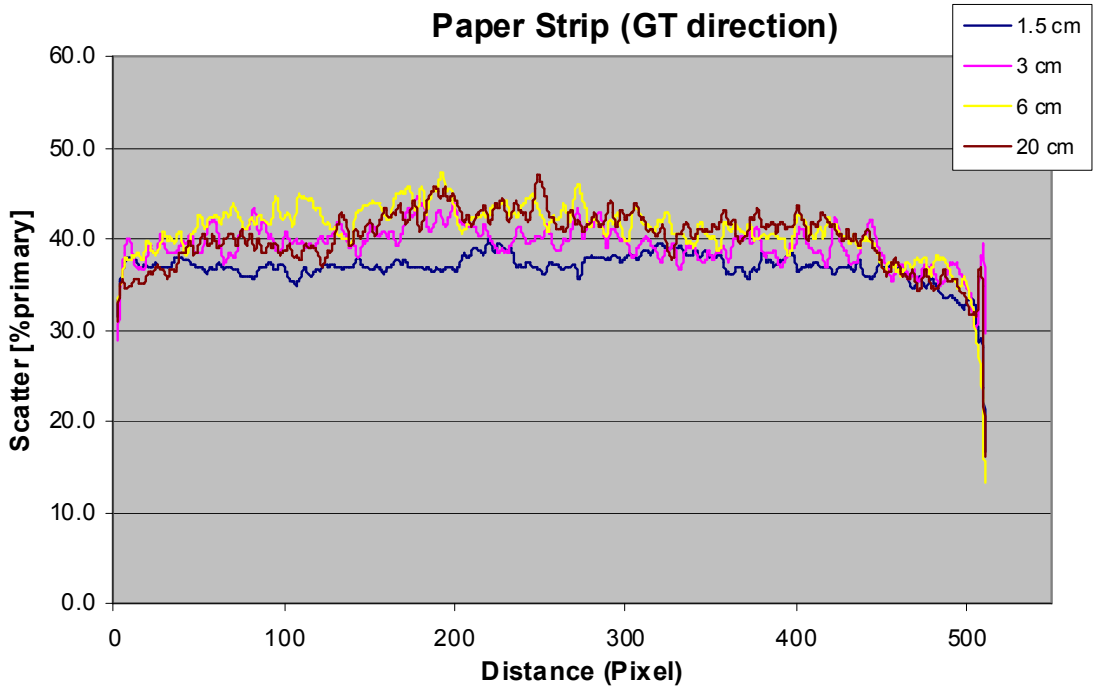



**Figure 4.8-2 The effect of paper strip width on measured optical scatter.** *The profiles were taken in the GT direction.*

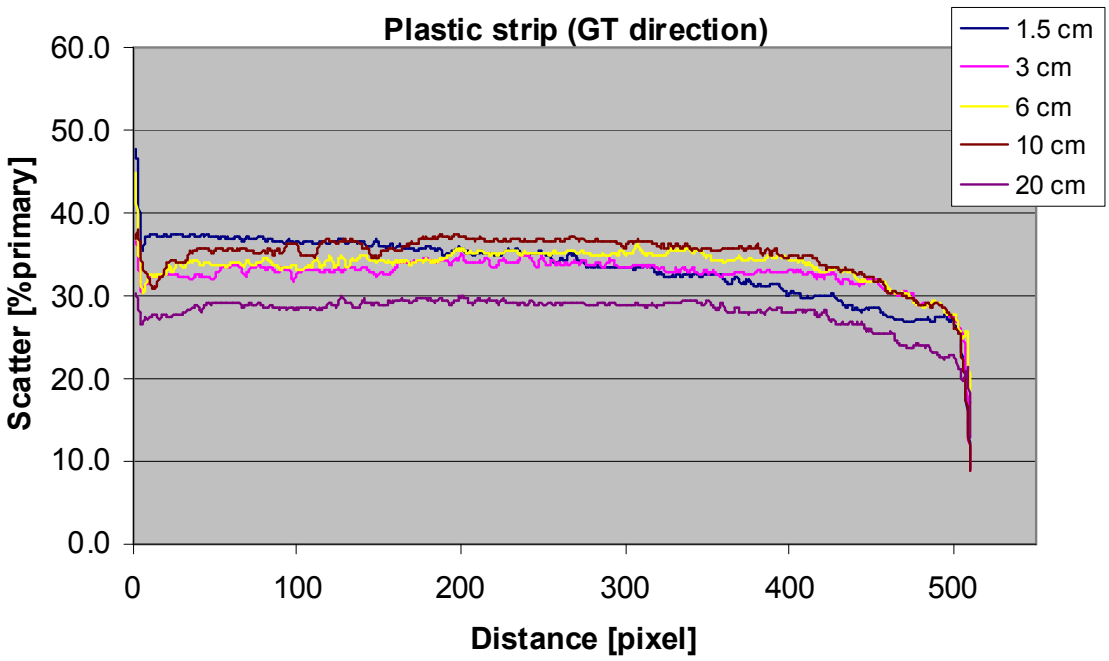



**Figure 4.8-3 The effect of plastic strip width on measured optical scatter.** *The profiles were taken in the GT direction.*

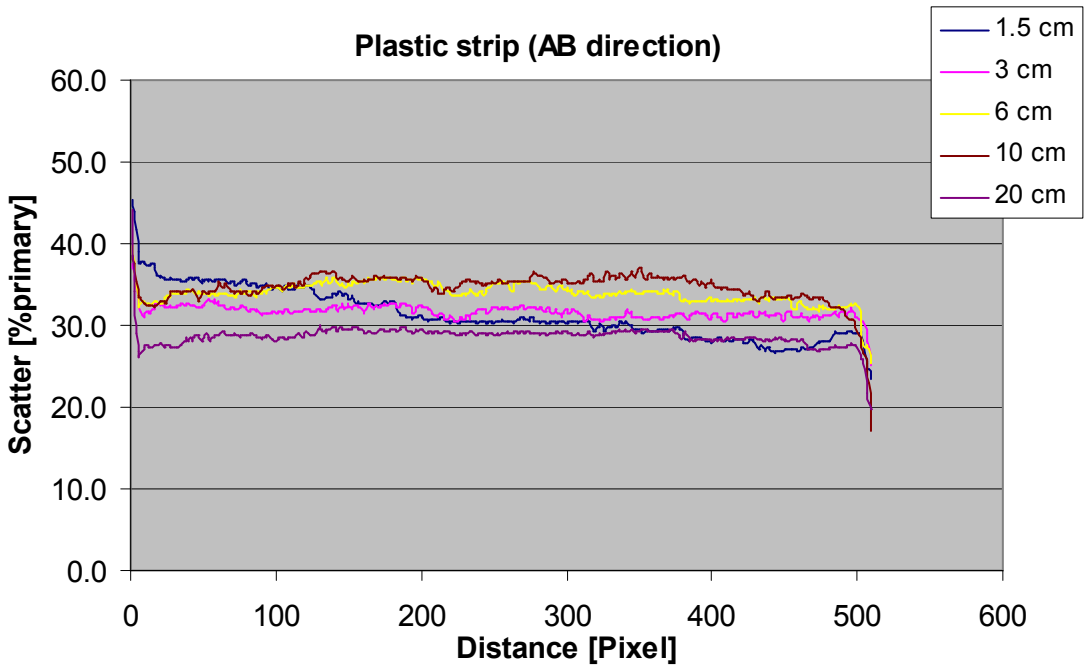



**Figure 4.8-4 The effect of plastic strip width on measured optical scatter. The** *profiles were taken in the AB direction.*

There was no convergence to a particular value as was expected. The graphs in Figure 4.8-1 to Figure 4.8-4 were expected to be comparable to those obtained by Partridge *et al.* (1999), as indicated in Figure 4.8-5. It was expected that as the width of the strips decreased the graphs for the line profiles would converge to a value close to that when no strips were presents. Since the strips that were used were of two completely different materials, i.e. that of paper and plastic, it can be seen that the scatter for the paper was about 40 % while that for the plastic was about 30 %. The scintillation screen was far from the mirror, which may have contributed to a reduction in the contribution of scatter (Lätti, 2000). This might also explain why the different mask sizes had little effect on the measured data.

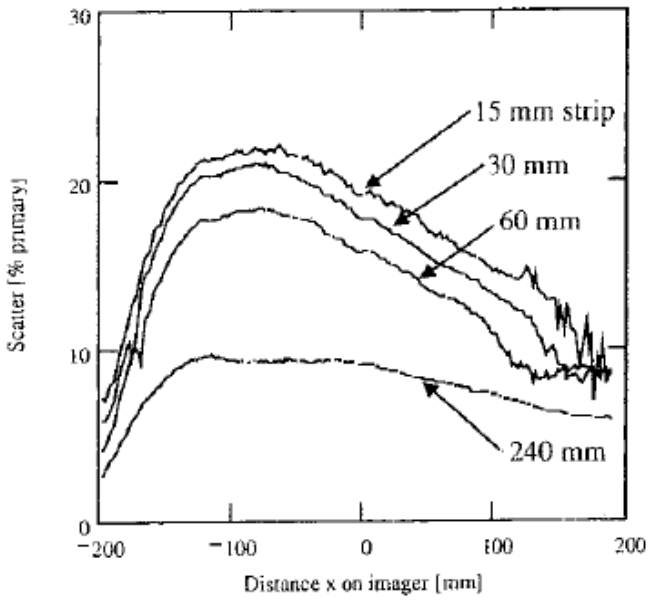



**Figure 4.8-5 The effect of measurement strip width on measured optical scatter.** The *measurements were taken with a 600 mm × 450 mm 6 MV beam using the high-speed imager. Signal converges on the 'ideal' value as strip width is reduced. Profiles are taken in the GT direction. [Image from Partridge et al., 1999]*

A plot of the scatter against the field mask, to determine optical scatter for different field sizes is show in Figure 4.8-6. It can be seen that there was a linear relation between the peak scatter and the mask size.

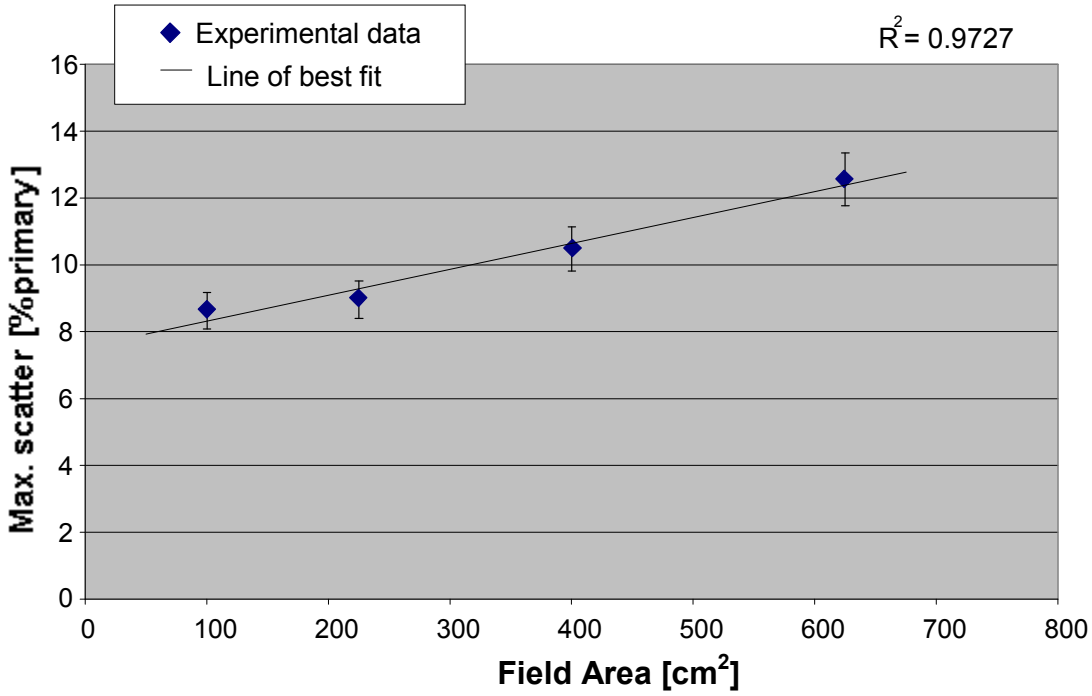



**Figure 4.8-6 The maximum scatter as a function of mask area.**

Figure 4.8-3 shows the measured results for the different mask sizes in the GT direction; these plots are similar to those that were obtained in the AB direction.

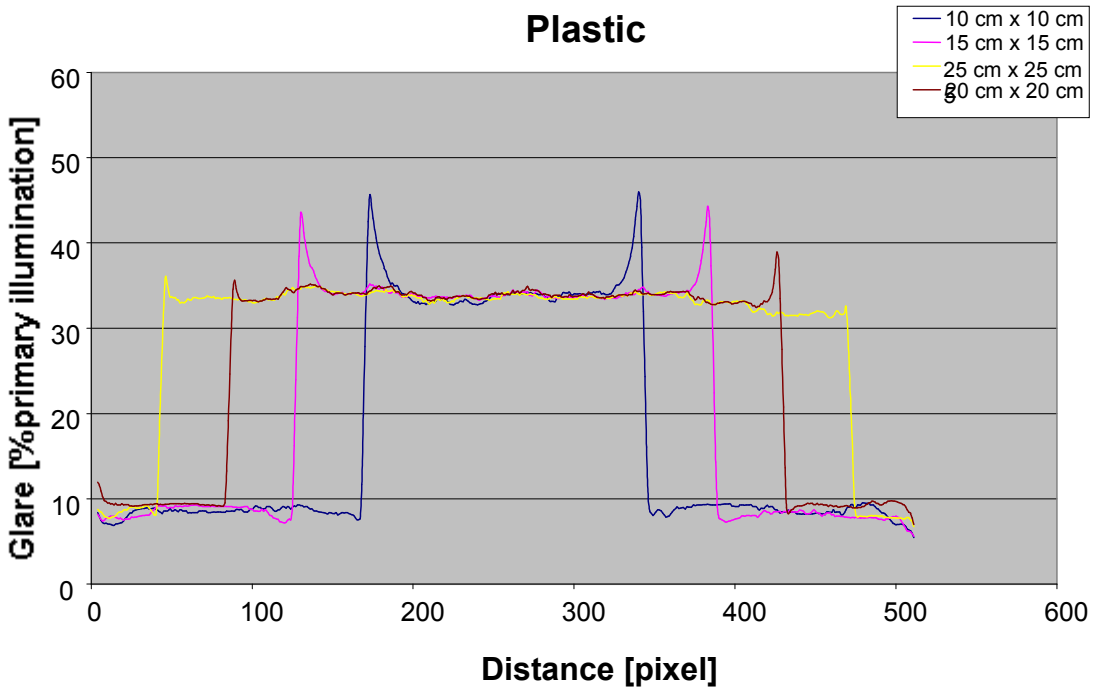



**Figure 4.8-7 The measured optical scatter on the central axis in the GT direction of imager for a range of mask sizes**

From Figure 4.8-7 the appearance of "horns" can be seen at the edges of the masks, and could have been due to jaggedness of the edges. The method to determine optical scatter described by Partridge *et al.* (1999) could not be verified. Different beam energies were used. The results obtained from the two dissimilar materials (that of paper sample and that of plastic sample) were similar even though the results from the Zygo experiment indicated that the materials were different. Further analysis of the optical scattering is required.

### 4.8.1 Anti-Scatter Grid

The effects of a filter to prevent glare were examined

It can be seen from Figure 4.8-8 that the glare was significantly reduced when the "privacy filter" was used.

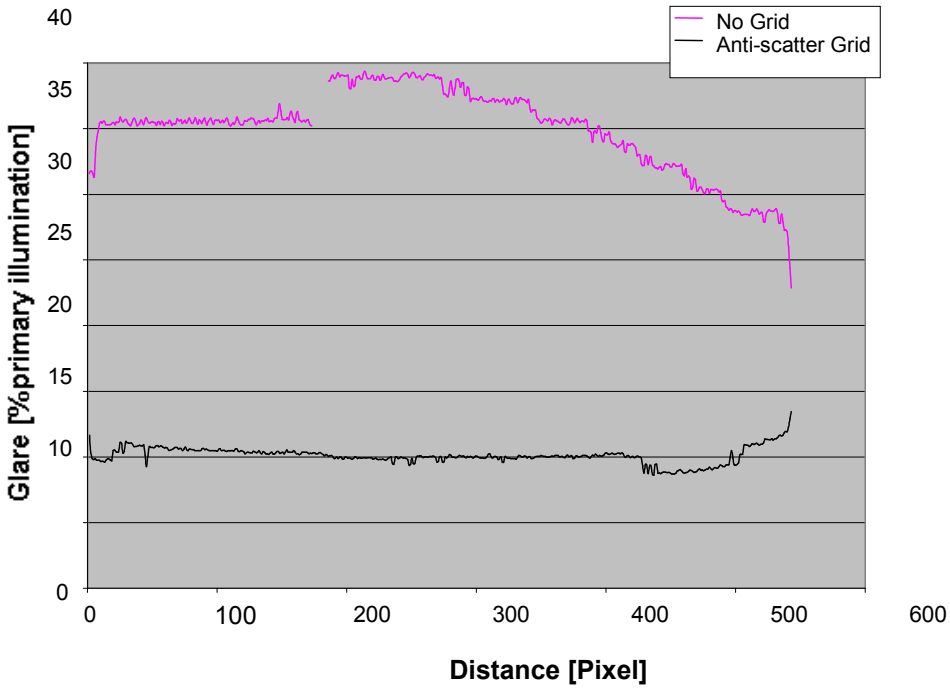
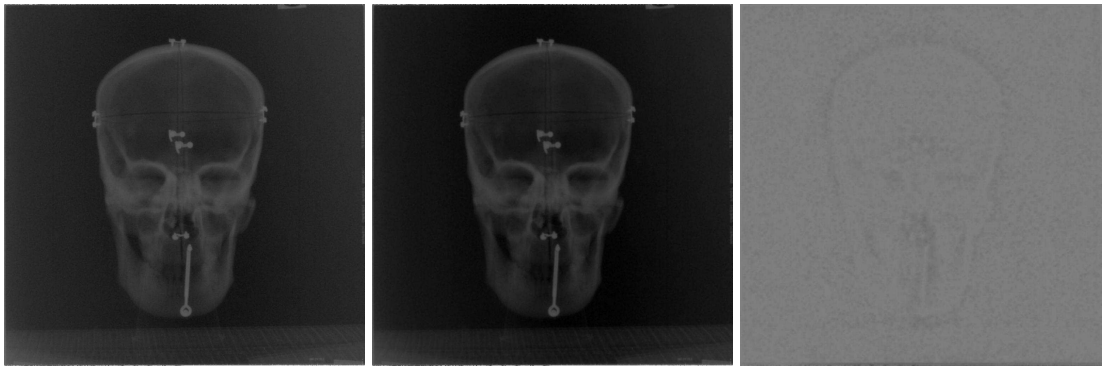



**Figure 4.8-8 The effect of adding an anti-scatter grid.**

A comparison between the filtered images of the skull phantom and those without the filter was made. The effect of the reduction in glare was determined by visually

comparing images taken with and without the filter as seen in Figure 4.8-9. The windowed subtraction image (difference image) is also shown.



**(a)** **(b)** **(c)**

**Figure 4.8-9 (a) An image of skull with the 'privacy filter' (b) An image of skull without the 'privacy filter' (c) Difference image**

The histogram for the subtraction image of the skull is shown in Figure 4.8-6. The figure shows discrete lines instead of a continuous distribution as expected. This could be due to how the software selects the histogram bin size, which was not established. Although Figure 4.8-8 showed a reduction in glare this was not evident in the subtraction image in Figure 4.8-9 (c).

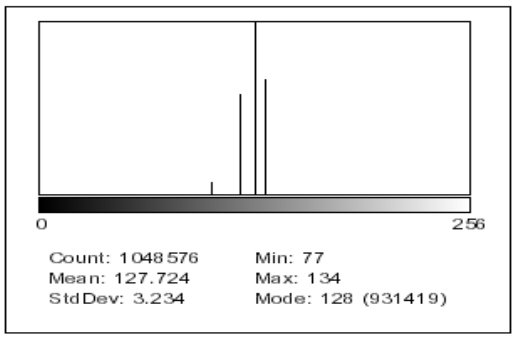
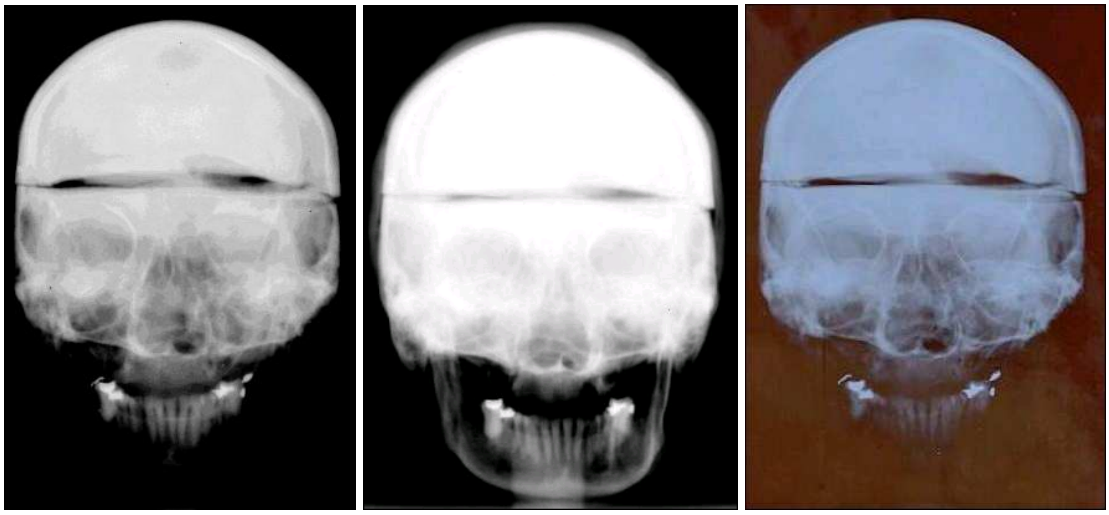



**Figure 4.8-10 A histogram of the subtraction image of the skull (taken with the use of the 'privacy filter' from image of skull without the 'privacy filter'**

## 4.9 X-ray Imaging and Pixel Binning

X-ray images of a human skull filled and covered with wax were obtained using the imaging device are shown in Figure 4.9-1. The digital images were obtained at two different exposure settings and also on x-ray film. Digital imaging allows for the setting of a different greyscale window to selectively determine what information is viewed.



**(a)** **(b)** **(c)**

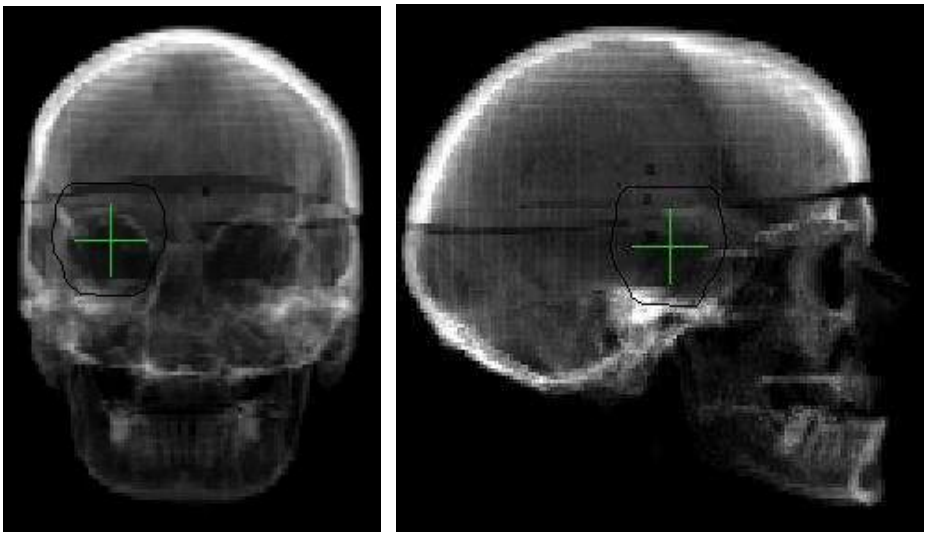
**Figure 4.9-1 An illustration of digital x-ray images compared to a film x-ray image**

***(a)*** ***A digital x-ray image of the skull.*** *Exposure settings: 85 kV, 200 mA, 160 ms Binning scheme of 2 (512× 512)*

***(b)*** ***A digital x-ray image of the skull.*** *Exposure settings: 77 kV, 250mA, 160 ms Binning scheme of 2 (512× 512)*

***(c)*** ***A film image of the skull.*** *Exposure settings: 77 kV, 250 mA, 63 ms. The image was digitized using a flatbed scanner*

When comparing the digital x-ray image in Figure 4.9-1 (a) with the DRR in Figure 4.9-2, it can be seen that the digital x-ray image quality is satisfactory for image registration.



*(a)* *(b)*

**Figure 4.9-2 An illustration of the digitally reconstructed radiograph of the skull from 5 mm slice thickness.** *(a) The posterior view of the skull (b) The right lateral view of the skull.*

### 4.9.1 Pixel Binning

Figure 4.9-3 shows the effects of pixel binning. It was noted that for the same kVp settings, less mAs was required to get the same image contrast, i.e. the mAs decreased by a factor of two for each increase in binning. When the images for different binning settings were compared for the same image size it was noted that images with a pixel binning of up to 3 × 3 could be used, despite the fact that increasing pixel size decreased the resolution.

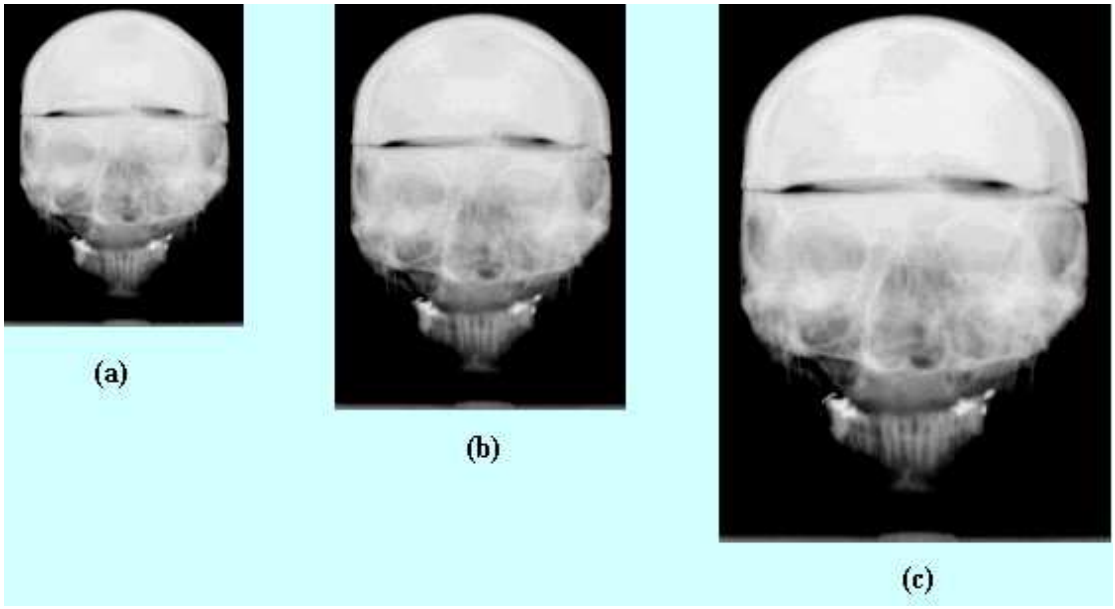



**Figure 4.9-3 An illustration showing the effects of pixel binning.** *The image size in pixels is indicated in brackets. (Images are for the same kV setting, with skull having wax)*

**(a) Skull Image 5 × 5 binning (204 × 204 ),** *Exposure setting of 85 kV, 8 mAs*

**(b) Skull Image 4 × 4 binning (256 × 256 )**, *Exposure setting of 85 kV, 10 mAs*

**(c) Skull Image 3 × 3 binning (341 × 341)**, *Exposure setting of 85 kV, 20 mAs*

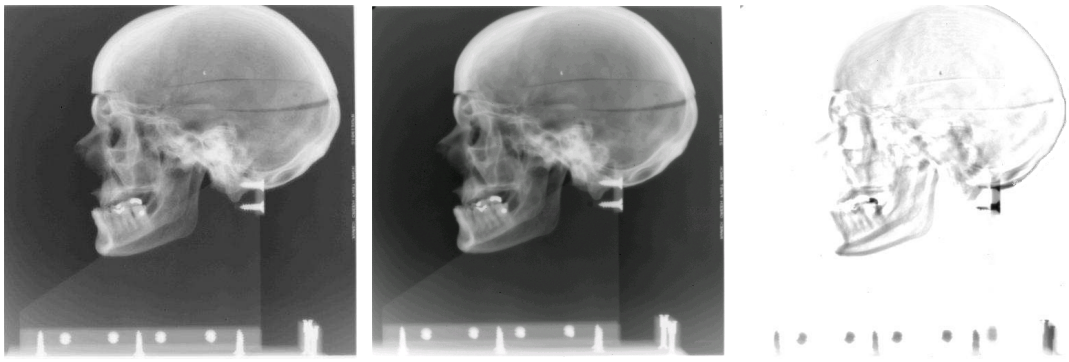
Table 4.9-1 indicates the exposure settings that were required to achieve images that were comparable to film. The use of higher kV values was required to reduce the mAs that was used for the digital x-ray images. Pixel binning of 2 × 2, giving an image size of 512 × 512 pixels gave a better image that a binning of 1 × 1 with an image size of 1024 × 1024 pixels. When using a binning of 1 × 1 it took about 38 s to download the image for viewing on the computer screen, whilst that of a binning of 2 × 2 took about 11 s.

**Table 4.9-1 Exposure settings for different binning schemes and film.**

| | kVp | mA | ms | mAs |
|---|---|---|---|---|
| Binning 1 × 1 | 100 | 160 | 500 | 80 |
| Binning 2 × 2 | 85 | 200 | 160 | 32 |
| Binning 3 × 3 | 77 | 250 | 80 | 20 |
| Film | 77 | 250 | 63 | 16 |

Varying the thicknesses of perspex slabs mimicking body tissue gave an indication of the effect of body tissue on the image quality. Figure 4.9-4 (b) shows an exposure of a skull with 6 cm of perspex in front of it. The same exposure settings were used in both images in Figure 4.9-4 (a) and (b), to demonstrate the effect of the Perspex on its own. There was a slight deterioration in the image with 6 cm of perspex in front of it, which suggests that even if the skull consisted of varying muscle and fat tissue, reasonably good x-ray images could still be obtained.

The subtraction image is also shown in Figure 4.9-4 (c). The image shows the difference between the two images, this difference is probably due to the change in the energy spectrum of the x-rays as a result of the filtration from the perspex.



**(a)** **(b)** **(c)**

**Figure 4.9-4 An illustration showing the effect of Perspex slab in front skull;**
**(a)** *A skull with no perspex in front Exposure setting: 95 kV, 200 mA, 100 ms.*
**(b)** *A skull with 6 cm perspex in front, Exposure setting: 95 kV, 200 mA, 100 ms, with binning of 2 × 2.*
**(c)** *An image resulting from subtracting image with no Perspex from that with 6 cm of Perspex.*

## *4.10 Shielding (MCNPX )*

The MCNPX simulations were of 20 million histories, and took a computer time of 5778.50 minutes. The Tally type 4 (F4) was used; it gave the flux averaged over a region of interest in units of particles/cm$^2$ (Pelowitz, 2005). Flux to dose conversion factors were used to convert the particle flux to dose equivalence rate, with the units for dose equivalence rate being μSv/h. These factors were obtained from ICRP (1996). The publication provides conversion coefficients for use in radiological protection against external radiation. A patient dose equivalence rate of $4.587 \times 10^{-4}$ μSv/h was determined. Of the 20 million histories only 12 protons were detected in the region of interest where the CCD chip would be located. Considering a beam current of 200 nA, the neutron dose equivalence rate was 1.096 μSv/h with a relative error of 2.88 % at one standard deviation. The equivalent dose rate for protons was

greater than the equivalent dose rate for neutrons; however the proton results had an error of greater than 50% and are therefore not reliable (Pelowitz, 2005). The photon dose equivalence rate was 1.644 μSv/h with a relative error of 0.20 % at one standard deviation. The results for the dose equivalence rate for electrons were unreliable as they had an error of 24 %. Although no specifications in a radiation environment are provided by the CCD manufacturer; a fluence of $2 \times 10^{11}$ neutrons/cm$^2$ creates a noticeable effect on a typical CCD (Rybka *et al.*, 2004). $8.021 \times 10^9$ neutrons/cm$^2$ would give a neutron dose equivalence rate of 1.096 μSv/h,, which is less by a factor of 25. The camera shielding is therefore adequate, and no extra shielding is required.

# CHAPTER 5 CONCLUSION

A camera-based imaging device that is comparably much cheaper than an amorphous silicon flat panel was developed and tested. To optimize the efficiency of the system, the CCD chip and scintillation screen were chosen so that the wavelength of the light from the screen closely matched the wavelength for which the CCD sensor has the greatest quantum efficiency. The use of the device allowed for x-ray images to be obtained in a shorter time, compared to developing film. With the camera system, the images are obtained in digital form, thus allowing for the use of image processing tools, such as contrast enhancement and image fusion.

The camera was operated at a temperature of –20 $^{o}$C to reduce the effects of dark current. The calibration frames were used to calibrate the images that were taken. Although the contribution of the lens distortion was small, the images were corrected for lens distortion by using the MatLab routine by Bouget (2004).

The results obtained by Partridge *et al*. (1999) could not be reproduced. The results might be improved if the strips and field masks were made from the same material as the scintillation screen; a substitute was used in the work because of the prohibitive costs of the scintillation screen. There was no apparent improvement in the image quality with the use of the privacy screen, as the benefit of the reduced scatter (which should improve the contrast resolution) is undone by the fact there is also an attenuation of the primary signal. Its use was not justified as it reduced the light coupling efficiency even further. Although no work was done on image registration (image fusion), as this was beyond the scope of this work, when comparing the digital

x-ray images (obtained from the imaging device) with the DDRs, it was seen that the digital images were satisfactory. The calculated resolution for film was about seven times better than the resolution of the device. However, the resolution of the digital images were satisfactory for the purposes of this work (the images would be used for comparison with DRRs). The field of view was chosen to include the whole area of the scintillation screen, however by reducing the field of view, the resolution could be increased. The measured parameters for the pixel binning of two was the preferred choice as this gave a better image than a binning of one. Some of the fine structures that were visible in images with binning of two, were not visible in those with binning of one, even after adjusting the window levels. The use of pixel binning allowed for the use of lower exposure settings when compared to exposure settings for un-binned images; this resulted in a reduction of patient dose. From the Monte Carlo simulations, no extra shielding was required for the camera.

Future work might include looking at the development of a phantom similar to the Las Vegas phantom for QA purposes. Investigations can also be carried out to look into the optical fibre coupling for the CCD as the chip does allow for such a coupling. The CCD is equipped with a fibre optic plate in front of the sensor area coupled via a fibre optical taper to the scintillation screen with fibre optic output window. This allows the light to be transmitted directly from the scintillation screen to the CCD chip. Fibre optics offers excellent resolution and reduces contrast loss due to stray light (Karellas *et al.*, 1992). However, the costs involved in purchasing the optical fibre coupling would have to be considered. Optical fibre coupling has the potential for using a lower exposure setting which leads to a further reduction in the dose to the patient, and improvement in image quality.

# REFERENCES


Ahmed, S. N., (2007), *Physics and Engineering of Radiation Detection*, Academic Press.

Althof, V.G.M. *et al.* (1996), Physical characteristics of a commercial electronic portal imaging device, *Medical Physics*, vol. 23, no. 11, pp. 1845-54.

Apogee Instruments Inc., CCD Camera Operating instructions

Beckmann, P. and Spizzichino, A. (1963), *The Scattering of Electromagnetic Waves from Rough Surfaces*, Pergamon, New York.

Beutel, J. et al. (2000), *Handbook of Medical Imaging: Medical Image Processing and Analysis*, SPIE Press.

Bhushan, B. (1999), *Principles and applications of tribology*, Wiley-IEEE

Born, M. and Wolf, E. (1999), *Principles of Optics: Electromagnetic Theory of Propagation, Interference and Diffraction of Light*, Cambridge University Press.

Bouguet, J. (2004), Camera Calibration Toolbox for Matlab, www.vision.caltech.edu/bouguetj/calib_doc *(from the internet)*

Bovik, A. (2000), *Handbook of Image and Video Processing*, Academic Press.

Boyer, A.L. *et al.* (1992), A review of electronic portal imaging devices (EPIDs), *Medical Physics*, vol. 19, no. 1, pp. 1-16.

Brodie, I. and Gutcheck, R.A. (1985), Minimum entrance exposure estimates for information recording in diagnostic radiology, *Medical Physics*, vol. 12, no 3, pp. 362-367.

Bronzino, J.D. (2000), The *Biomedical Engineering Handbook*, Vol. I, Springer.

Brown, D.C. (1966), Decentering Distortion of Lenses, *Photometric Engineering*, Vol. 32, No. 3, pp. 444-462.

Bushberg, J.T.*et al*. (2002), *The Essential Physics of Medical Imaging,* Lippincott Williams & Wilkins.

Carlsson, G.A. and Chan, H.P. (1999), Commentary: Progress in optimization of patient dose and image quality in x-ray diagnostics, *Physics in Medicine and Biology*, vol. 44 no. 2.

Collins, A.R. (2005), Depth of field, www.digifotoinfo.com *(from the internet)*

Dick, C.E. and Motz, J.W. (1981), Image information transfer properties of x-ray fluorescent screens. *Medical Physics,* vol. 8, no. 3 pp. 337-346.

Diffraction Limited, *MaxIm DL User Guide*, Image Processing Software.

Dimitrijev, S. (2000), *Understanding Semiconductor Devices*, Oxford University Press US.

Dohi, T. and Kikinis, R. (2002), *Medical Image Computing and Computer-assisted Intervention*-MICCAI 2002, Springer

E2V Technologies Limited, A1A-CCD47-10 Backthinned Issue 3, October 2002

Edmund Optics (2000), *Best of EO application notes*, Technical documentation.

Enertron Inc. (2000), *Thermoelectric cooling- The basics*, Enertron Library.

Freund, L.B. and Suresh, S. (2003), *Thin Film Materials: Stress, Defect Formation, and Surface Evolution*, Cambridge University Press.

Fujita, H. *et al*. (1985), Investigation of basic imaging properties in digital radiography. 6. MTFs of II-TV digital imaging systems, *Medical Physics*, vol.12, no.6, pp. 713-720.

Fujita, H. *et al*. (1989), Basic imaging of a computed radiographic system with photostimulated phosphors, *Medical Physics*, vol.16, no.1, pp. 52-59.

Giakoumakis, G. E. and Miliotis, D.M (1985), Light angular distribution of fluorescent screens excited by x-rays, *Physics in Medicine and Biology*, vol. 30, no. 1, pp. 21-29.

Giger, M. L. and Doi, K. (1984), Investigation of basic imaging properties in digital radiography. I. Modulation transfer function, *Medical Physics*, vol. 11, no. 3, pp. 287-295.

Goitein, M. (1985), Calculation of the uncertainty in the dose delivered during radiation therapy, *Medical Physics*, vol. 12, no. 5, pp. 608-612.

Gonzalez, R.C. and Woods, R.E. (2002), *Digital Image Processing*, 2nd Edition, Prentice-Hall.

Guerra A.D. (2004), *Ionizing Radiation Detectors for Medical Imaging*. World Scientific

Gupta, D. C. and Langer, P. H. (1987), *Emerging Semiconductor Technology*: A Symposium ASTM Committee F-1 on Electronics, ASTM International.

Hanson, K. M. (1981), Noise and contrast discrimination in CT, *Radiology of the Skull and Brain, Vol. V: Technical Aspects of Computed Tomography*, T. H. Newton and D. G. Potts, eds., pp. 3941-3955, C. V. Mosby, New York.

Hanson, K. M. (1998), A simplified method of estimating noise power spectra, *Physics of Medical Imaging, Proc. SPIE 3336*, J. T. Dobbins III and J. M. Boone eds., pp. 243-250

Harbas, P. (1993), *Dissertation: Analysis of Physical Effects in Small Silicon MOS Devices*, Technischen Universität Wien.

Hartley, R. and Zisserman (2000), A., Multiple View Geometry in Computer Vision, Cambridge University Press.

Harwood, E. (2007), *Digital CCTV: A Security Professional's Guide*, Butterworth-Heinemann.

Hecht, E.(2001), *Optics*, Pearson Addison Wesley.

Hendricks, J.S. *et al.* (2005), MCNPX manual, version 2.5.f, Los Alamos National Laboratory.

Herman, M.G. *et al.* (2000), Guide to clinical use of electronic portal imaging, *Journal of Applied Clinical Medical Physics,* vol. 1, no. 2, pp. 38-57.

Herman, M.G. *et al.* (2001), Clinical use of electronic portal imaging: Report of AAPM Radiation Therapy Committee Task Group 58, *Medical Physics*., vol. 28, no. 5, pp. 712-737.

Hummel, R.E. *et al.* (1995) *Handbook of optical properties: Thin Films for Optical Coating*, Vol 1, CRC Press.

International Commission on Radiological Protection (ICRP) Committee 3, Diagnostic reference levels in medical imaging: Review and additional advice. www.icrp.org/docs/DRL_for_web.pdf *(from the internet)*

International Commission on Radiological Protection (ICRP) Publication 74 (1996): Conversion Coefficients for use in Radiological Protection against External Radiation, Annals of the ICRP Volume 26/3

International Commission on Radiation Units and Measurements (ICRU) Report #19. (1971), Radiation quantities and units.

Jedlička, J. and Potůčková, M. (2007), Correction of radial distortion in digital images, Charles University in Prague.

Johns, H. E. and Cunningham, J. R. (1983), The physics of radiology fourth edition, Charles C Thomas Publisher.

Karellas, A. *et al.* (1992), Charge-coupled device detector: Performance considerations and potential for small-field mammographic imaging applications, *Medical Physics* vol. 19, no. 4, pp. 1025-1023.

Lätti, E. (2000), Development of a digital X-ray-imaging system at the National Accelerator Centre, MSc thesis at the University of Stellenbosch.

Leal, M.J. (2001), Effect of pixel size and scintillator on image quality of a ccd-based digital x-ray imaging system, MSc thesis at the Worcester Polytechnic Institute.

Li, F. M. and Nathan, A. (2005), *CCD Image Sensors in Deep-ultraviolet: Degradation Behaviour and Damage Mechanisms*, Springer

Liu, H. *et al*. (1994), Methods to calculate the lens efficiency in optically coupled CCD x-ray imaging systems. *Medical Physics,* vol. 21, no. 7, pp. 1193-1195.

Liu, H. *et al*. (2000), Lens distortion in optically coupled digital x-ray imaging, *Medical Physics*, vol. 27, no. 5, pp 906-912.

Lomax, A.J. *et al.* (2001), Intensity modulated proton therapy: A clinical example, *Medical Physics,* vol. 28 no. 3, pp 317-324.

Mikhail M.E. *et al* (2001), *Introduction to Modern Photogrammetry*, Wiley

Motz, J.W. and Danos, M. (1978), Image information content and patient exposure, *Medical Physics*, vol. 5, no. 1, pp. 8-22.

Munro, P., *et al*. (1990), Therapy imaging: A signal-to-noise analysis of a fluoroscopic imaging system for radiotherapy localisation. *Medical Physics,* vol. 17, no. 5, pp. 763- 772,

National Council on Radiation Protection and Measurements (NCRP), 1993, Limitation of Exposure to Ionizing Radiation, Report No. 116.

Nikon Corporation, Nikkor 35 mm f/1.4 lens *Instruction Manual*.

Nocedal, J. and Wright, S.J., (1999), *Numerical Optimization*, Springer

Oakley, J. (2003), *Digital Imaging, A Primer for Radiographers, Radiologists and Health Care Professionals.* Cambridge University Press

Partridge, M. *et al*. (1999), Optical scattering in camera-based electronic portal imaging, *Physics in Medicine and Biology*, vol. 44, pp. 2381-2396.

Pelowitz, D.B. (2005), MCNPX User's Manual, version 2.5.0., Los Alamos National Laboratory.

Pollock, D.D. (1985), *Thermoelectricity: Theory, Thermometry, Tool By*, ASTM International

Rangayyan, R.M. (2005), *Biomedical Image Analysis*, CRC Press.

Renema, K. (1999), Digital x-ray imaging with a CCD camera and a scintillator screen, Practical training report for MSc degree at the Rijksuniversiteit Groningen.

Rieke, G. (2002), *Detection of Light: From the Ultraviolet to the Submillimeter*, Cambridge University Press

Rybka, D.K. et al. (2004), *Irradiation Investigations for TESLA and X-FEL experiments at DESY*, TESLA Report 2004-12.

Ryneveld, S.C. (1998), Measurement of proton beam dose profiles using a sensitive scintillation screen observed with a CCD camera, MSc thesis at The University of British Columbia.

Seibert, J.A. *et al*. (1984), Characterization of the veiling glare PSF in x-ray image intensified fluoroscopy, *Medical Physics*, vol.11, no.2, pp.172-179.

Seibert, J.A. *et al*. (1985), Removal of image intensifier veiling glare by mathematical deconvolution techniques, *Medical Physics*, vol.12, no.3, pp. 281-288.

SITe, Scientific Imaging Technologies, Inc. (2003), *An introduction to scientific imaging charge-coupled devices*.

Smith, G. and Atchison, D.A. (1997), The eye and visual optical instruments, Cambridge University Press.

Stroebel, L.D. and Zakia, R.D. (1993), *The Focal Encyclopedia of Photography*, Focal Press.

Sun, Y. *et la.* (2007), *Post-Si CMOS: III-V n-MOSFETs with High-k Gate Dielectrics*, CS MANTECH Conference, May 14-17, 2007, Austin, Texas, USA

Tapiovaara, M.J. *et al.* (1999), A search for improved technique factors in paediatric fluoroscopy, *Physics in Medicine and Biology*, vol. 44, pp. 537-559.

Taylor, N. T., (1993), An Analysis of FM Jamming and Noise Quality Measures, Air Force Institute of Technology, Air University.

Tilley, R.J.D. (2004), *Understanding solids: the science of materials*, John Wiley and Sons

Triggs B. *et al.* (2000), Vision Algorithms: Theory and Practice, Spinger.

Wagner, R. F (1976), Fast Fourier digital quantum mottle analysis with application to rare earth intensifying screen systems, *Medical Physics*, vol. 4 pp. 157-162

Webb S. (1993), *The Physics of Three-Dimensional Radiation Therapy: Conformal Radiotherapy, Radiosurgery, and Treatment Planning*, CRC Press.

Webb S. (1997), *The Physics of Three Dimensional Radiation Therapy: Advances in Technology*, CRC Press.

Whitaker J. C. (1996), *The Electronics Handbook*, CRC Press.

Yu, T. and Boone, J. M. (1997), Lens coupling efficiency: Derivation and application under differing geometrical assumptions, *Medical Physics*, vol. 24, no. 4, pp. 565-570.

Zhuang, H. and Roth, Z.S. (1996), *Camera-aided Robot Calibration*, CRC Press.

# APPENDIX A.

## TEST DATA SHEET

### *TEST DATA SHEET*

| | | | | | |
|---|---|---|---|---|---|
| **Model:** | AP47P | **Date:** | 11/20/2002 | **Sensor:** | CCD47-10-1 |
| **Bits:** | 16 | **Firmware Rev.:** | P47C | **Size** | 1024X1024X13u |
| **CAM s/n:** | A2804 | **Cable Length:** | 25' | **Cooling:** | HV |
| **PC s/n:** | | **Base Address:** | 3bc | **Window:** | Std |

**TEST DATA**

**System Noise**

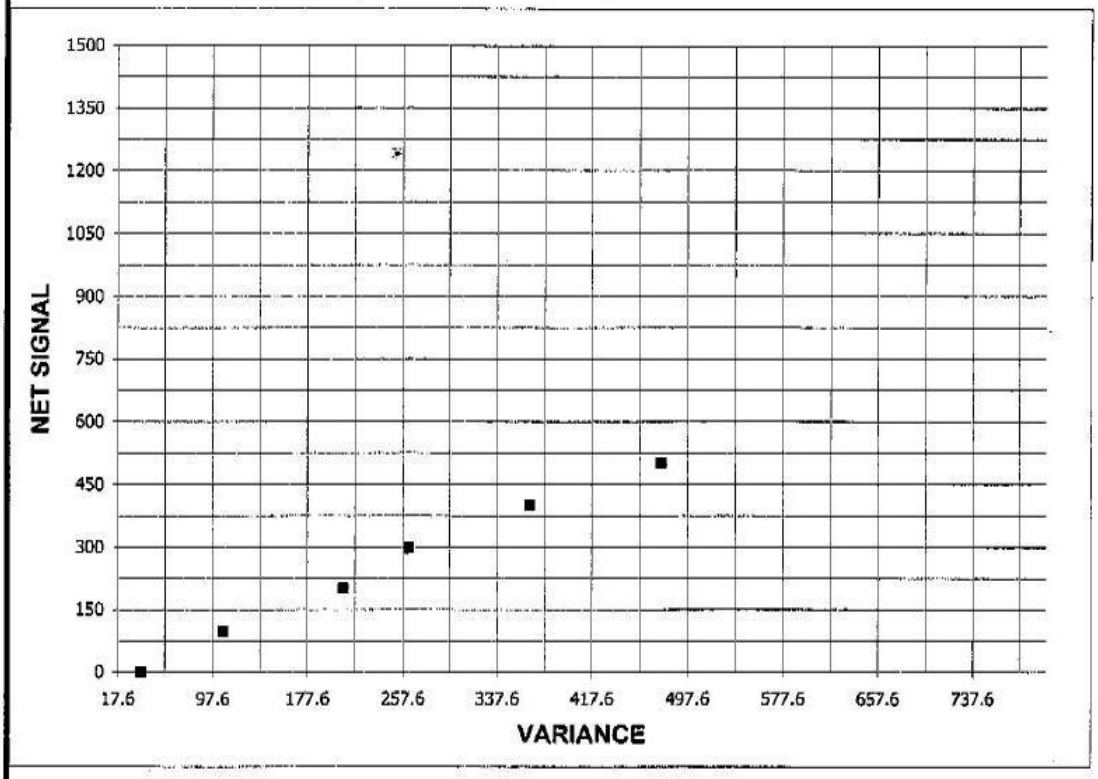
| | |
|---|---|
| **GAIN:** | 1.3 |
| **SDEV** | 5.1 |
| **n(e-)** | 6.4 |

**Bias Level Setting:** 2310

**Power On Cooling** n/a

**Maximum Digitized Well Capacity:** 80k

| | | | Zero | Scale |
|---|---|---|---|---|
| **GAIN** | 1.3 | e-/ADU | **Temp Calibration:** 165 | 2.1 |




**DARK COUNT**

| | |
|---|---|
| **Temperature** | -27 |
| **Net Count** | .56e/p/s |

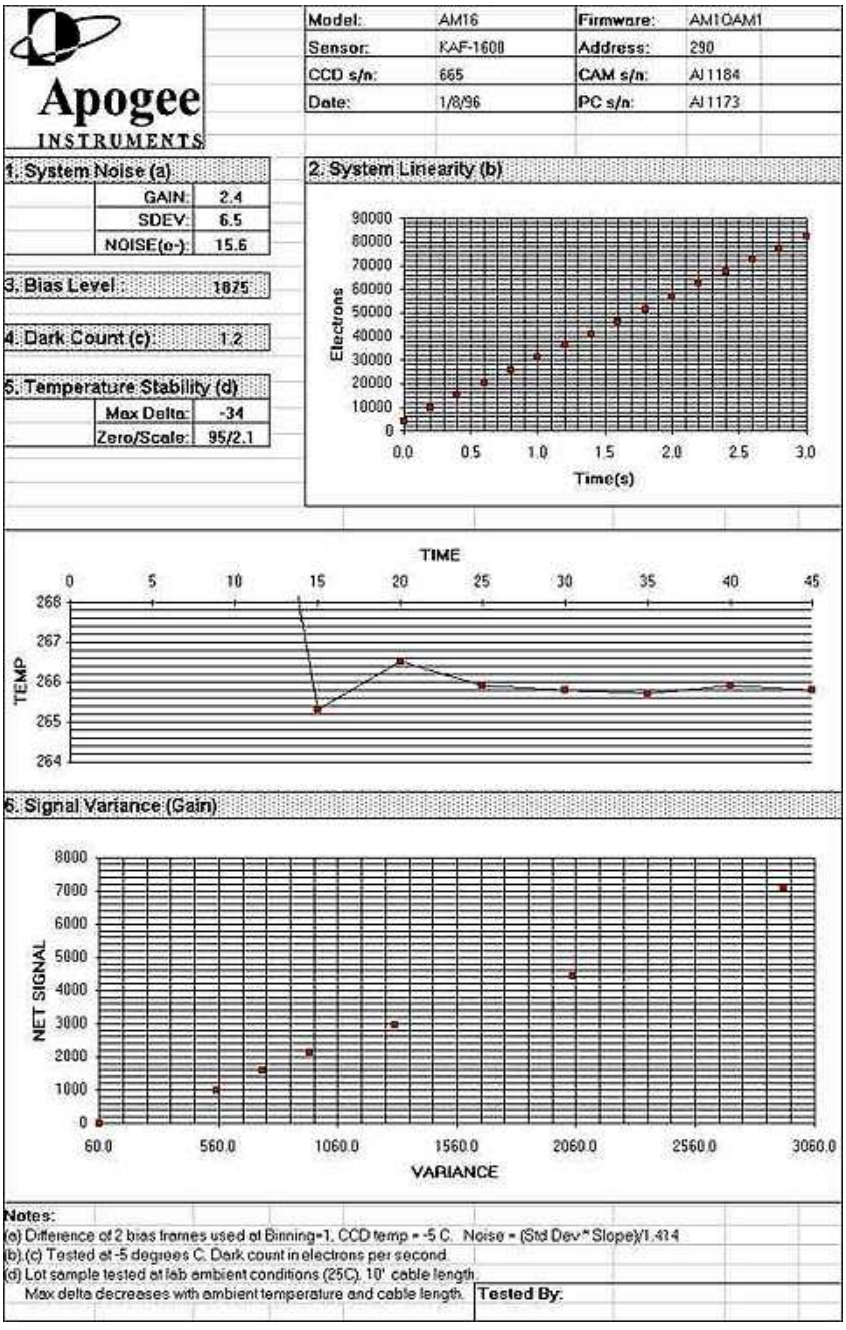
**Notes:** 01063/09/19
PR

# APPENDIX B.

## CAMERA TEST METHODS

The following document is from the Apogee Instruments Inc. website (http://www.ccd.com/ccd105.html)

The following data sheet is typical of that prepared by Apogee Instruments for each of its imaging cameras. Some of the measurements here are done by design, and some are performed on each camera in production. In this course, each test will be described and, where appropriate, tips will be given for performing these tests yourself. It is recommended that you familiarize yourself with the other subjects in CCD University before reviewing the subject of testing. These tests are important indicators of camera quality and they fulfill the commitment we have to our customers for substantiating the claims we make before the purchase.

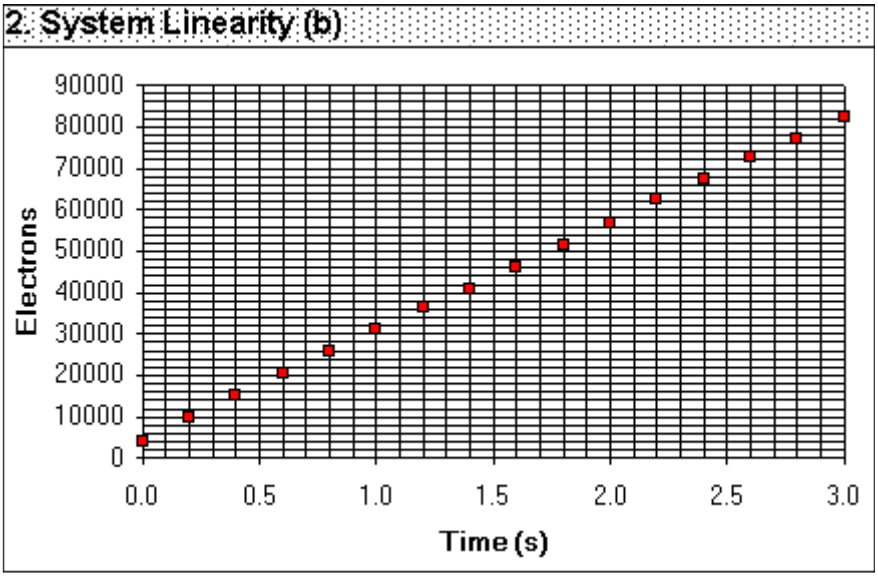


**Gain**

| 1. System Noise (a) | | |
|---|---|---|
| | GAIN: | 2.4 |
| | SDEV: | 6.5 |
| | NOISE(e-): | 15.6 |

The first section of data lists the gain of the system in electrons per count, also referred to as electrons/ADU. For a gain of 2.4, 10,000 counts of signal would equate to 24,000 photons of light. The gain figure is determined in section 6, and it will be discussed there. The standard deviation was obtained from the difference of two bias frames taken at -5 degrees C, calculated by software from a region of interest (ROI) near the center of the frame. The product of the gain and standard deviation is noise in electrons. A word of caution: Shutters can leak light. The camera should be well sealed and in a very dark room when this is done.

**Linearity**




Linearity is a measure of how consistently the CCD responds to light over its well depth. For example, if a 1-second exposure to a stable light source produces 1000 electrons of charge, 10 seconds should produce 10,000 electrons of charge. The deviation from this straight line is a measure of non-linearity. Dark count build-up over time has also been used by some, but we do not endorse this as a valid way to determine linearity. You can perform this test yourself to a reasonable degree.

Try this procedure:

1. Place the camera upright in a room with no windows and a stable light source. A fluorescent light will work. Position the light so that it casts indirect light on the ceiling above the camera.

2. Cut out a piece of plain white paper and place it over the camera opening.

3. Take exposures with the camera in even increments from zero until the camera saturates. Plot the counts on the Y axis and the time on the X axis. The counts can be converted to electrons by multiplying by the gain of the system. The line should be reasonably straight throughout the well depth of the sensor.

4. A word of warning. If you are using a camera with a fast shutter that can go to 0.02 seconds, increments down to 0.1 seconds should produce results virtually free from shutter uncertainty. If you are using the ultra slow shutters only capable of 0.1 second exposures, then the increments of time should be larger (0.5 seconds). Try and keep the entire test very short (less than 5 seconds) and keep the camera as cold as possible to minimize dark count induced error. For Kodak KAF-0400 sensors at -5° C and 0.1-second increments for a total of 3.0 seconds to saturation, dark count is not a signficant factor. Under these conditions, very good linearity results can be obtained.

**Bias Level**

| 3. Bias Level : | 1875 |
|---|---|

The bias level is shown on the Apogee Instruments data sheets for information only. It is the mean bias level taken from the statistics box on a raw bias frame discussed above during system noise calculations.

**Dark Count**

| 4. Dark Count (c): | 1.2 |
|---|---|

Dark count is a function of the CCD characteristics and the temperature of the CCD. The dark count will double with a rise of 5-6 degrees C. A simple way to determine dark count is to take a 60-second dark frame (a 60-second exposure with the shutter closed) at a temperature of -5° C. Determine the mean value of the pixels within a region of interest near the center of the frame. Next, take a bias frame and again determine the mean value. The dark count then becomes: (Dark - Bias)/60*system gain in electrons/second. A word of caution: Shutters can leak light. The camera should be well sealed and in a very dark room when this is done.

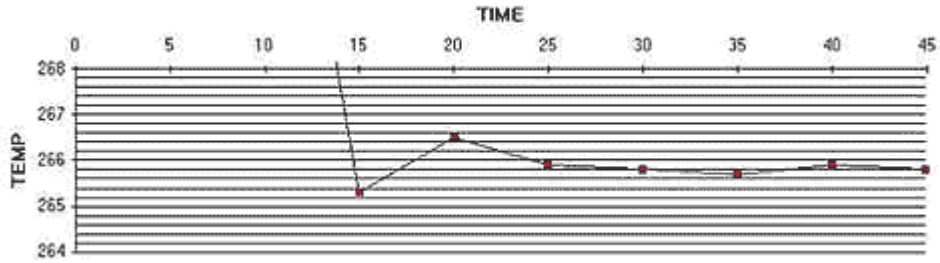
**Temperature Stability**

| 5. Temperature Stability (d) | | |
|---|---|---|
| | Max Delta: | -34 |
| | Zero/Scale: | 95/2.1 |

Temperature stability data given in the data sheets starts with a measure of the maximum temperature delta that can be achieved from an ambient temperature of +25 °C. This maximum delta will often be greater than the difference between your ambient temperature and the operating temperature.

The zero/scale numbers are those used by the software in interpreting the data coming from the temperature control subsystem. They are listed as a reference only. The Apogee Instruments temperature control system is independent of the computer and software once the system is enabled and desired temperature given. The computer can be reset, other programs can be run, and the camera-control software can be exited and re-entered without influencing camera temperature.

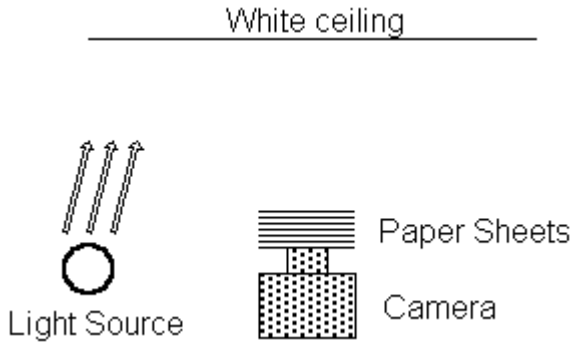
Another feature of this temperature control system is the automatic ramp times to cold temperature and back to ambient. Once any desired temperature is programmed, the descent and ascent rate is controlled by the electronics. This limits the rate of change to the CCD, thus preventing premature failure due to excessive temperature shock. On the chart below, 15-20 minutes passes before the temperature ramps to the desired value of about -7 degrees C. The camera-control software reports current temperature by reading a status port on the temperature controller, but there is some noise in the reading of this temperature. For user information on the current state of the controller, this noise does not present a problem. For testing of real temperature stability, we directly monitor the temperature sensor telemetry. Unless you have electronics expertise and a precision voltmeter, we do not recommend you do this test yourself. If you do, there is a monitor point on the C contoller board.




**Signal Variance**

## 6. Signal Variance (Gain)

The signal variance method of determining system gain in electrons per ADU is the most difficult of the tests discussed here, but can be repeated by anyone who follows the procedure outlined. This method is one where multiple exposures are taken with increasing light. Standard deviation and mean count data is collected for each image. The standard deviation numbers are each squared, then plotted with the net mean (mean - bias) numbers. The slope of the line represents the gain of the system. The test setup is very much like that discussed for the linearity test above. There are error sources in this simplified measurement and better methods exist for determining gain. This description is used for simplicity to better describe the concept.

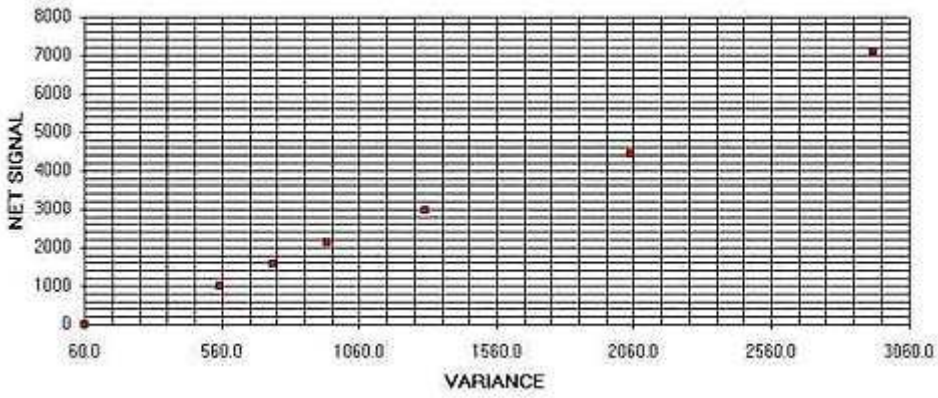



Try the following procedure:

1. Set up the conditions as you did for the linearity test. The light will probably have to be brighter.
2. Stack several sheets (8-10) of plain white paper over the camera.
3. Take a bias frame. Record the mean and standard deviation from the cursor box positioned in the middle of the frame.
4. Remove a sheet of paper. Take a 0.1 second exposure.
5. Record the mean and standard deviation from the cursor box positioned in the middle of the frame.
6. Repeat steps 4-5 until the paper is gone or the image saturates.
7. Create 2 more columns next to the data you've recorded. In one column record the square of the standard deviation data you recorded earlier. In the other column, subtract the bias mean from each mean you recorded. Your data should now look something like:

| **SD** | **MN** | SD2 | MN-BIAS |
|---|---|---|---|
| 7.74 | 1769 | 59.9 | 0 |
| 23.51 | 2777 | 552.7 | 1008 |
| 27.30 | 3357 | 745.3 | 1588 |
| 30.69 | 3886 | 941.9 | 2117 |
| 36.05 | 4728 | 1299.6 | 2959 |
| 45.23 | 6222 | 2045.8 | 4453 |
| 54.13 | 8852 | 2930.1 | 7083 |
| 83.16 | 15228 | 6915.6 | 13459 |
| 122.60 | 29468 | 15030.8 | 27699 |

All that remains is to plot the net signal on the Y axis and the SD2 data on the X axis. Draw a straight line through the data to make the best possible fit. To determine the slope, pick 2 points along the line. The slope will be (Ypoint 1 - Ypoint 2)/(Xpoint 1 - Xpoint 2). For example in this case, the two points might be net signal numbers of 6000 and 0, and variance numbers of 2560 and 60. So (6000-0)/(2560-60) = 2.4 electrons per ADU (Analog to Digital Unit) or count.


8000
7000
6000
5000
4000
3000
2000
1000
0
NET SIGNAL
60.0
560.0
1060.0
1560.0
2060.0
2560.0
3060.0
VARIANCE

## *APPENDIX C.*

## *C.1 Quantum Efficiency*

Quantum efficiency gives an indication of how efficiently incident photons are detected. It is the ratio of the number of detected electrons to the product of the incident photons multiplied by the number of electrons each photon can be expected to generate, for example light photons generate one electron-hole pair. In silicon an energy of 3.65 eV, which is the binding energy of an electron, is required to produce one electron hole. The energy, *E*, of the incident photons is given by

$$E = \frac{1.24}{\lambda} \qquad \text{[eV]}. \qquad \text{C1.1}$$

Here $\lambda$ is the photon wavelength in millimetres (mm).

The number of collected electrons per pixel per second, $N_{e,}$ for wavelengths greater than 300 μm is given by

$$N_e = 5.03 \times 10^{10} \times P \times A \times \lambda \times QE \ , \qquad \text{C1.2}$$

where $P$ is the optical power density [$\mu Wcm^{-2}$], $A$ is the pixel area [$cm^2$], $\lambda$ is the wavelength [μm] and $QE$ is the quantum efficiency in percent, (SITe, 2003).

The quantum efficiency is generally a function of the wavelength and temperature, and is given by

$$QE = \frac{Q_n h c}{q T_{\text{int}} \Phi_0 \lambda} \ , \qquad \text{C1.3}$$

where $Q_n$ is the number of minority carriers, $h$ is Planck's constant, $c$ is the speed of light, $q$ is unit charge, $T_{\text{int}}$ is integration time, $\Phi_0$ is the incoming photon flux, and $\lambda$ is the wavelength of the light. Associated with the quantum efficiency is the spectral

response, R, which is defined as the ratio of the output current, $I_{out}$, of the sensor to the incoming photon flux, $\Phi_0$. The spectral response provides a measure of the output response of the CCD image sensor due to an optical input signal. The output current is given by

$$I_{out} = \frac{Q_n}{T_{\text{int}}}. \qquad \text{C1.4}$$

The response is expressed as

$$R = \frac{Q_n}{T_{\text{int}}\Phi_0}. \qquad \text{C1.5}$$

Substituting equation C1.5 into equation C1.3, gives quantum efficiency as a function of spectral response

$$QE = \frac{Rhc}{q\lambda} \quad , \qquad \text{C1.6}$$

QE is specified at different frequencies, and typically the QE in the visible region peaks at about 650 nm (Li and Nathan, 2005).

Related to quantum efficiency is the detective quantum efficiency, which is an absolute measure of the efficiency of the real detector compared to that of the ideal detector. It is defined as (Munro *et al*., 1990),

$$DQE = (SNR_{OUT}/SNR_{IN})^2 , \qquad \text{C1.7}$$

where $SNR_{OUT}$ indicates output signal to noise ratio of the radiation detector and $SNR_{IN}$ the signal to noise ratio associated with the radiation beam. The detective quantum efficiency can be employed as an overall measure of image quality. When considering the two types of detectors, the integrating and quantum detector, the DQE for an integrating system, $DQE_{\text{int}}$, is given by

$$DQE_{\text{int}} = \frac{QE}{1 + \frac{\sigma_m^2}{(QE)(N_{in})}}, \qquad \text{C1.8}$$

where $N_{in}$ is the number of incident photons and $\sigma_m^2$ represents the standard deviation of measurements. For a quantum detector, where the charges are not integrated and individual pulses are counted the DQE is given by

$$DQE_{quant} = QE\left[1 - \frac{(QE)(\tau)(N_{in})}{\Delta t}\right]^2 \exp\left(-\frac{(QE)(\tau)(N_{in})}{\Delta t}\right), \qquad \text{C1.9}$$

where $\tau$ is detector's dead time, and $\Delta t$ is the measurement time. From equations C1.8 and C1.9 the maximum DQE possible for the detector is given by QE; the quantum efficiency sets the physical limit of any detector (Ahmed, 2007). It can be seen that the DQE of an integrating detector increases with incident photon intensity while it's the opposite for the quantum detector, this is show in Figure C-1.

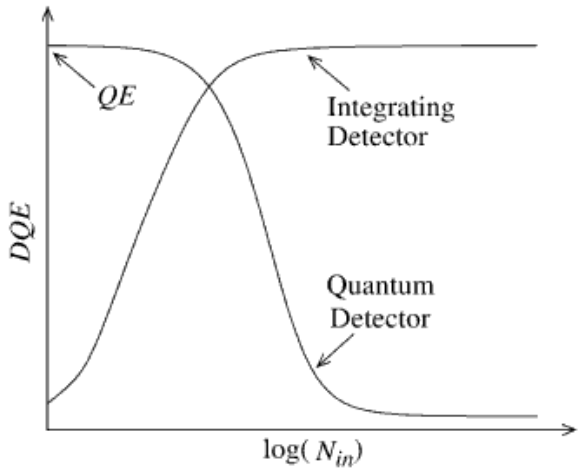



**Figure C-1 The variation of detective quantum efficiencies with respect to incident number of photons for integrating and quantum detectors**. *[Image from Ahmed, , (2007)]*

The DQE is a measurement of the real performance of an imaging system considering all the stages involved in producing the final image. In an ideal imaging system 100%

of the x-ray quanta that reach the detector would be used to create the image, but this is not the case in a real imaging system. In a real system the signal obtained will not be entirely made up of just the signal generated by the quanta, but to some varying degree will also be made up of noise. Other factors such as the amount of contrast in the image are also considered when calculating the DQE, as a high contrast image will be less affected by noise (Oakley J., 2003). For a system with ideal noise properties, the quantum efficiency, QE*(f)*, will be equal to the DQE*(f)* (at $f=0$), where $f$ is spatial frequency (Bushberg J.T.*et al*, 2002 and Guerra A.D., 2004). Ideal (white) noise is an idealized noise process having a power spectral density that is constant over all frequencies. The term white is used to describe such noise based on the fact that the spectrum of white light is constant over all frequencies in the visible range (Whitaker J. C., 1996 and Taylor N. T., 1993)

## *C.2 Depth of Field*

A great depth of field would make the system less susceptible to defocusing. Depth of field is strongly dependent on the working distance. It is also dependent on the lens focal length, aperture size and focus distance. When an object is at the exact distance at which the lens is focused, all the points on the object would form points on the image plane. As the object moves out of focus, these points grow and become circles. These circles are referred to as circles of confusion, which become larger the further out of focus the object is. However, there is a point at which the eye is unable to resolve these circles. When determining the size at which the circle of confusion becomes visible, the rule of thumb was to take it to be $1/1730^{th}$ the size of the diagonal of the image (Collins, 2005). The depth of focus was determined by calculating the near and far focus limit. The near focus limit, $F_N$, is given by

$$F_N = \frac{H \times D}{H + (D - L)} \quad . \qquad \text{C2.1}$$

The far focus limit, $F_F$, is given by

$$F_F = \frac{H \times D}{H - (D - L)} \quad , \qquad \text{C2.2}$$

where $H$ is the hyperfocal distance, $D$ is the distance at which the lens is focused, and $L$ is the lens focal length. Equation C2.1 and C2.2 are derived by considering a symmetrical lens as illustrated in Figure C-2, with the subject at distance $D$ in focus at image distance $I$. Point objects at distances $F_F$ and $F_N$ would be in focus at image distances $I_F$ and $I_N$, respectively; at image distance I, they are imaged as blur spots.

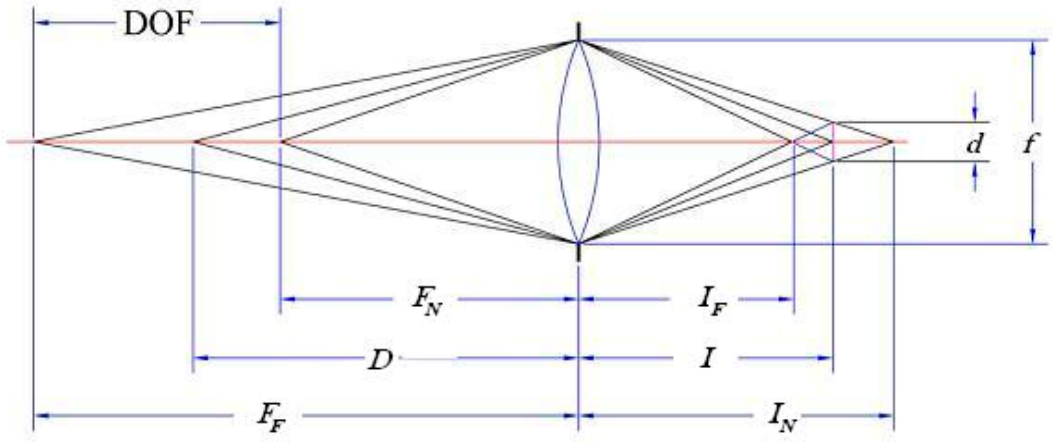



**Figure C-2. The depth of field for symmetrical lens**

The depth of field is affected by the aperture stop diameter $f$; when the blur spot diameter is equal to the acceptable circle of confusion $d$, the near and far limits of DOF are at $F_N$ and $F_F$. From similar triangles,

$$\frac{I_N - I}{I_N} = \frac{d}{f} \quad , \qquad \text{C2.3}$$

$$\frac{I - I_F}{I_F} = \frac{d}{f} \quad . \qquad \text{C2.4}$$

The f-number $F_\#$ is related to the lens focal length $L$ and the aperture diameter $f$ by

$$F_{\#} = \frac{L}{f} \ . \qquad \text{C2.5}$$

Substituting into the previous equations gives

$$I_N = \frac{L \times I}{L - (F_{\#} \times d)} \ , \qquad \text{C2.6}$$

$$I_F = \frac{L \times I}{L + (F_{\#} \times d)} \ . \qquad \text{C2.7}$$

The image distance $I$ is related to an object distance $O$ by the thin-lens equation

$$\frac{1}{O} + \frac{1}{I} = \frac{1}{L} \ . \qquad \text{C2.8}$$

Substituting into the two previous equations gives the near and far limits of DOF:

$$F_N = \frac{D \times L^2}{L^2 + (F_{\#} \times d)(D - L)} , \qquad \text{C2.9}$$

$$F_F = \frac{D \times L^2}{L^2 - (F_{\#} \times d)(D - L)} \ . \qquad \text{C2.10}$$

Setting the far limit of DOF $F_F$ to infinity and solving for the focus distance $D$ gives

$$D = H = \frac{L^2}{F_{\#} \times d} + L \, , \qquad \text{C2.11}$$

where $H$ is the hyperfocal distance. Setting the subject distance to the hyperfocal distance and solving for the near limit of DOF gives

$$F_N = \frac{L^2 / (F_{\#} \times d) + L}{2} = \frac{H}{2} \ . \qquad \text{C2.12}$$

For any practical value of H, the focal length is negligible in comparison, so that

$$H \approx \frac{L^2}{F_{\#} \times d} \ . \qquad \text{C2.13}$$

Substituting the approximate expression for hyperfocal distance into the formulae for the near and far limits of DOF gives

$$F_N = \frac{H \times D}{H + (D - L)} \ , \qquad \text{C2.14}$$

$$F_F = \frac{H \times D}{H - (D - L)} \ . \qquad \text{C2.15}$$

The hyperfocal distance allows for the greatest DOF to be obtained. If the lens is set to focus at the hyperfocal distance this gives the maximum depth of field from half the hyperfocal distance to infinity.

## C.3 Field of View

The field of view is the viewable area of the object that fills the camera's sensor, which for this work is the CCD chip. The size of the sensor's active area, together with the working distance between the scintillation screen and the camera's lens, and the optical properties of the lens (in particular the focal length), are important factors in determining the field of view. Generally, under similar conditions, larger sensors give larger field of views. On the other hand, if the lens is not able to support a large CCD chip size a "tunnel effect" results, caused by vignetting with the edges of the field being darker. Another aspect of the optical system is the depth of field, which gave an insight into the focusing ability of the system.

## C.4 Lens Coupling Efficiency

Work done by Yu and Boone (1997) and Liu *et al.* (1994) on lens coupling efficiency will now be considered. The benefit of systems having a scintillating screen coupled to a detector through a lens is that a relatively small photo-detector can form an image

from a large region of the scintillator by demagnification. However, with demagnification there is a potential for large light losses, which may cause a secondary quantum sink and leads to a reduction in quantum efficiency. A demagnifying optical coupling results in the loss of spatial resolution, which is inversely proportional to the demagnification between the image plane and the CCD focal plane (Karellas *et al.*, 1992).

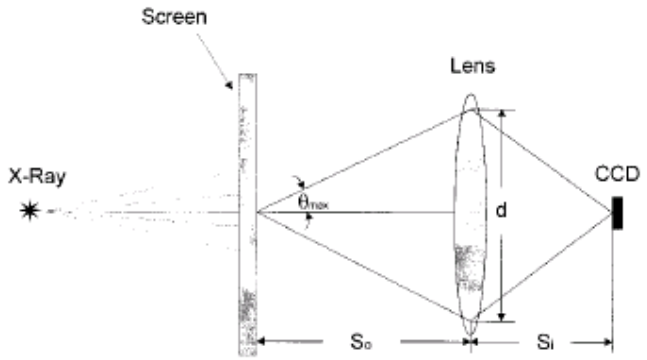



**Figure C-3 A schematic diagram of a lens coupled imaging system.**

The lens coupling efficiency for a generalised case, as shown in Figure C-3, without taking into account the emission characteristics of the scintillating screen, in terms of spherical coordinates is given by

$$g_2 = T\frac{\int_{\varphi=0}^{2\pi}\int_{\theta=o}^{\theta_{\max}} f(\theta)\sin\theta\cos\theta\, d\theta\, d\varphi}{\int_{\varphi=0}^{2\pi}\int_{\theta=o}^{\pi/2} f(\theta)\sin\theta\cos\theta\, d\theta\, d\varphi} = T\frac{\int_{\theta=o}^{\theta_{\max}} f(\theta)\sin\theta\cos\theta\, d\theta}{\int_{\theta=o}^{\pi/2} f(\theta)\sin\theta\cos\theta\, d\theta} \quad \text{C4.1}$$

Here $g_2$ is the lens coupling efficiency. $T$ is the bulk transmittance of the lens, which is the ratio of the photon energy passing into the image domain to the photon energy

falling into the lens aperture at the object domain. $\theta$ is the polar angle and $f(\theta)$ is the normalized angular distribution for the radiance of the scintillation screen. The angle at which the angular distribution of the radiance was normalised to, was taken to be at 0°. To obtain the normalized angular distribution, the angular distribution of the radiance was divided by the radiance at a particular angle; in this case at the 0° angle as shown in Figure C-4. Since $f(\theta)$ is typically measured for a given screen, a simple analytic expression for this function is usually not available. Numerical methods are therefore used to evaluate the integrals in Equation C4.1 (Yu and Boone, 1997). φ is the azimuthal angle and $\theta_{max}$ is the polar angle that the marginal ray makes with the optical axis.

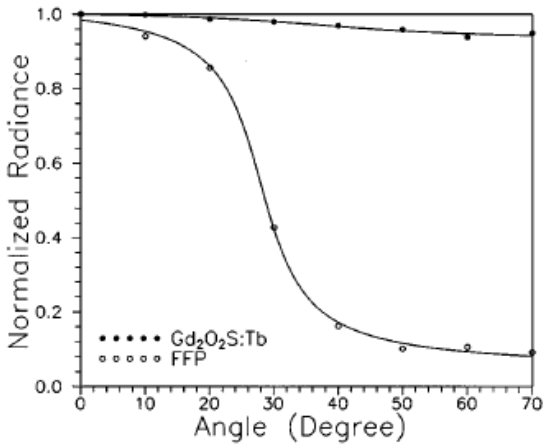



**Figure C-4 The normalized radiance as a function of angle is shown for two different scintillating screens $Gd_2O_2S$:Tb and FFP (fiber optical scintillating faceplate)** *The angular distribution is normalized to the radiance at the angle of 0°. [Image from Yu and Boone (1997)]*

Assuming a Lambertian source for the scintillation screen, $f(\theta) \equiv 1$, equation C4.1 reduces to

$$g_2 = T\frac{\int_{\varphi=0}^{2\pi}\int_{\theta=o}^{\theta_{\max}}\sin\theta\cos\theta\,d\theta\,d\varphi}{\int_{\varphi=0}^{2\pi}\int_{\theta=o}^{\pi/2}f(\theta)\sin\theta\cos\theta\,d\theta\,d\varphi} = T\sin^2(\theta_{\max})\ . \quad \text{C4.2}$$

From the geometry illustrated in Figure C-3, it follows that

$$\sin^2(\theta_{\max}) = \frac{(d/2)^2}{(d/2)^2 + S_o^2}, \qquad \text{C4.3}$$

where d is the diameter of the lens, and $S_o$ is the distance between the screen and the lens. From the lens equation,

$$\frac{1}{S_o} + \frac{1}{S_i} = \frac{1}{f} \quad , \qquad \text{C4.4}$$

where $S_i$ is the distance between the lens and the CCD, and $f$ is the focal length of the lens in Figure C-3. Taking $m$ as the system geometrical magnification factor, $m = S_i / S_o$; and $F_\#$ as the f-number of the lens, $F_\# = f/d$. Substituting $m$ and $F_\#$ into equation C4.1, C4.2 and C4.4 gives

$$g_2 = \frac{Tm^2}{4(F_\#)^2(1+m)^2 + m^2} \ . \qquad \text{C4.5}$$

Assuming a point source as shown in Figure C-5 the lens coupling efficiency is given by

$$g_2 = T\frac{\int_{\varphi=0}^{2\pi}\int_{\theta=o}^{\alpha_{\max}} \sin\theta d\theta\, d\varphi}{\int_{\varphi=0}^{2\pi}\int_{\theta=o}^{\pi/2} \sin\theta\, d\theta\, d\varphi} = \frac{T}{2}(1-\cos\alpha_{\max}) = T\sin^2\left(\frac{\alpha_{\max}}{2}\right), \qquad \text{C4.6}$$

where $\alpha_{\max}$ is the meridian angle in the screen that the marginal ray makes with the optical axis.

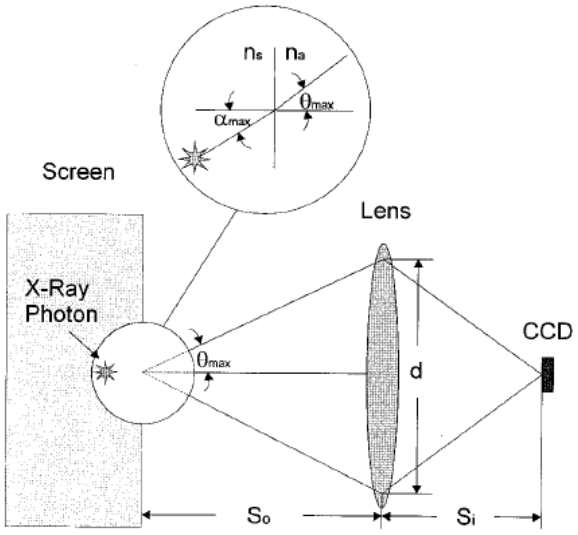



**Figure C-5 An illustration of assumption of point source.** *Light photons propagate across the boundary between the phosphor screen and the air, and Snell's. law was applied to get the relationship between the angle $\alpha$ in the screen and the angle $\theta$ in the air.*

When the angle $\alpha_{max}$ is small, then

$$g_2 = T\sin^2\left(\frac{\alpha_{\max}}{2}\right) \approx T\left(\frac{1}{2}\sin(\alpha_{\max})\right)^2 . \qquad \text{C4.7}$$

From Snell's law $n_s \sin(\alpha_{max}) = n_a \sin(\theta_{max})$, where $n_s$ is the refractive index of the screen, $n_a$ is the refractive index of the air, $n_a \approx 1$. Equation C4.7 becomes

$$\begin{aligned} g_2 = T\left(\frac{1}{2n_s}\sin(\theta_{\max})\right)^2 &\approx T\left(\frac{1}{2n_s}\tan(\theta_{\max})\right)^2 \\ &= T\left(\frac{d/2}{2n_s S_o}\right)^2 \end{aligned} . \qquad \text{C4.8}$$

Here the tangent is substituted for the sine, which is valid for small angles. By substituting the parameters $m$ and $F_{\#}$ into equation C4.4 and equation C4.8, the equation becomes

$$g_2 = \frac{Tm^2}{16(F_{\#})^2(1+m)^2 n_s^2} . \qquad \text{C4.9}$$

The assumptions for $g_2$ are that the marginal ray angle is small ($\theta_{max} \leq 10°$), and there is negligible light attenuation within the screen (Yu and Boone, 1997 and Liu *et al.*, 1994).

Liu *et al.* (1994) suggest that for a well-designed multi-piece photographic lens, a good estimate for $T$ is $T$ = 70 %- 80 %, Yu and Boone have taken it to be unity. The demagnification factor is given by $m$, it is the ratio of the object to the image size. The f-number of the lens is given by $F_{\#}$, it is the quotient of focal length of the lens, $f$, divided by effective diameter of the lens, $d$ and $n_s$ is the refractive index of the screen.

If the lens coupling efficiency is known, the signal to noise ratio can be determined by the approximation (Liu *et al.*, 1994)

$$SNR = \sqrt{\eta N_i} \Bigg/ \sqrt{\left(1 + \frac{1}{g_1 g_2 g_3}\right)} \,, \qquad \text{C4.10}$$

where $\eta$ is the quantum efficiency of the scintillating screen. $\eta$ is a quantity defined as the fraction of photons hitting the surface of the scintillating screen, that will produce an electron–hole pair. $N_i$ is the x-ray photon flux (number of x-ray photons per pixel at the entrance of the scintillating screen), $g_3$ is the quantum efficiency of the CCD (electrons/photon), $g_2$ is the optical coupling efficiency of the lens, and $g_1$ is x-ray light conversion factor of the screen. The product $g_1 g_2 g_3$ is the total quantum gain of the imaging system, whose units are those of electrons produced in the CCD per x-ray photon absorbed in the scintillating screen.

For large values of $g_1 g_2 g_3$ the equation becomes (Liu *et al.*, 1994)

$$SNR = \sqrt{\eta N_i} \,, \qquad \text{C4.11}$$

this represents a perfect x-ray quantum-noise-limited system. For values of $g_1 g_2 g_3$ smaller than about 10, the SNR of the system is dominated by the low efficiency of the lens. Equation C4.9 is a monoenergetic approximation of the SNR equation, which assumes the lens-coupled CCD imaging chain obeys Poisson statistics. The equation is used to determine whether an imaging system is x-ray quantum noise limited or not. Quantum noise may also occur in electronic circuits. It is noise that arises when the finite number of particles that carry energy, such as electrons in an electronic circuit or photons in an optical device, is small enough to give rise to detectable statistical fluctuations in a measurement. It represents the fundamental limit of the achievable signal-to-noise ratio of an optical system. A quantum noise limited system is a system wherein the minimum detectable signal is limited by the quantum noise.

## *C.5 Lens Distortion*

Distortion arises from the fact that transverse magnification may be a function of the off-axis image distance. This causes the different areas of the lens to have different focal lengths and different magnifications as shown in Figure C-6, where the object plane is at $O$, $Q$ is the general off-axis point, $E'$ is a point in image space where the central ray of the beam crosses the optical axis, $E$ is a point in object space where the central ray of the beam crosses the optical axis, $\overline{\mathrm{Q}}$ is the real image point, $Q'$ is the Gaussian image point, $O'$ is the axis image point, $\overline{\eta}'$ is the real image height, and $\eta'$ is the Gaussian image height.

When distortion is present, the point *Q* is imaged on the Gaussian image plane but not on the expected Gaussian position. In paraxial optics (Gaussian optics), the Gaussian image plane is the plane conjugate to the object plane in the absence of aberrations; it can be computed from Newton's lens equation if the object position is known. Gaussian optics is also known as first-order optics, and arises from the basic approximations $\sin \varphi \cong \varphi$, $\tan \varphi \cong \varphi$, and $\cos \varphi \cong 1$, which leads to Snell's law. These approximations greatly simplify ray tracing and lens formulas, but they do restrict the angles the light rays make with the optical axis to rather small values of 20° or less.

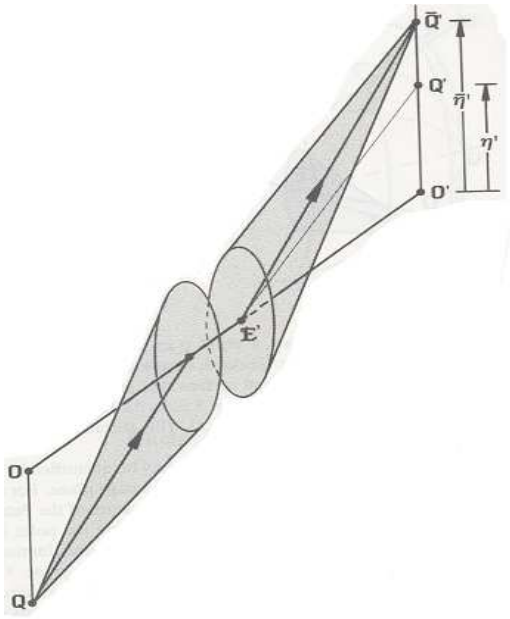



**Figure C-6 An illustration of the distortion aberration** *[Image from Smith and Atchison, 1997]*

Lens distortion does not degrade the quality of the image in terms of sharpness or focus, but affects the shape of the image. Both radial and tangential distortion is possible. Geometrical distortion causes a change in shape, which results in pincushion

or barrel distortions as illustrated in Figure C-7. Radial lens distortion is an alteration in magnification from the center of the field to any point in the field, measured in a radial direction from the center of the field. It is usually expressed as a polynomial function of the radial distance from the point of symmetry (usually coinciding with the principal point). There are two major types of radial distortion. The first one is a negative displacement also called barrel distortion. Barrel distortion occurs when points are moved from their correct position towards the center of the image. The second type of radial distortion is a positive displacement, which occurs when points are displaced further away from the optical axis. This type is also called pincushion distortion. Barrel distortion is common for wide-angle lenses and pincushion distortion for narrow angle lenses (Jedlička and Potůčková, 2007; Mikhail M.E. *et al,* 2001). Some radial distortion is inherent in most optical systems, but can be reduced by proper design.

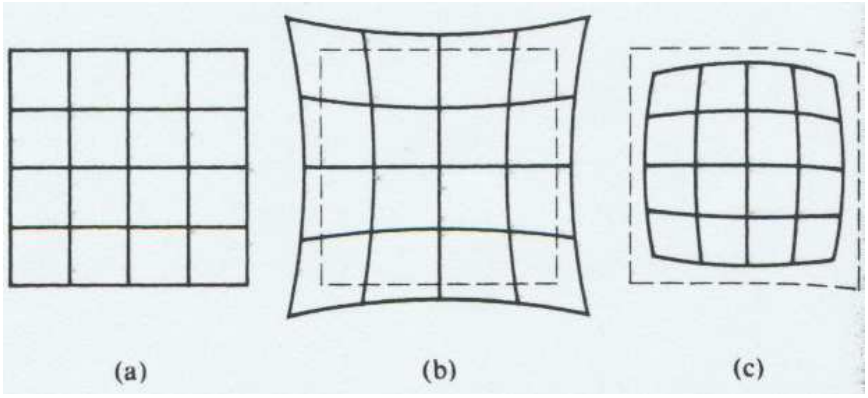



**Figure C-7 An illustrations of geometrical distortions introduced by the lens.** *(a) A checkerboard like grid without distortion; (b) Pincushion distortion; (c) Barrel distortion.*

The tangential distortion (also known as decentering distortion) is due to lack of centering (decentering) of lens elements along the optical axis, and other manufacturing defects in a compound lens. It results in the displacement of image

points perpendicular to the radius from the center of the field. One of the effects of tangential distortion is that a straight line passing through the center of the field may be recorded as a weakly curved line as shown in Figure C-8.

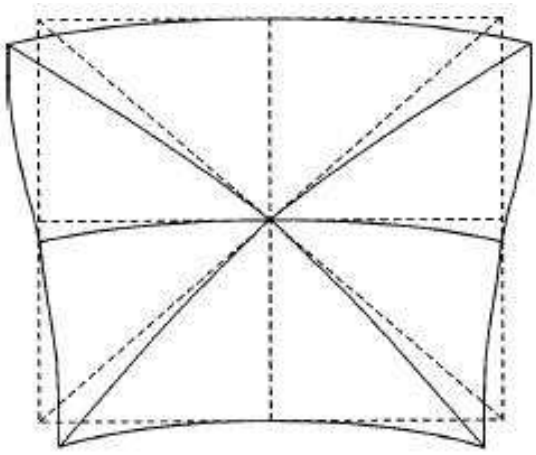
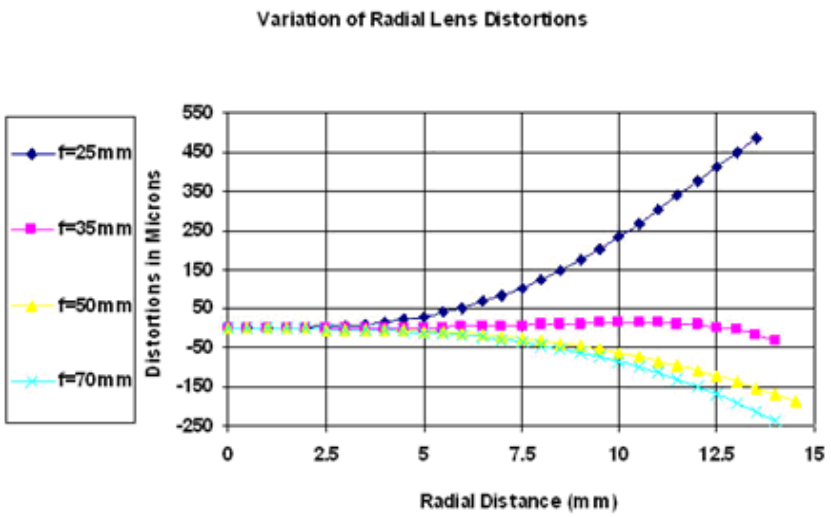
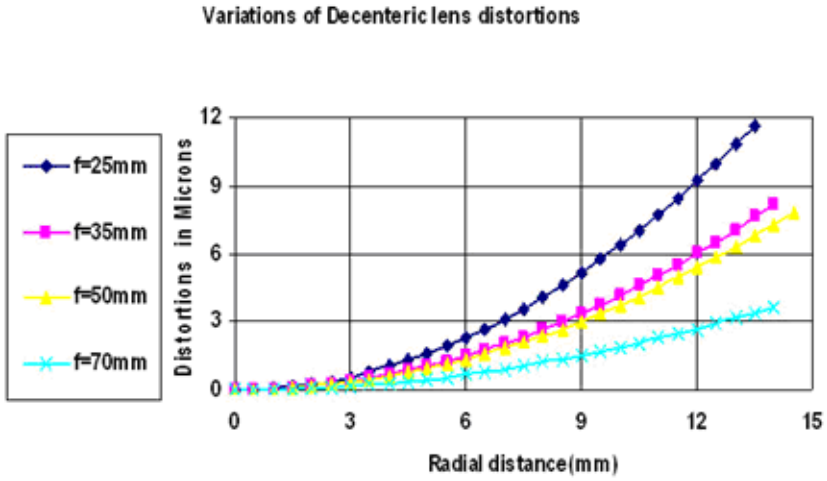


**Figure C-8 an illustration of tangential distortion***: A straight line passing through the center (optical axis) of the field is recorded as a weakly curved line. In this schematic, the dashed lines show the undistorted geometrical pattern and the solid lines represent the distorted pattern. [Image from* Liu. *et al*. (2000)*]*

Tangential distortion is usually an order of magnitude less than radial distortion and varies less with focus, much less than radial distortion, as indicated by the distortion profiles shown in Figure C-9. Camera calibration researhers have argued and experimentally verified that radial distortion is the dominant distortion effect (Zhuang and Roth, 1996)




**(a)**




**(b)**

**Figure C-9 (a)The radial distortion profile for a digital camera set at different focal length. (b) The decentering distortion profile for a digital camera set at different focal length.**

For our system, the captured images needed to be corrected for image distortions. Because of the shape of the lenses and the imperfections, which arise during the manufacturing process, the lenses exhibit lens distortion. Lens aberrations cannot be completely avoided in optical design, with commercially available relay lenses having distortion errors in the range of 1 to 3 %, (Liu *et al.*, 2000), for zoom lenses this figure is higher. Various correction methods can be applied to minimize lens distortion.

Lenses generally have curved surfaces and therefore project world points in a somewhat spherical surface instead of a plane. To correct for lens distortion a distortion model can be used that models how the distortion occurs on the image. However to conceptualise this, a camera model may be constructed to give an indication of the workings of a camera from which a method can be devised to do the necessary corrections for the distortions.

## *C.6 Projective Camera Model*

A camera can be represented by a matrix, which maps homogenous coordinates of a *3D* world point to homogeneous coordinates of the image point on a *2D* image plane (Hecht, 2001). For a point *(x, y, z)* in 3D space, the homogeneous coordinates are a 4-vector representation $\begin{pmatrix} x \\ y \\ z \\ 1 \end{pmatrix}$ of the point. CCD cameras are usually modelled using a specialized and simple camera model based on the pinhole camera. Figure C-10 illustrates the projection of points in space onto a plane at $z = f$, with this plane being called the image plane or focal plane.

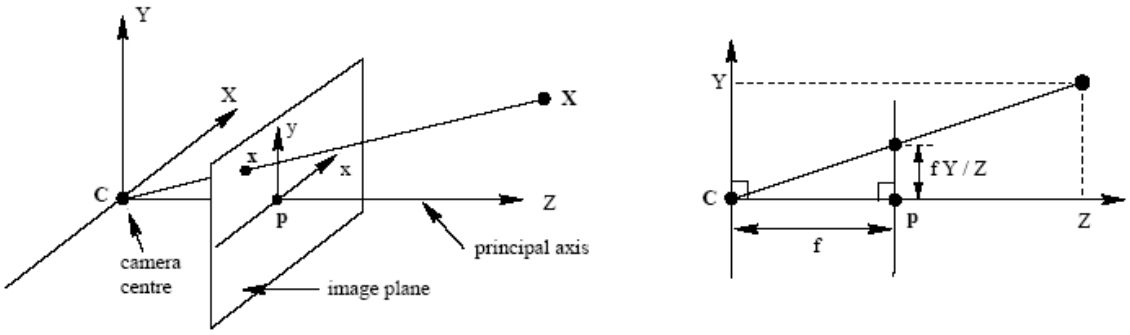



**Figure C-10 The pinhole camera geometry.** *C is the camera center and p the principal point. The camera center is placed at the coordinate origin, with the image plane placed in front of the camera center.[Image from Hartley and Zisserman, 2000]*

A point in space with coordinates $\mathbf{x} = (X, Y, Z)^{\mathsf{T}}$ is mapped to the point on the image plane where a line joining the point $\mathbf{x}$ to the center of projection meets the image plane. The column vector $\mathbf{x}$ is given by the transpose of the row vector $(X, Y, Z)$. By similar triangles, the point $(X, Y, Z)^T$ is mapped to the point $(fX/Z, fY/Z, f)^{\mathsf{T}}$ on the image plane. This gives the mapping

$$(X, Y, Z)^T \mapsto (fX / Z, fY / Z)^T \quad . \qquad \text{C6.1}$$

In terms of homogeneous vectors, the central projection is expressed in matrix form as

$$\begin{pmatrix} X \\ Y \\ Z \\ 1 \end{pmatrix} \mapsto \begin{pmatrix} fX \\ fY \\ Z \end{pmatrix} = \begin{bmatrix} f & 0 & 0 & 0 \\ 0 & f & 0 & 0 \\ 0 & 0 & 1 & 0 \end{bmatrix} \begin{pmatrix} X \\ Y \\ Z \\ 1 \end{pmatrix} . \qquad \text{C6.2}$$

This can be expressed as

$$\mathrm{x} = \mathrm{P}\mathbf{X} , \qquad \text{C6.3}$$

where $\mathbf{X}$ is the world point represented by the homogeneous 4-vector $(\mathrm{X}, \mathrm{Y}, \mathrm{Z}, 1)^{\mathsf{T}}$, $\mathbf{x}$ is a homogeneous 3-vector for the image point, and P represents the $3 \times 4$ homogeneous camera projection matrix. The more general form of equation C6.2, which takes into account whether the origin of the coordinates in the image plane is at the principal point is given by

$$\begin{pmatrix} X \\ Y \\ Z \\ 1 \end{pmatrix} \mapsto \begin{pmatrix} fX + Zp_x \\ fY + Zp_y \\ Z \end{pmatrix} = \begin{bmatrix} f & 0 & p_x & 0 \\ 0 & f & p_y & 0 \\ 0 & 0 & 1 & 0 \end{bmatrix} \begin{pmatrix} X \\ Y \\ Z \\ 1 \end{pmatrix} , \qquad \text{C6.4}$$

where $(p_x, p_x)^{\mathsf{T}}$ are the coordinates of the principal point. The concise form of equation C6.4 is given as

$$\mathbf{x} = K\left[\mathrm{I}\middle|0\right]\mathbf{x}_{\mathbf{cam}}, \qquad \text{C6.5}$$

where $\left[\mathrm{I}\middle|0\right]$ represents an augmented matrix divided up into a 3 × 3 block, which is the identity matrix together with a column vector (which in this case is a zero vector). The augmented matrix of a matrix is obtained by combining two matrices. Given the matrices *A* and *B*:

$$A = \begin{bmatrix} a_{11} & a_{12} & a_{13} \\ a_{21} & a_{22} & a_{23} \\ a_{31} & a_{32} & a_{33} \end{bmatrix}, \quad B = \begin{bmatrix} b_1 \\ b_2 \\ b_3 \end{bmatrix} \qquad \text{C6.6}$$

then, the augmented matrix [A|B] is written as:

$$\left[A \mid B\right] = \left[\begin{array}{ccc:c} a_{11} & a_{12} & a_{13} & b_1 \\ a_{21} & a_{22} & a_{23} & b_2 \\ a_{31} & a_{32} & a_{33} & b_3 \end{array}\right]. \qquad \text{C6.7}$$

The $\mathbf{x}_{\mathrm{cam}}$ in equation C6.7 emphasizes that the camera is assumed to be located at the origin of a Euclidean coordinate system, and *K* is known as the camera calibration matrix, which is given by

$$K = \begin{bmatrix} f & 0 & p_x \\ 0 & f & p_y \\ 0 & 0 & 1 \end{bmatrix}. \qquad \text{C6.8}$$

The world coordinate frame and the camera coordinate frame are related through a rotation and a translation. A point in the camera coordinate frame can be written as

$$\mathbf{x}_{\mathrm{cam}} = \begin{bmatrix} R & -R\tilde{C} \\ 0 & 1 \end{bmatrix} \begin{pmatrix} X \\ Y \\ Z \\ 1 \end{pmatrix} = \begin{bmatrix} R & -R\tilde{C} \\ 0 & 1 \end{bmatrix} \mathbf{X}, \qquad \text{C6.9}$$

where $\widetilde{C}$ represents the coordinates of the camera center in the world coordinate frame, and $R$ is a $3 \times 3$ rotation matrix representing the orientation of the camera coordinate frame. The equation C6.9 can then be written as

$$\mathbf{x} = KR[\mathrm{I} \mid -\widetilde{C}]\,\mathbf{X}\,, \qquad \text{C6.10}$$

where $\mathbf{X}$ is now in the world coordinate frame. It can be seen that the general pinhole camera, $P = KR[\mathrm{I} \mid -\widetilde{C}]$, has 9 degrees of freedom: 3 for $K$ (the elements $f$, $p_x$, $p_x$, which are called the internal camera parameters), 3 for $R$, and 3 for $\widetilde{C}$. The entities $R$ and $\widetilde{C}$ represent the external camera parameters. External (extrinsic) parameters define location and orientation of camera reference frame with respect to world frame, while internal (intrinsic) parameters define pixel coordinates of image points with respect to coordinates in camera reference frame.

The pinhole camera is for the ideal situation where there is no distortion. However, this is not the case with real cameras as they always have some degree of distortion. A distortion model was used as a basis for the correction of lens distortion.

## *C.7 Distortion Model*

As mentioned above, the pinhole projection camera model is for ideal situations where there is no lens distortion. Under ideal (undistorted) pinhole projection the image coordinates can be denoted by $(\widetilde{x}, \widetilde{y})$, measured in units of focal length. For a point $\mathbf{x}$ we get

$$(\widetilde{x}, \widetilde{y}, 1)^{\mathsf{T}} = \left[\mathrm{I}|0\right] \mathbf{x}_{\mathrm{cam}}\,, \qquad \text{C7.1}$$

where $\mathbf{x}_{cam}$ is the 3D point in camera coordinates given in C6.9. The undistorted point is linked to the projected point by a radial displacement.

The radial distortion can then be represented by

$$\begin{pmatrix} x_d \\ y_d \end{pmatrix} = L(\tilde{r}) \begin{pmatrix} \tilde{x} \\ \tilde{y} \end{pmatrix}, \qquad \text{C7.2}$$

where $(\tilde{x}, \tilde{y})$ is the ideal image position (which obeys linear projection); $(x_d, y_d)$ is the actual image position after radial distortion; $\tilde{r}$ is the radial distance $\sqrt{\tilde{x}^2 + \tilde{y}^2}$ from the center for radial distortion; $L(\tilde{r})$ is a distortion factor, which is a function of the radius $\tilde{r}$ only.

To correct for the radial distortion, the following can be used to give the corrected pixel coordinates

$$\hat{x} = x_c + L(r)(x - x_c) \qquad \hat{y} = y_c + L(r)(y - y_c), \qquad \text{C7.3}$$

where $(x, y)$ are the measured coordinates, $(\hat{x}, \hat{y})$ are the corrected coordinates, and $(x_c, y_c)$ is the center of the radial distortion, and $r^2 = (x - x_c)^2 + (y - y_c)^2$. The coordinates $(\hat{x}, \hat{y})$ are then related to the coordinates of the *3D* world point by a linear projective camera by using this correction.

The function $L(r)$ is defined by positive values of $r$ with $L(0) = 1$. This function can be approximated by the Taylor expansion $L(r) = 1 + \kappa_1 r + \kappa_2 r^2 + \kappa_3 r^3 + \ldots\ldots$, whose coefficients $\{\kappa_1, \kappa_2, \kappa_3, \ldots\ldots, x_c, y_c\}$ are taken to be part of the interior calibration of the camera. Using an iterative algorithm such as Levenberg-Marquardt

(Hartley and Zisserman, 2000; Triggs *et al.*, 2000), the function maybe computed by minimizing a cost based on the deviation from a linear mapping.

In the distortion model used by Bouguet, both radial and tangential distortions are considered. The model is based on the 'plumb-line' model (also known as the Brown-Conrady model) which was proposed by Brown (1966). This technique for determining radial and decentering distortions for a particular focus setting of a lens is based on the principle that in a perspective projection a straight line in object space should project as a straight line into the image space. Any deviations from linearity can be attributed to radial and decentering distortions in the lens. In his early experiments, Brown suspended thin plumblines from the ceiling in a laboratory, thereby providing the title to this method. However, the lines do not have to be vertical, merely straight. In model the expression C7.2 becomes

$$\begin{pmatrix} x_d \\ y_d \end{pmatrix} = (1 + k_c(1) r^2 + k_c(2) r^4 + k_c(5) r^6)\mathbf{x} + d_x \ , \qquad \text{C7.4}$$

where $k_c$ is a 5 × 1 vector , which has the radial and tangential distortions, $\mathbf{x}$ is a point in space, and where $d_x$ is the tangential distortion vector:

$$d_x = \begin{bmatrix} 2k_c(3)xy + k_c(4)\left(r^2 + 2x^2\right) \\ k_c(3)\left(r^2 + 2y^2\right) + 2k_c(4)xy \end{bmatrix} . \qquad \text{C7.5}$$

The final pixel coordinates $x_{pixel} = (x_p;y_p)$ of the projection of the point $\mathbf{x}$ on the image plane is:

$$\begin{aligned} x_P &= f_1 x_d + \alpha_c y_d + c_x \\ y_P &= f_2 y_d + c_y \end{aligned} . \qquad \text{C7.6}$$

Here $f$, which is a $2 \times 1$ vector of the focal length in pixels, is given by $f = \begin{pmatrix} f_1 \\ f_2 \end{pmatrix}$, $\alpha_c$ is the skew coefficient defining the angle between the length, x, and width, y, of the pixel axes (it is usually assumed that the pixels are rectangular, and thus skew is assumed to be zero), $c$ is the principle point $(c_x, c_y)$.

Therefore, the 5-vector $k_c$ contains both radial and tangential distortion coefficients. It can be seen from equation C7.4 that the coefficient of $6^{th}$ order radial distortion term is the fifth entry of the vector $k_c$.